2015

Dielectric properties and degradation monitoring in polymer-matrix structural composites

Connor Daily
Iowa State University

Dielectric properties and degradation monitoring in polymer-matrix structural composites

by

Connor Daily

A dissertation submitted to the graduate faculty

in partial fulfillment of the requirements for the degree of

DOCTOR OF PHILOSOPHY

Major: Materials Science and Engineering

Program of Study Committee:

Nicola Bowler, Major Professor

Scott Beckman

Vinay Dayal

Ronald Roberts

Xiaoli Tan

Iowa State University

Ames, Iowa

2015

TABLE OF CONTENTS

LIST OF TABLES v

LIST OF FIGURES vi

ACKNOWLEDGEMENTS xii

ABSTRACT xiii

CHAPTER 1. INTRODUCTION 1

1.1 Research Question 1

1.2 Composites in Aerospace 1

1.3 Composite Materials 2

1.4 Non-Destructive Evaluation of Composites 6

1.5 Multiphase Modeling 8

1.6 Characterization Techniques 9

1.6.1 Dielectric Spectroscopy 9

1.6.2 Fourier Transform Infrared Photoacoustic Spectroscopy 12

1.7 Thesis Organization 14

CHAPTER 2. MODELING THE INTERPHASE OF A NANODIELECTRIC THERMOSET 17

2.1 Introduction 18

2.2 Model 21

2.2.1 Regime One: Non-Overlapping Interphase 23

2.2.2 Regime Two: Interphase Overlap Through Cell Faces 24

2.2.3 Regime Three: Interphase Overlap Through Cell Faces and Edges . . . 24

2.2.4 Regime Four: Matrix Displaced Entirely by Interphase 25

2.2.5 Three-Phase Wiener Bounds . . . 26
2.3 Experiment . . . 27
2.4 Data Analysis . . . 28
2.4.1 Experimental Analysis . . . 31
2.5 Discussion and Conclusions . . . 32
2.6 Acknowledgements . . . 35
2.7 APPENDIX: CALCULATION OF REGIME 3 . . . 35
CHAPTER 3. THERMO-OXIDATIVE DEGRADATION ASSESSMENT IN QUASI-ISOTROPIC CARBON FIBER/EPOXY COMPOSITES . . . 38
3.1 Introduction . . . 39
3.2 Experiment . . . 40
3.2.1 Materials . . . 40
3.2.2 Thermogravimetric Analysis . . . 40
3.2.3 Accelerated Isothermal Aging . . . 42
3.2.4 Interlaminar Shear Strength . . . 43
3.2.5 Photoacoustic Spectroscopy . . . 43
3.2.6 Kinetic Modeling . . . 44
3.3 Results and Discussion . . . 49
3.4 Conclusion . . . 55
3.5 Acknowledgements . . . 55
CHAPTER 4. DIELECTRIC PROPERTIES AND KINETIC STUDY ON THE DEGRADATION OF BISMALEIMIDE RESIN . . . 56
4.1 Introduction . . . 57
4.2 Experiment . . . 58
4.3 Thermogravimetric Analysis . . . 59
4.4 Kinetic Modeling . . . 59
4.5 Dielectric Spectroscopy . . . 63
4.6 Dielectric Relaxation Modeling . . . 65

4.7 Discussion and Conclusions 69
4.8 Future Work 71

CHAPTER 5. DIELECTRIC AND INFRARED INFERENCE OF THERMO-OXIDATIVE AGING OF A BISMALEIMIDE COMPOSITE MATERIAL 73

5.1 Introduction 73
5.2 Experiment 75
5.2.1 Materials 75
5.2.2 Thermogravimetric Analysis 77
5.2.3 Isothermal Aging 78
5.2.4 Dielectric Spectroscopy 80
5.2.5 Mechanical Testing 81
5.2.6 FTIR Photoacoustic Spectroscopy 82
5.3 Results and Discussion 83
5.4 Conclusion 89

CHAPTER 6. CONCLUSIONS 93

LIST OF TABLES

Table 2.1 Example Pairs of Interphase Parameters for which Experimental Data [1] Falls Within Modeled Three-Phase Wiener Bounds. 33

Table 2.2 Example Pairs of Interphase Parameters for which Literature Data [2] Falls Within Modeled Three-Phase Wiener Bounds. 33

Table 4.1 Havriliak-Negami Fit Parameters for Gamma Relaxation 70

Table 5.1 Correlation Values Between Selected Inidicators and ILSS and Mass Loss 92

LIST OF FIGURES

Figure 1.1 Percentage of composite usage in the structure of a variety of aircraft, redrawn from [3]. Black squares represent Boeing aircraft, and red triangles represent those of Airbus. 3

Figure 1.2 A representative bismaleimide unit. Image obtained from [4]. 6

Figure 1.3 Top-down view of a representative vacuum bagging layup for a square-foot laminate. This schematic is not to scale. 7

Figure 1.4 Schematic of different dielectric relaxations as a function of frequency as they occur in the dielectric constant (top) and the dielectric loss (bottom), from [5]. 11

Figure 1.5 Measured relative permittivity of unaged, BMI resin from 1 kHz to 2 MHz. 12

Figure 1.6 Imaginary permittivity of unaged, BMI resin, from 1 kHz to 2 MHz. . 13

Figure 1.7 Example IR spectra for neat BMI resin. Indicated peaks are C=O stretch ∼1720 cm^{-1}, aromatic C=C stretching ∼1500 and 1600 cm^{-1}, aromatic C-H bending ∼650-750 cm^{-1}, and aliphatic C-H stretching ∼2850-3000 cm^{-1} [6, 7]. 15

Figure 2.1 The first regime, containing a non-overlapping interphase. 21

Figure 2.2 The second regime, where the interphase is overlapping through the unit cell faces. 22

Figure 2.3 The third regime, where the interphase is overlapping through the cell faces and edges. 22

Figure 2.4 The fourth regime, where the matrix phase is entirely displaced by the interphase. 23

Figure 2.5 (top) The interphase volume fraction with respect to nanofiller loading for various interphase thicknesses surrounding a 60 nm radius, spherical nanoparticle. 26

Figure 2.6 The unperturbed matrix volume (corresponding to the interphase volume fraction in Figure 2.5) with respect to nanofiller loading for various interphase thicknesses surrounding a 60 nm radius, spherical nanoparticle. 27

Figure 2.7 SEM images of the fracture surface of composites with (a) 10 and (b) 26 vol% of Si nanoparticles. 29

Figure 2.8 Upper Wiener bound showing the variation in effective permittivity of a nanocomposite as a function of both relative interphase permittivity (ϵ_i = 1-10) and thickness (t_i = 0-70 nm) with intersecting measured permittivity plane (at ϵ = 5) at 5 vol% nanofiller. The intersection of the Wiener bound with the plane gives rise to a locus of viable values of ϵ_i and t_i for the interphase. Particle radius = 50 nm; particle permittivity = 10; matrix permittivity = 3. 31

Figure 2.9 Lines of inetersection between calculated three-phase Wiener bounds and measured permittivity values, for two volume fractions of silicon/BECy nanocomposites at 1 MHz. The area highlighted by arrows indicate possible pairs of values for interphase thickness, t_i, and permittivity, ϵ_i, that are common to both volume fractions. 34

Figure 2.10 Three-phase and two-phase upper and lower Wiener bounds (UWB and LWB) for 1 MHz permittivity data measured on a silicon/bisphenol E cyanate ester nanocomposite [8]. In the calculation the nanoparticle radius = 65 nm and relative permittivity = 12, while the interphase thickness = 30 nm and relative permittivity = 7. 36

Figure 2.11 Three-phase (thick curves) and two-phase (thin-curves) upper and lower Wiener bounds for 1 kHz permittivity data measured on a LDPE/Al2O3 system [9]. In the calculation the nanoparticle radius = 20 nm and relative permittivity = 9, while the interphase thickness = 15 nm and relative permittivity = 1.6. 36

Figure 3.1 Thermograms of untoughened epoxy/carbon fiber composites. 41

Figure 3.2 Temperature derivative of the thermogram in Figure 3.1. 42

Figure 3.3 Friedman plot of the TG data from Figure 3.1. Constant fractional mass loss (CFML) lines are represented in black for increasing (from right to left) fractional mass. Heating rates are increasing from bottom right (2 °C/min) to top left (50 °C/min). 46

Figure 3.4 Activation energy as a function of fractional mass loss based on the Friedman plot from Figure 3.3. 47

Figure 3.5 Ozawa-Flynn-Wall plot of the TG data from Figure 3.1. Constant fractional mass loss (CFML) lines are represented in black for increasing (from right to left) fractional mass. Heating rates are increasing from bottom (2 °C/min) to top (50 °C/min) 49

Figure 3.6 Activation energy as a function of fractional mass loss based on the Ozawa-Flynn-Wall plot from Figure 3.5. 50

Figure 3.7 Resin mass loss results for the untoughened epoxy/carbon fiber samples. The squares represent the average of 10 measurements and the error bars represent one standard deviation. 51

Figure 3.8 ILSS results for the untoughened epoxy/carbon fiber samples. The squares represent the average of 10 measurements (except for 275 °C, which represents one measurement), and the error bars represent one standard deviation. 52

Figure 3.9 IR spectra for untoughened epoxy/carbon fiber composites. All spectra are normalized to the maximum at 1153 cm^{-1} and minimum at 3958 cm^{-1}. Higher temperature aging shows an increase near the 1682 cm^{-1} peak, representative of the introduction of more carbonyl groups due to oxidation. 53

Figure 3.10 ILSS values from Figure 3.8 vs the relative peak intensities for the 1682 cm^{-1} peak (squares) and the 2920 cm^{-1} peak (circles) extracted from Figure 3.9. Error bars for the ILSS data (shown in Figure 3.8) have been omitted for clarity. The peak intensities for the 150 °C spectra were normalized to the value of 1. 54

Figure 4.1 Temperature profile of the curing procedure for RM-3002 BMI flash, as detailed in [10]. 58

Figure 4.2 BMI mass loss as a function of temperature for four different heating rates. 59

Figure 4.3 Temperature derivatives of the thermograms in Figure 5.3. 60

Figure 4.4 Friedman plot of the thermograms in Figure 5.3. CFML lines indicated in black are (increasing from right to left): α= 0.02, 0.10, 0.20, 0.30, 0.60, 0.70, and 0.80. 62

Figure 4.5 Calculated activation energy as a function of mass loss based on the Friedman plot in Figure 4.4. 63

Figure 4.6 Ozawa-Flynn-Wall plot of the thermograms in Figure 5.3. CFML lines indicated in black are (increasing from right to left): α= 0.02, 0.10 to 0.90 by 0.10 increments, and 0.98. 64

Figure 4.7 Calculated activation energy as a function of mass loss based on the Ozawa-Flynn-Wall plot in Figure 4.6. 65

Figure 4.8 Surface plot of the relative permittivity as a function of both temperature (-140 °C - 160 °C) and frequency (10^{-1} - 10^{6} Hz). 66

Figure 4.9 Surface plot of the imaginary permittivity as a function of both temperature (-140 °C - 160 °C) and frequency (10^{-1} - 10^{6}) Hz. 67

Figure 4.10 The model fit (blue line) of the measured imaginary permittivity of BMI resin at 183 K (-90 °C) from 0.1 Hz to 1 MHz. Model fit parameters are found in Table 4.1. 68

Figure 4.11 The model fit (blue line) of the measured imaginary permittivity of BMI resin at 203 K (-70 °C) from 0.1 Hz to 1 MHz. Model fit parameters are found in Table 4.1. 69

Figure 4.12 Arrhenius plot of the natural log of the maximum frequency for the relaxation at each temperature. Red line shows a linear fit with a calculated activation energy of 43 kJ/mol from the slope. 71

Figure 5.1 Temperature cure cycle for the BMI/glass-fiber composites (RM-3002). Vacuum was pulled initially, followed by venting and application of 586 kPa of pressure for the remainder of the cure cycle. 76

Figure 5.2 Schematic diagram showing the resultant fractured halves of the composite samples after compression testing. Multiplication of the width in the area between the two notches (w) and the failed length (l) leads to the failed area, and is utilized to calculate the ILSS in Equation 5.2. . 77

Figure 5.3 Mass loss percentages of cured BMI resin at five different heating rates: 2, 5, 10, 20, and 50 °C/min. 78

Figure 5.4 Temperature derivative of the weight percentages in Figure 5.3. 79

Figure 5.5 IR spectra for unaged BMI resin (bottom, solid) and 8-harness satin 8871 style E-glass fiber weave obtained from constituent measurements of BMI/glass-fiber composites, as outlined in [11](top, dashed). While feature and peak locations are maintained, intensity comparisons between the two spectra should not be assessed. 83

Figure 5.6 Percent of sixteen-ply (circles) and eight-ply (triangles) composite mass lost at each aging temperature. Error bars represent one standard deviation above and below the average of ten samples (sixteen-ply) and three samples (eight-ply). Inset shows natural log of percent composite mass loss, at each aging temperature. 84

Figure 5.7 Relative permittivity results for eight-ply composite samples. Each spectrum represents the average of nine spectra, with error bars representing one standard deviation above and below the average. 85

Figure 5.8 Dissipation factor results for eight-ply composite samples. Each spectrum represents the average of nine spectra, with error bars representing one standard deviation above and below the average. 86

Figure 5.9 The real permittivity results for aged BMI resin. 87

Figure 5.10 The dissipation factor results for aged BMI resin. 88

Figure 5.11 DSC scans for uncured and aged composites (exotherm up). Aged composites show no exothermic signals. 89

Figure 5.12 Derivative of the DSC scans in Figure 5.11 for uncured and aged composites. 90

Figure 5.13 DSC scans for aged BMI resin (exotherm up). Aged resin samples show no exothermic signals, but do show crystallization endotherms. 90

Figure 5.14 Derivative of the DSC scans in Figure 5.13for aged BMI resin. 91

Figure 5.15 Interlaminar shear strength values for sixteen-ply composites at their corresponding aging temperatures. Error bars represent one standard deviation above and below the average of ten samples. 91

Figure 5.16 Photoacoustic spectra measured from six differently aged composite samples. The spectra are normalized to the 2200 cm^{-1} band as a minimum, and 1395 cm^{-1} for the maximum. A sequential decrease in the carbonyl band around 1720 cm^{-1} was observed as the aging temperature increased. Each spectrum is the average of six sample measurements. . 92

ACKNOWLEDGEMENTS

There are many people who have helped me throughout my time at ISU. I would like to thank my major professor Dr. Nicola Bowler for putting up with me for four years, for her excellent guidance, and for being an great researcher to aspire to. I would also like to thank Dr. Scott Beckman, Dr. Vinay Dayal, Dr. Ronald Roberts, and Dr. Xiaoli Tan for serving on my committee. I would also like to thank Dr. Samy Madbouly for serving on my early committee, and for his insights and guidance. Additionally, I have to thank Dan Barnard for his time and immense help with the fiber-reinforced composites work, and Roger Jones for his help and guidance with photoacoustic spectroscopy.

I would also like to thanks my groupmates in the EMDC group: Robert Sheldon, Weixing Sun, Rui Ding, Shuaishuai Liu, Nathan Kleppe, Amin Gorji, and Jin Liu for their guidance, helpful talks, and friendship throughout my time at ISU. Many other grad students have been instrumental to my development: Tim Cullinan, Ryan Gebhardt, Perry Antonelli, Brittany Curtis, Mitch Rock, Danny Vennerberg, Hannah Bygd, Peter Hondred, and countless others.

Finally, I would like to thank Brian, Dennis, and Carl Wilson, as well as Al Jardine, and, I suppose, Mike Love, for their discussions on good vibrational theory.

ABSTRACT

Polymer-matrix composites (PMCs), material systems made of two or more phases, are increasingly being utilized in aerospace applications due to their high strength-to-weight ratios and corrosion resistance. The present reasearch investigates two different types of PMCs: particle-reinforced and fiber-reinforced.

To adequately describe some surprising properties that are observed in polymer-matrix composites reinforced with nanoscale filler particles, a three-phase theoretical model is proposed that is suitable for describing the effective permittivity of polymer-matrix composites containing spherical nanoparticles. The model accounts for the presence of an interphase region, which takes on a dominant role in influencing properties of nano-filled composites due to the large surface-area-to-volume ratio of nanoscale fillers.

Regarding fiber-reinforced PMCs, spectroscopic techniques have been utilized to determine indicators of composite aging due to thermo-oxidation which are generally undetected by other non-destructive methods, such as ultrasonic testing. Two aerospace composite systems, bismaleimide/glass-fiber and epoxy/carbon-fiber, are thermo-oxidatively aged at a variety of temperatures. Both aged systems are analyzed via photoacoustic spectroscopy, an abosorbance-based IR spectroscopy technique, while the bismaleimide/glass-fiber system is also analyzed dielectrically. Spectroscopic properties are correlated with interlaminar shear strengths to determine the viability of particular degradation indicators and it is observed that changes in permittivity and dissipation factor of bismaleimide/glass-fiber both correlate well with reduction in interlaminar shear strength due to thermo-oxidative aging. The degradation is characterized through kinetic modeling, and the rates and activation energies of the degradation are extracted. Finally, dielectric properties as a function of temperature are measured for bismaleimide resin, and a major relaxation is modeled and characterized.

CHAPTER 1. INTRODUCTION

1.1 Research Question

The first goal of this research is to explain discrepancies between theoretical predictions and experimental measurement of dielectric properties of nanoparticle-filled structural polymers. The approach is to use of a new model which allows for the existence of a third phase in the material system - an interphase region - with properties distinct from those of either the polymer matrix or the nano-filler. The second goal is to identify new non-destructive indicators of polymer aging, due to thermo-oxidative processes, in structural polymer-matrix composites. By correlating measured permittivity spectra and infrared spectra with mass loss and inter-laminar shear strength of thermally-aged structural polymer matrix composites, key indicators of mechanical performance are obtained, that can be measured nondestructively.

1.2 Composites in Aerospace

A continuous hurdle in the production, manufacture, and repair of structural vehicles is reducing weight and long-term cost while maintaining or improving structural integrity. In addition to improvements solely in design, one common way in which this hurdle is overcome is through replacing conventional materials by composite materials. In the aerospace field, composites have been incorporated into structures since the 1960s [12] and their presence in aircraft has increased since.

Between the 1960s and the early 1980s, the percentage of composites comprising the aircraft was no more than five percent [13]. The U.S. Air Force began using carbon-fiber parts in the early 1980s to improve their warplanes [14]. This sparked interest in the commercial industry, and the mid 1980s saw a rise in composite weight percentage up to ten percent for the McDonnell

Douglas F-18A, and ten to fifteen percent for the Airbus A320, which had a composite tail assembly [13, 15]. Throughout the next two decades composite percentages showed minimal increases, generally staying around or below twenty percent. Around 2005, however, the Airbus A380 was released with a greater than twenty percent composite structure, and containing a center wing box which was made up of over fifty percent composites [16, 3]. A brief history of this increased usage of composites is shown in Figure 1.1, from [3].

More recently, composites have comprised fifty percent or more of the structure of some of the largest available commercial aircraft: the Boeing 787 [17] and the Airbus A350 [18]. Weight savings due to composites can result in large, long-term fuel burn savings: up to $430 for regional jets and $715 for jumbo jets per year, per pound of weight savings [19]. Other manufacturers who are conversely using composites less, such as Mitsubishi with their Regional Jet, are discovering that comparable weight savings are not as easily achieved as with composites [20].

Additionally, long-term costs such as inspection and repair can be reduced by using composites. On the Boeing 777, the tail is comprised almost entirely of composites. Conversely, the Boeing 767, one generation earlier, has a tail made of aluminum. Although the metal tail on the 767 is 25 percent smaller than the composite tail of the 777, the composite tail requires 35 percent less labor hours than the metal tail [17]. This reduction is due to metals having a higher corrosion risk, compared to their composite counterparts.

On the astronautics side, composites are also experiencing more use. SpaceX is utilizing composite fairings in both their Falcon Heavy and Falcon 9 rockets [21, 22]. Additionally, in NASA's Space Shuttle Fleet, composite overwrapped pressure vessels have been made using composite coatings since the 1970s [23]. This trend of composite usage in all aerospace fields is increasing. In the following section, composite materials for these applications are discussed in more detail, along with the particular materials which are studied in this research.

1.3 Composite Materials

Composites are materials made up of two or more constituents, which can be designed to capitalize on the properties of each constituent. For instance, carbon fibers perform extremely

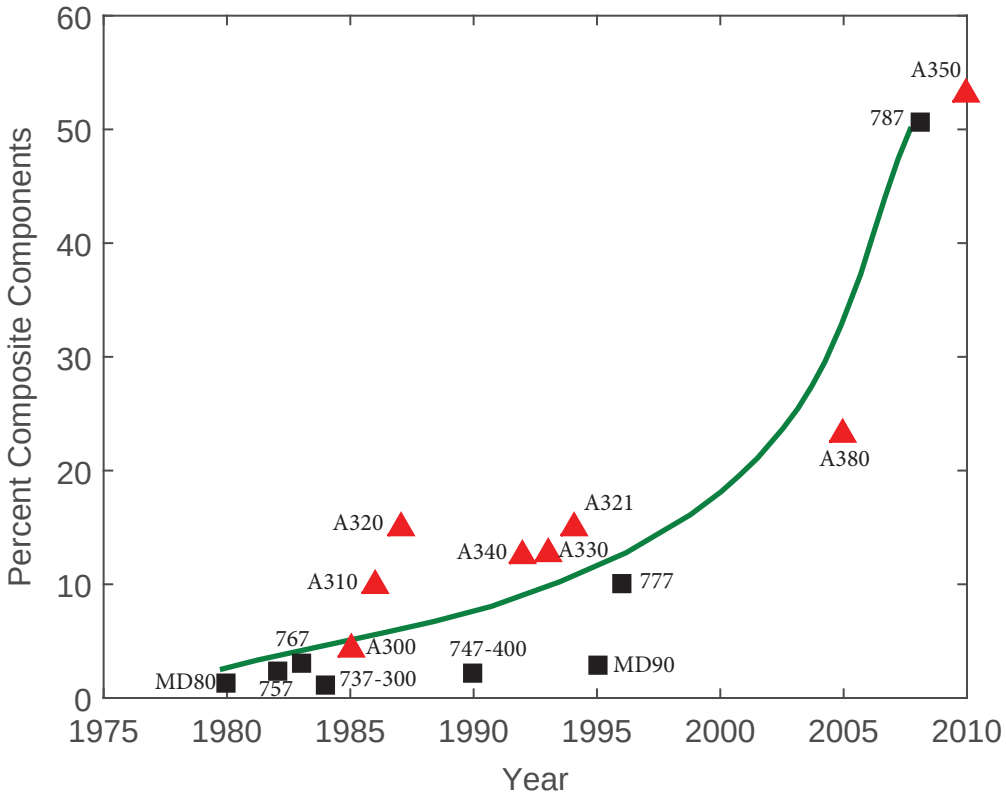

Figure 1.1: Percentage of composite usage in the structure of a variety of aircraft, redrawn from [3]. Black squares represent Boeing aircraft, and red triangles represent those of Airbus.

well in tension, but buckle under compression. When aligned within a matrix, however, the fibers can exercise their strength in tension, while the matrix supports small compressive stresses and helps transfer loads to the fibers. In general, for a two-phase composite, the constituents are categorized as either a reinforcement (filler) material, or as a matrix (host) material. Reinforcing materials can be separated into two categories: particle and fiber. Particle fillers can be of different materials (polymer, ceramic, metallic), shapes (spheres, rods, plates), and sizes (micrometer, nanometer), and are usually found as a minor component compared to the matrix. Additionally, when particle fillers are dispersed in a matrix, they can have various orientations (aligned, random) as well as different degrees of dispersion (agglomerated, exfoliated, intercalated).

In contrast, fiber-reinforced composites do not contain dispersions of particles, but instead contain long, continuous or discontinuous fibers in majority fractions compared to the matrix.

The fibers can be made out of carbon [24], boron nitride [25], glass [26], or other materials. Fiber-reinforced composites are typically used in 'prepreg' form, where the fibers are pre-impregnated with matrix material to form long rolls. Prepregs can be found with a variety of fiber forms, including unidirectional tapes, and a large variety of weaves (plain, satin, twill, etc.). These prepregs can be molded or cut into laminae which can be stacked in various ways (aligned fiber directions, perpendicular fiber directions, angled fiber directions) prior to curing.

Matrix materials for structural applications can be thermoplastic polymers, but are most often thermosetting polymer resins, such as epoxy or bismaleimide [19]. For thermosets (and some thermoplastics), specific amounts of energy (provided via heat and occasionally spurred by catalysts) lead to individual polymer chains cross-linking with one another to form a larger network. This so-called 'curing' process 'sets' the polymer in place, greatly increasing its strength, and, unlike thermoplastics, prevents it from flowing at elevated temperature.

Bismaleimide (BMI) is a thermosetting polymer resin with excellent high temperature stability which makes it an appealing candidate as a matrix for reinforced aerospace composites [27]. A type of thermosetting polyimides, bismaleimides are synthesized from a variety of monomer units containing maleimide end groups, and by a variety of synthesis methods [28]. A representative BMI unit is shown in Figure 1.2. In prepreg form, BMI is often found with glass or carbon fiber reinforcement. Part of this research considers a BMI/glass-fiber composite.

Similarly, epoxy is a thermosetting polymer that is made from a resin mixed together with a hardener, which helps initiate the curing process. Epoxies are also high-temperature resistant, making them ideal candidates for aerospace applications. However, due to the high crosslink densities observed in epoxies, they can often be brittle [27]. To counteract this brittleness, epoxies can be toughened by adding rubbers or other elastomers. As with BMI, epoxies are usually found with a variety of fiber reinforcements. This research considers carbon-fiber reinforced toughened and untoughened epoxy.

Once the laminae are stacked or molded, they are placed in an autoclave or heat press, where they are cured in a vacuum bag. Vacuum bagging procedures differ depending on the materials involved, the desired product, and the shape of the composite or mold. For instance, a sixteen-laminae composite will have a different bagging setup, and be subjected to a different

heating profile, then a large tail fin for an airplane. In general, however, a basic vacuum bag is made-up of different layers, as follows.

On the outside is the vacuum bag itself, usually a high-temperature resistant, pliable plastic material. This material, as well as the others described next, is often rated for different temperature ranges and can be selected to fit the particular cure cycle called for. Inside the vacuum bag layer is generally a cloth known as the 'bleeder'. The bleeder absorbs excess gases and resin that might flow out of the laminate during the curing process. This helps to keep the composite uniform, whereas the absence of a bleeder could lead to excess resin patches on top of or within the composite. To further control the flow of resin, this material can be both porous or nonporous. Next is the so-called 'breather' cloth. The breather allows for the pulled vacuum to reach all areas of the composite, instead of getting stuck and cutting the vaccuum. Oftentimes the breather and bleeder are combined into one cloth. Directly in contact with the composite on both sides are release films. These are porous or non-porous (depending on desired resin flow and surface texture) sheets that allow the laminate to be 'released' after the curing procedure is finished and the vacuum bag cut open.

In order to seal the bag well enough to pull a strong vaccuum, sealant tape is used all around the composite and additional cloths and films. Sealant tape is a rubber-based tape that can also withstand high-temperatures, and is easy to cut and apply. Additional sealant tape is used to seal the vacuum tube, which is inserted into the corner of the vacuum bag (not in contact with the sample), and covered with breather cloth to allow uninterrupted pull. A representative image of a vacuum bagging layup for a square-foot laminate is shown in Figure 1.3.

To measure the mechanical strength of composite laminates, a variety of standards and tests have been created and used. Some tests include three-point bend tests for flexural properties [29], short-beam shear tests for interlaminar shear strength [30] and double-notch shear test for interlaminar shear strength [31], among various other ASTM and ISO standard tests. The double-notch shear test has been used in this research to determine the interlaminar shear strength (ILSS) of aged composite samples. In the proceeding chapters, a more detailed description will be given, or can be found in [32], with additional reference to [33].

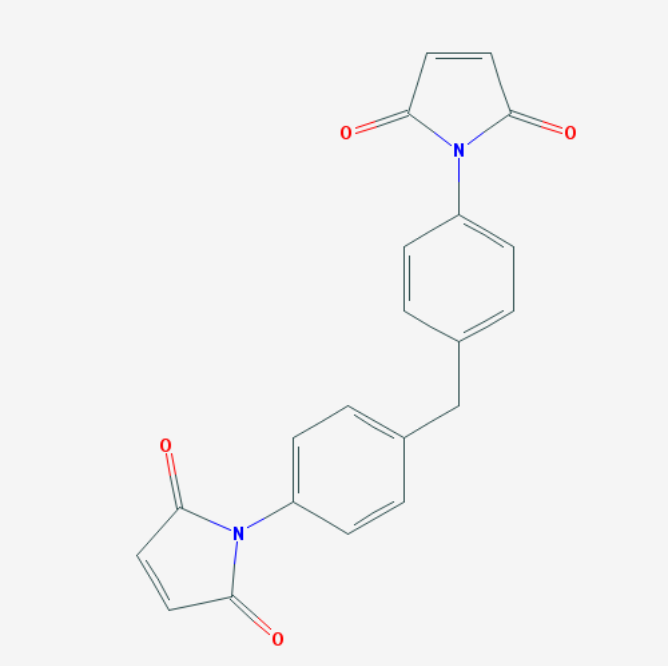

Figure 1.2: A representative bismaleimide unit. Image obtained from [4].

1.4 Non-Destructive Evaluation of Composites

As with metallic and other non-composite structures, in-service evaluation of composite structures is extremely important for safety assurance and cost efficient repairs. This evaluation can generally be performed via two methods: destructive evaluation (such as the compression tests described above), and non-destructive evaluation (NDE). Destructive testing involves the cutting, breaking, or other large destruction of the sample material in question, rendering it useless in its original application. NDE, however, uses ultrasonics, various forms of electromagnetic radiation, and other techniques which leave the sample in question intact, and viable for further use in its current application. NDE provides the ability to observe changes in the same structure over a period of time, which can help lead to identifying precursors to failure. One manifestation of NDE is known as structural health monitoring (SHM), and is characterized by receiving frequent or continuous signals from embedded or permanently attached sensing networks. SHM can help in predicting remaining useful life of structures.

In assessing the serviceability of fiber-reinforced composites non-destructively, a wide array of techniques is available, as mentioned above. One of the most widely used techniques, however,

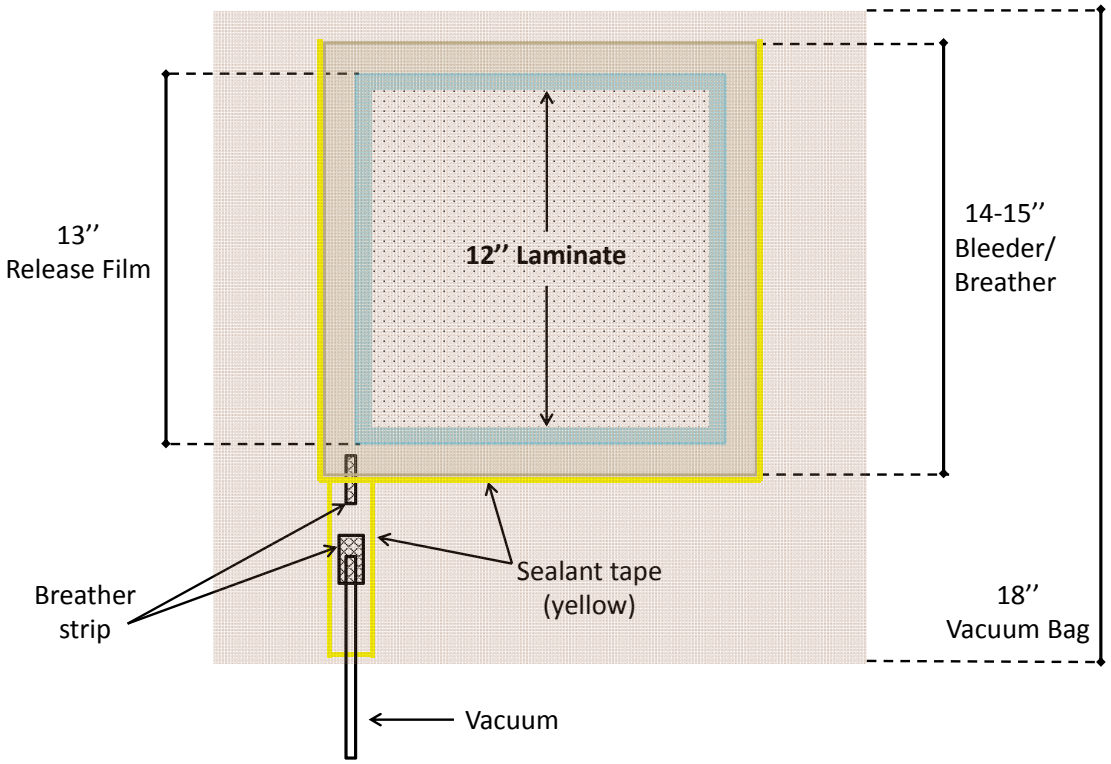

Figure 1.3: Top-down view of a representative vacuum bagging layup for a square-foot laminate. This schematic is not to scale.

is ultrasonic testing (UT). UT utilizes high energy sound waves which propagate through a material [34]. In one example, involving a pulser/receiver, an acoustic pulse is sent through the sample by the pulser, and any reflected waves are picked up by the receiver. When a defect is present, such as a disbond or delamination, the wave will be reflected back to the receiver. If no defects are present, the opposite wall of the composite will reflect the sound wave back, taking longer than the deflect-reflected wave.

Although it has been shown to be useful for detecting acute damage such as disbonds and delaminations, impact failures, some mechanical fatigue, and for recognizing environmental effects such as moisture absorption, the NDE of degraded composites due to thermal oxidation has not been highly researched. One study has shown the promotion of microcracks due to thermal aging [35], and others have discussed how to utilize UT to detect them [36, 37]. There is still more work to be done in this area, however. In particular, since oxidation of polymers often leads to changes in their dielectric properties, this research investigates the suitability

of capacitive NDE and FTIR spectral measurements for assessing degradation of structural composite materials.

1.5 Multiphase Modeling

In composite materials, or other multi-phase systems, the addition of new phases is primarily utilized to modify the properties of the host material. Oftentimes, however, it is difficult to know how much of a particular filler material is required so that the resulting mixture has the new, desired properties. Additonally, it sometimes desired to determine the property value of an unknown inclusion. In the case of dielectric properties, a variety of mixture models are available that accurately describe the behavior of multiphase mixtures.

One of the most famous mixing models is the so-called Maxwell-Garnett formula [38]. This relationship describes the effective permittivity of a two-phase mixture based on three parameters: the permittivity of the environment phase ϵ_e; the permittivity of the inclusion phase ϵ_i; the volume fraction of the filler phase ϕ. The Maxwell-Garnett formula for a two-phase system with spherical inclusions is shown below.

$$\epsilon_{\text{eff}} = \epsilon_e + 3\phi\epsilon_e \frac{\epsilon_i - \epsilon_e}{\epsilon_i + 2\epsilon_e}$$

The fractional term in the above relationship is derived from the Claussius-Mossotti equation, which will be described later in Section 1.6.1.

More complex scenarios, such as three or more phases or non-spherical inclusions, can become exceedingly difficult to model. To improve the ease of analysis for these types of systems, bounds are often used as general guidelines for what the effective permittivity could be. One of the most general sets of dielectric bounds are the so-called Wiener bounds [38]. For a simple two-phase system, the upper Wiener bound can be written as

$$\epsilon_{\text{eff}} = \phi_i\epsilon_i' + (1 - \phi_i)\,\epsilon_e'$$

with the lower Wiener bound as

$$\frac{1}{\epsilon_{\text{eff}}} = \frac{\phi_i}{\epsilon'_i} + \frac{(1-\phi_i)}{\epsilon'_e}$$

These bounds are representative of capacitors in a circuit connected in parallel (maximum bound) or in series (minimum bound). For more than two phases, additional volume fraction and permittivity terms can be added for each extra phase. The effective permittivity of the multiphase mixture will lie either on or between the Wiener bounds.

1.6 Characterization Techniques

In this study, two main NDE techniques will be investigated to determine their suitability for monitoring the thermal degradation of composite materials: dielectric spectroscopy and Fourier transform infrared photoacoustic spectroscopy.

1.6.1 Dielectric Spectroscopy

Unlike conductors, which allow the free flow of electrons in an electric field, a dielectric material resists the flow of electrons in an electric field. This leads to a separation of charges in the material: positive charges will move in the direction of the field, and negative charges will move away from the field direction. The material is then polarized. At the level of electrons, this can be represented by the electron cloud around an atom shifting off-center from its resting position outside of the field. This separation of charge creates a dipole moment, which is in the direction of the field. For two point charges, $+q$ and $-q$, separated by a distance d due to the electric field, the dipole moment can be represented by

$$\vec{p} = q\vec{d}$$

Therefore, the greater the charge, or the greater the separation of charge, the greater the dipole moment. This represents a Coulombic attraction which keeps the two charges from traveling towards the appropriately charged electrode. Once the electric field is removed, however, the electron cloud will eventually return to its original resting position. Since this dipole moment is induced by the electric field, it is known as an induced dipole.

On larger scales, many molecules are polar, meaning that they naturally contain dipoles due to the connectivity of their atoms. A simple case of this is the water molecule. Since the oxygen atom of the water molecule is more electronegative than the two hydrogen atoms, a dipole exists from the positive center of the hydrogen atoms, to the negative center of the oxygen atom. Because the charges are already separated, when this dipole is placed in an electric field, it attempts to align itself with the field. If the molecule is not already aligned, it will experience a torque which attempts to align it to the field. Eventually, this torque will cause the molecule to rotate and become aligned with the field. When the field is removed, the dipole will then rotate into a random orientation due to thermal agitation.

The intensity of the dipole moment and also be represented as a fraction of the electric field. This scalar factor is known as the polarizability, and represents an entity's tendency to polarize in an electric field, or the ease with which a dipole aligns itself with an electric field. For a bulk material, all the atomic polarizabilities can be related to a macroscale parameter: the dielectric constant, ϵ_r'. This relation, known as the Clausius-Mossotti relation, is shown below [38].

$$\frac{\epsilon_r' - 1}{\epsilon_r' + 2} = \frac{N_A \alpha}{3\epsilon_0}$$

The dielectric constant is the real component of the permittivity, ϵ^*, a complex number. The imaginary component is known as the dielectric loss, ϵ''.

Due to the charges in the material being separated and generally aligned, there is a large amount of charge built up within the material. This leads to a net dipole moment across the entire material. The energy due to the charge built up can be characterized by the capacitance. The capacitance is the amount of charge within a material per voltage across it. In a simple case, the dielectric constant (also known as the relative permittivity) is the ratio of the capacitance between two oppositely charged electrodes with a dielectric sandwiched between compared to the system of electrodes without the dielectric.

For AC voltages, the capacitance, and therefore the dielectric constant, changes depending on the frequency of the oscillating voltage. As the electric field oscillates, the dipoles will also oscillate in their attempt to align with the field. At particular frequencies, certain dipoles

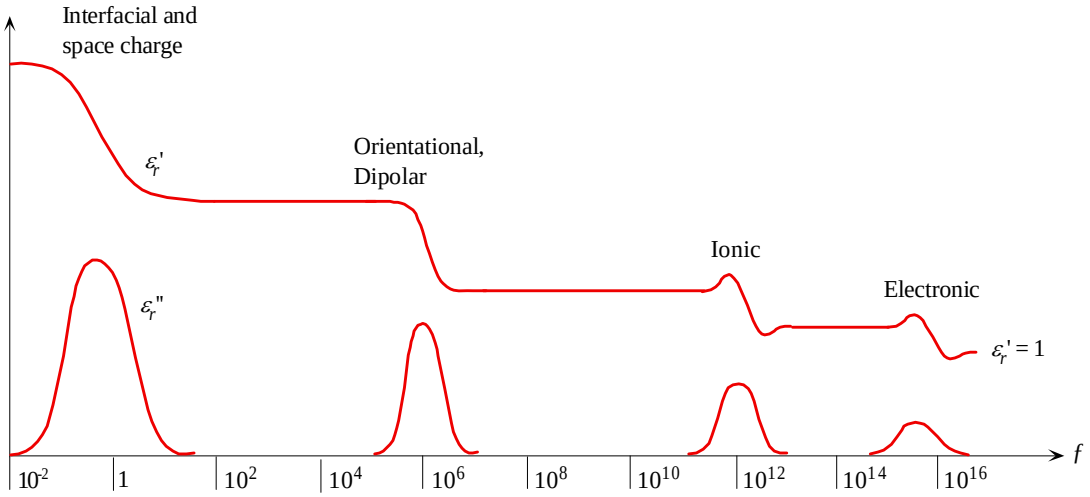

Figure 1.4: Schematic of different dielectric relaxations as a function of frequency as they occur in the dielectric constant (top) and the dielectric loss (bottom), from [5].

will be unable to keep up with oscillating field, and will 'relax', resulting in a decrease in the dielectric constant, and a peak in the dielectric loss. There are a variety of relaxations that can take place, depending on the type of dipole in question. An example of the main types of relaxations (dipolar, ionic, electronic), and their general relaxation frequencies, are shown in Figure 1.4.

Dielectric spectroscopy is the measurement of the permittivity of a material as function of frequency. This research investigates the changes in dielectric spectra from molecular changes due to thermal degradation.

For the investigated materials in this research, BMI and epoxy, only the dielectric spectra of BMI will be measured, due to conductive carbon-fibers being dispersed in the epoxy. While the dielectric properties of BMI have not been heavily researched, to the author's knowledge, other similar thermosets have, such as Matrimid ©, a polyimide [39]. Like most thermosetting resins, however, the dielectric constant of BMI is relatively stable at room temperature, for the frequency range 1 kHz to 1 MHz. This is primarily due to the rigid aromatic backbone of the BMI, which is what also gives the BMI its high-temperature resistance. Within this frequency range, however, unaged BMI does experience a dipolar relaxation, near 10^5 Hz. This is most likely due to the maleimide end groups, or possibly just the carbonyl groups on each end group.

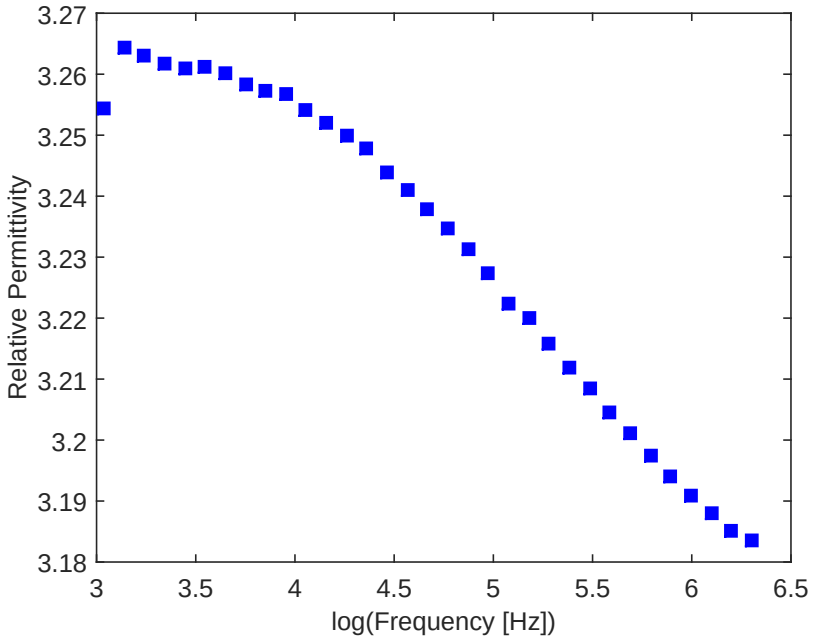

Figure 1.5: Measured relative permittivity of unaged, BMI resin from 1 kHz to 2 MHz.

Example plots of the BMI relative and imaginary permittivities are shown in Figures 1.5, 1.6.

1.6.2 Fourier Transform Infrared Photoacoustic Spectroscopy

Just as molecules respond differently to an electric field, they also respond differently to electromagnetic radiation. For polymeric systems in particular, infrared (IR) radiation interacts with different molecules, or more precisely different bonds, at characteristic frequencies. Atoms covalently bonded together are constantly oscillating, due to thermal agitation, at frequencies depending on the mass of the two atoms, and the strength of their bond. For example, a carbon-carbon bond will oscillate at a different frequency than a carbon-carbon double-bond, and both will be different from a carbon-oxygen bond. It is due to these characteristic bond frequencies that IR spectroscopy is utilized to characterize polymeric systems, or for identification purposes.

An IR spectrometer works primarily through what is called a Michelson interferometer [40]. Radiation from an IR source is directed into a beam-splitter (in the case of this research, a KBr beam-splitter) which splits the IR beam into two parts. One beam is sent towards a stationary mirror, and then reflected back to the beam-splitter. The second beam, on the other hand, is reflected towards a movable mirror, and then reflected back to the beam-splitter. At

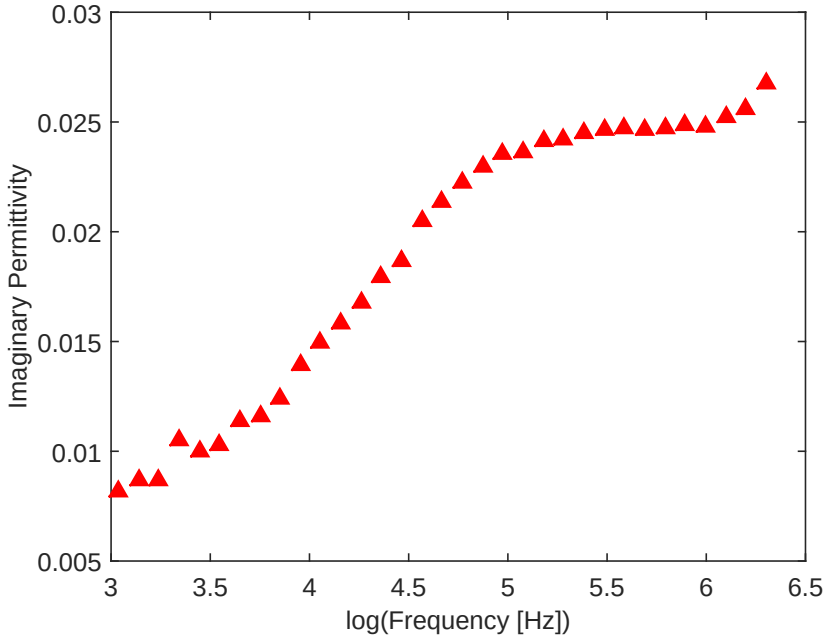

Figure 1.6: Imaginary permittivity of unaged, BMI resin, from 1 kHz to 2 MHz.

the beam-splitter, the two beams recombine and are directed towards a sample. If the two mirrors are the same distance apart, or optically with a $n2\pi$ phase difference ($n = 1, 2, 3...$), from the beam-splitter, then they will recombine constructively. Otherwise, they will not fully recombine, as there will be varying amounts of destructive interference.

In transmission IR spectroscopy, the recombined beam will be directed towards a sample, and the transmitted signal will be picked up by a detector on the other side of the sample. From the intensities picked up by the detector, a plot of the intensity as a function of the movable mirror distance (from either side of the equidistant point) can be created. This plot is known as an interferogram. Instead of detecting what is transmitted through a sample, photoacoustic spectroscopy (PAS) detects what the sample absorbs. This is done in a photoacoustic cell, which holds the sample, the sample cell, a microphone, and an IR-transparent gas (in the case of this research, helium). As the sample absorbs the radiation, it begins to heat the surface of the sample. This heat flows from the surface to the surrounding gas, causing it to expand. Since in PAS the IR radiation is intensity modulated at a particular frequency (in the case of this research, 2.5 kHz), the gas will experience oscillating expansion and contraction at the

modulation frequency. This creates an acoustic wave which can be picked up by the microphone in the cell. An interferogram can be made from the amplitude of the acoustic waves and the off-center distance of the mobile mirror.

From an interferogram, the data can be manipulated via a mathematical procedure known as a Fourier transformation. Essentially, the Fourier transform converts the amplitude or intensity as a function of off-center distance (usually defined in cm), and transforms it into a function of inverse distance (cm^{-1}). The units of cm^{-1} are referred to as wavenumbers, and are related to wave frequency.

As previously mentioned, IR spectra can be used to characterize polymeric materials. This is done through radiation being absorbed by particular bonds at characteristic wavenumbers. Some bonds can absorb a few different wavelengths, however, depending on the type of motion associated with it. Examples of different vibrations are bond stretching, bending, wagging, and rocking. One common characteristic bond stretch, a carbon-oxygen double bond, occurs near 1720 cm^{-1}. This carbonyl bond stretch is represented as a strong peak. Conversely, the oxygen-hydrogen bond of hydroxyl groups is represented as a broad, shallow peak around 3000 cm^{-1}. These two wavenumbers are general locations for these absorptions, as the atoms they're attached to play a role in determining at what wavenumber they're absorbed.

An example IR spectra of neat BMI resin is shown in Figure 1.7.

1.7 Thesis Organization

The following chapters of the thesis will in greater detail explore multiphase dielectric modeling and the potential indicators that can be detected with the above NDE spectroscopic techniques. In Chapter 2, a theoretical model to describe multiphase composite materials with nanoparticle dispersions is proposed. This model incorporates an interphase, and results propose particular dimensions and characteristics of this phase. Chapter 3 analyzes a carbon-fiber/epoxy (CFE) composite with IR spectroscopy to determine correlation with interlaminar shear strength values. Degradation kinetics of the CFE are also analyzed.

Chapter 4 looks at the degradation kinetics of BMI resin, as well as dielectric changes in the resin as a function of temperature. Additionally, dielectric models are fit to the data

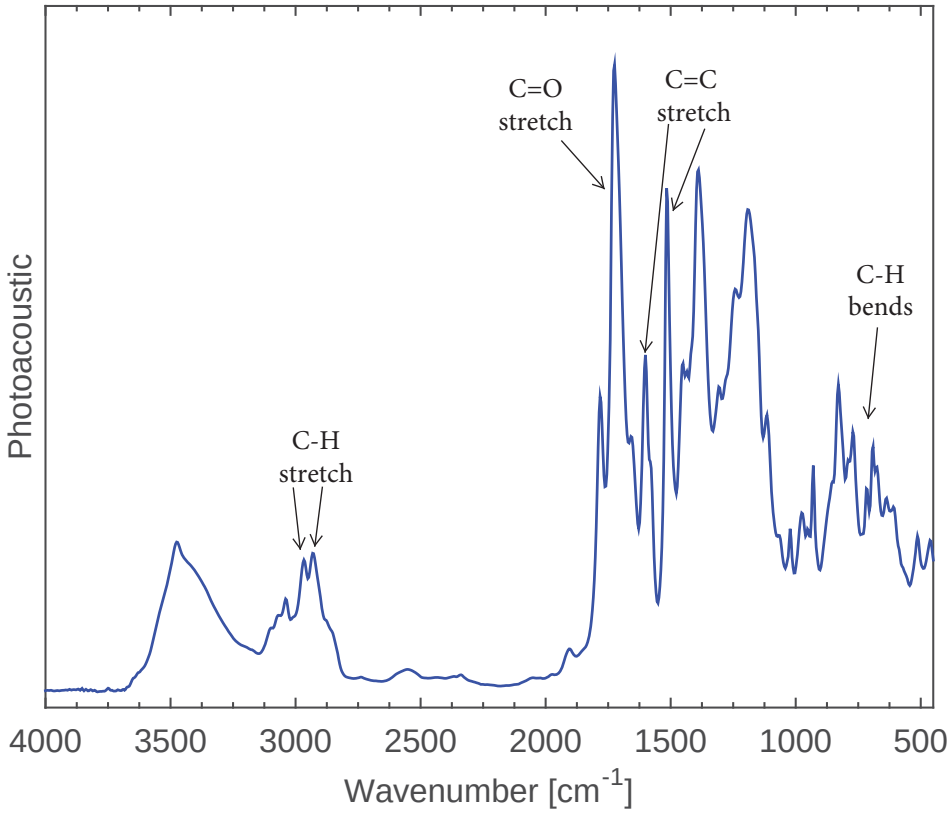

Figure 1.7: Example IR spectra for neat BMI resin. Indicated peaks are C=O stretch ∼1720 cm^{-1}, aromatic C=C stretching ∼1500 and 1600 cm^{-1}, aromatic C-H bending ∼650-750 cm^{-1}, and aliphatic C-H stretching ∼2850-3000 cm^{-1} [6, 7].

to extract the activation energy of a major relaxation. In Chapter 5, a thermo-oxidatively aged BMI/glass-fiber system is analyzed with dielectric and IR spectroscopy. These results are correlated to interlaminar shear strength values to determine which indicators are the most applicable. Finally, conclusions are summarized in Chapter 6, along with proposed future works.

CHAPTER 2. MODELING THE INTERPHASE OF A NANODIELECTRIC THERMOSET

Modeling the Interphase of a Nanodielectric Thermoset

C. Daily, W. Sun, M.R. Kessler, X. Tan, N. Bowler

Materials Science and Engineering, Iowa State University, Ames IA 50011, USA

Published in *IEEE Transaction on Dielectrics and Electrical Insulation*, 2014.

Abstract

A three-phase theoretical model is proposed that is suitable for describing the effective permittivity of polymer-matrix composites containing spherical nanoparticles. The model accounts for the presence of an interphase region, which surrounds each nanosphere, whose permittivity is allowed to be different from that of the matrix polymer. The nanoparticles themselves are approximated as hard (non-overlapping) spheres, whereas the interphase regions of neighboring nanoparticles are permitted to overlap. The volume fraction of the interphase region is computed by assuming that the nanoparticles are arranged on the nodes of a simple-cubic lattice. The effective permittivity of the composite is subsequently computed via three-phase Wiener bounds. As an example application of the model, permittivity data measured on a silicon/bisphenol E cyanate ester nanodielectric is shown to lie outside the range of the two-phase Wiener bounds yet lies within the range of the three-phase Wiener bounds with appropriate choice of interphase permittivity and thickness.

2.1 Introduction

The study of polymer-based dielectrics has been ongoing for the past half century [41], with dielectric relaxations for many main polymer classes being well understood. Chain structure modifications and orientation changes, and their effect on dielectric relaxations, can also be explained. The study of polymer-based nanodielectrics has emerged more recently out of observations of enhanced mechanical and other property improvements in polymer-based nanocomposites. Pioneering work in the field of nanodielectrics was conducted by Nelson et al [42] in 2002, where epoxy composites filled with nano-sized titania (TiO2) displayed slightly reduced permittivity values, when compared to their micro-filled counterparts. This lead to the discovery that the titania nanoparticles were inhibiting chain mobility, and the authors began proposing the idea of interaction zones, a region of highly immobilized chains (1-2 nm) near the filler surface surrounded by highly altered chains that affect composite property changes. In the decade since, the number of works based on the study of polymer-based nanodielectrics has increased significantly, with entire books now devoted to the subject [43].

In 1994, Lewis [44] discussed the phenomenon of an interfacial region that exists between two dielectric media and displays properties that differ from those of its two constituents. As nanofillers of any shape (with at least one dimension less than 100 nm) possess higher surface area-to-volume ratios than their micro-sized counterparts, an interfacial region along the surface of nanofillers is more influential in dictating the properties of the nanocomposite than it is for a microcomposite. In 2004, Lewis again brought interfaces to the forefront of the nanodielectrics discussion, going so far as deeming interfaces and nanodielectrics inextricable [45]. His proposal of a volumetric, interfacial region was soon termed by many as the interphase, and various attempts were made to characterize its properties and chemistry.

In 2005, Tanaka [46] proposed a multi-core model which divided the interphase into three layers, building upon the two-layered interphase proposed by Tsagaropoulos [47], each with their own unique chemistry, to help describe how the interphase influences nanocomposite properties. In the same year, Roy et al [48] showed, among other things, that changes in chain mobility, indicative of an interphase presence, can be identified through changes in the glass transition

temperature of nanofilled composites. More recently, Raetzke et al [49] explained improvements in high-voltage arcing resistance of silicone/SiO2 nanocomposites with an interphase volume model; a model based on nanoparticles with overlapping interphases positioned on the lattice points of a body-centered cubic lattice. Todd and Shi [50] proposed a mixture model based on polarizability calculations to determine the permittivity of an interphase layer, as well as an overlap probability function to determine its thickness. Later, Todd and Shi [51] proposed an interphase power law which calculates the effective composite permittivity using a three-phase power law calculation. Pitsa et al [52] recently proposed a model to calculate the interphase permittivity, for use in examining how titania nanoparticles affect electrical treeing in epoxy, assuming that the interphase permittivity ranges from particle to matrix permittivity values and varies with respect to an exponential function. Also, Pitsa et al [53] published a detailed overview of many of the widely accepted theoretical interphase models, including those of Tsagaropoulos and Tanaka.

The proposition of an interphase has been able to help explain certain features or property changes that polymer composites based with nano-sized fillers provide in comparison to their micro-sized counterparts [49]. However, there are still many observations that have yet to be explained. One of these is an anomalous reduction in the relative permittivity of a nanocomposite at low filler loadings, whereby it is reduced below the relative permittivity of the neat, unfilled, matrix material. This anomaly has been shown to present itself in a wide variety of polymer-based nanocomposites, from thermosetting nanocomposites [54, 55, 9, 56], to thermoplastic nanocomposites [2], with fillers that may vary in size. The present work attempts to describe normal composite behavior [1], as well as this anomalous behavior, an extension of previous work [57], through the interphase using a multilayered nanofiller model, an approach that has been previously utilized.

Hanai [8] was one of the first to derive basic expressions for the dielectric constant of dispersions of multilayered fillers. In his calculations, Hanai considered a case where spherical particles surrounded by shells of finite thickness were dispersed dilutely in a dispersion medium, with each component of the dispersion having its own volume fraction and complex permittivity. Through this approach, he showed that dispersions of layered, spherical particles

experienced two dielectric relaxations, with respect to frequency. A number of previous models have also used a multilayered filler approach to help describe the frequency-based dielectric response of nanocomposites. Steeman *et al* [58] proposed an interlayer model, based on work derived by Maurer, to help explain dielectric measurements of water adsorption in a glass-bead filled matrix, where the water was represented by the interlayer. Using an approach similar to one which determines various mechanical moduli of polymer-based composites with the interlayer model, the authors derived an expression which described how the interlayer affected the effective composite permittivity. Similarly, Tinga *et al* [59] presented a solution to calculate the complex permittivity of a multiphase mixture, utilizing a confocal ellipsoidal shell that surrounded ellipsoidal nanofillers. Further, first-order effects of neighboring particles were included in the calculations. None of these models account, however, for any overlapping of the interlayer or shell.

We propose a three-dimensional theoretical model, based on a simple-cubic lattice, where monodisperse, inorganic nanoparticles of a finite radius and relative permittivity are fixed on each of the lattice points. Surrounding each nanoparticle in the lattice is an interphase layer of a finite thickness, with its own relative permittivity, which is allowed to overlap with neighboring interphase layers. Volume fractions of the three phases; nanofiller, interphase, and unperturbed matrix material, can be calculated analytically for any nanoparticle loading. Using the results in three-phase Wiener bounds, the effective composite permittivity can be modeled and a range of reasonable values for the interphase thickness and permittivity can be extracted. To the authors knowledge, this is the first work to offer a semi-analytical calculation of the bulk permittivity of a composite with overlapping interphases. The three-dimensional model will first be described in detail in Section 2, followed by an example of the dielectric analysis and extraction of interphase parameters in Section 4. Finally, the interphase parameters (thickness and dielectric constant) are presented for a silicon/bisphenol E cyanate ester nanodielectric, as well as a low-density polyethylene/alumina (LDPE/Al2O3) nanocomposite system for which the anomalous reduction of permittivity in the nanocomposite, below that of the matrix value, has been observed.

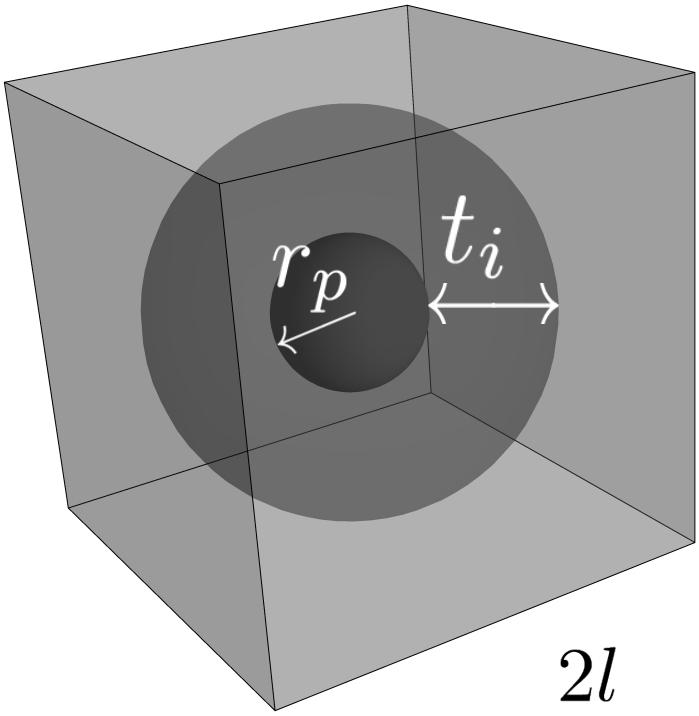

Figure 2.1: The first regime, containing a non-overlapping interphase.

2.2 Model

The three-dimensional theoretical model is proposed based upon hard, spherical nanoparticles with a surrounding interphase layer of discrete thickness that is permitted to overlap with neighboring interphase layers. The nanoparticles are centered on the nodes of a simple cubic lattice, such that three unique phases exist: unperturbed host material, the nanofiller, and the interphase. Calculating the volume fraction of each phase in a composite at a particular nanofiller loading is executed by analyzing a single unit cell of the lattice, side length $2l$. As the nanoparticle radius r_p and interphase thickness t_i are fixed, changes in the nanofiller loading are simulated by changing the size of the unit cell. Due to the geometry of the components of the unit cell, and the unit cell itself, four geometrical regimes arise for different filler loading and interphase thickness pairs, as shown in Figures 2.1, 2.2, 2.3, and 2.4. The calculation of the volume of unperturbed matrix material is provided below for each of the four regimes, and the resulting volume fraction calculations of the three phases follow.

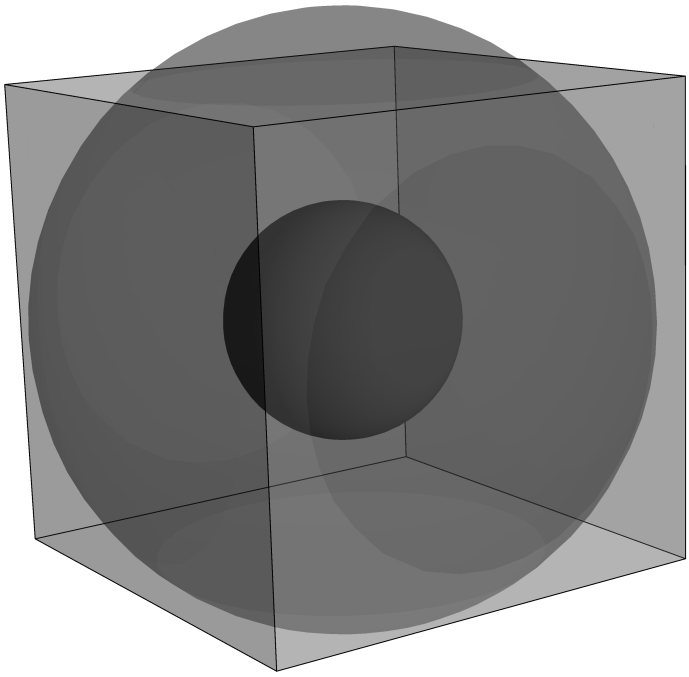

Figure 2.2: The second regime, where the interphase is overlapping through the unit cell faces.

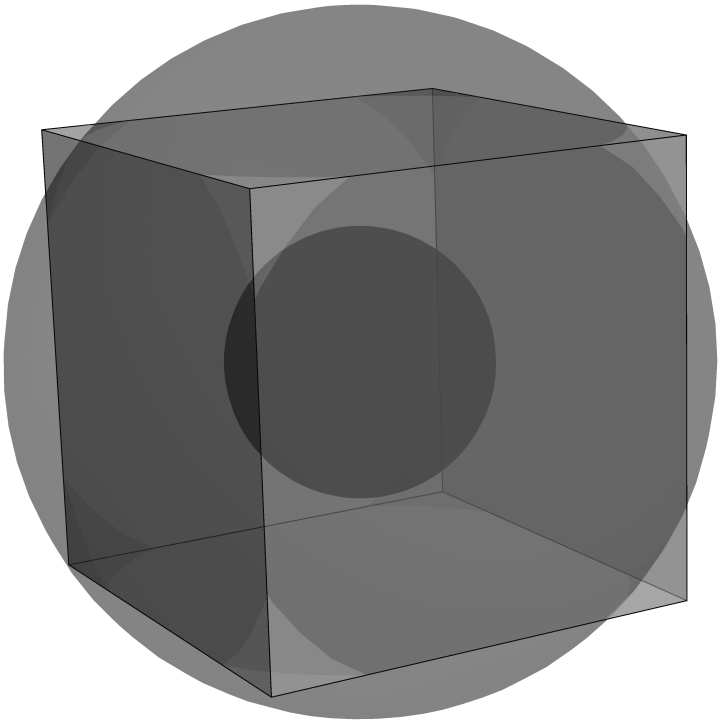

Figure 2.3: The third regime, where the interphase is overlapping through the cell faces and edges.

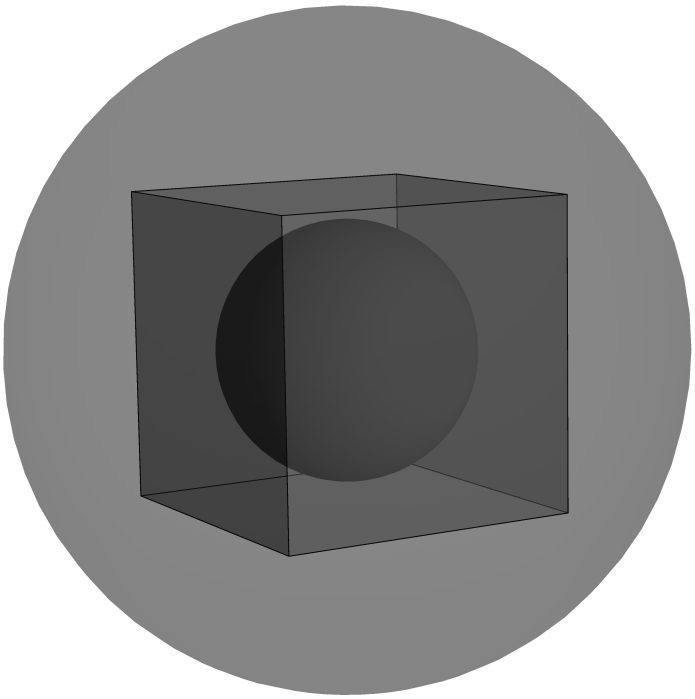

Figure 2.4: The fourth regime, where the matrix phase is entirely displaced by the interphase.

2.2.1 Regime One: Non-Overlapping Interphase

When the nanofiller loading is low, or when the interphase thickness is extremely small (on the order of a few nanometers), there is likely no interphase overlap. A unit cell representative of Regime One is shown in Figure 2.1. To calculate the volume of unperturbed matrix material, the volume of the interphase boundary (nanoparticle + interphase) is simply subtracted from the total unit cell volume. For any pair of nanoparticle radius and interphase thickness, the conditions and the calculation of the unperturbed matrix volume for Regime One are:

$$v_m = 8l^3 - (4/3)\,\pi r^3 \;;\; l \geq r \tag{2.1}$$

where v_m is the unperturbed matrix volume, l is the half length of a side of the unit cell, and r is the radius of the interphase boundary ($r = r_p + t_i$).

2.2.2 Regime Two: Interphase Overlap Through Cell Faces

As the nanofiller loading, or relative size of the interphase thickness, increases beyond those that fall under Regime One, the interphase layers begin to overlap. The overlap is shown in Figure 2.2 as six spherical caps protruding from each of the six sides of the unit cell. The volume of unperturbed matrix material can be calculated by using again subtracting the interphase boundary volume from the total unit cell volume, while adding the volume of the six spherical caps, which are no longer inside the unit cell. For any pair of nanoparticle radius and interphase thickness, the conditions and the calculation of the unperturbed matrix volume for Regime Two are:

$$v_m = 8l^3 - \left\{(4/3)\,\pi r^3 - 6\left[(1/3)\,\pi\,(r-l)^2\,(2r+l)\right]\right\}\ ;\ r/\sqrt{2} \le l \le r \tag{2.2}$$

2.2.3 Regime Three: Interphase Overlap Through Cell Faces and Edges

As the overlap of interphase layers of neighboring nanoparticles begins to increase above that found within the limits of Regime Two, the six spherical caps protruding from each side of the unit cell will begin to overlap with one another along the twelve edges of the unit cell, as shown in Figure 2.3. This increased overlap, due to an increase in filler loading or interphase thickness, makes the unperturbed matrix calculation increasingly complex. The material inside the unit cell, a cube with corners that become more, or less, rounded depending on the filler loading and interphase thickness, can be divided into sixteen equal parts. One of these sixteen pieces may be divided into five regions, each with its own volume calculation. The summation of all five regions, for all sixteen pieces, and subsequent subtraction from the total unit cell volume results in the volume of the unperturbed matrix material. The equations for each of the five regions can be found in Appendix A, and the final calculation of the unperturbed matrix material and conditions for Regime 3 are:

$$v_m = 8l^3 - 16\,(v_{R1} + v_{R2} + v_{R3} + v_{R4} + v_{R5})\ ;\ r/\sqrt{3} \le l \le r/\sqrt{2} \tag{2.3}$$

where $v_{R1} - v_{R5}$ are the volumes of Regions 1-5 described above.

2.2.4 Regime Four: Matrix Displaced Entirely by Interphase

When the nanofiller loading, or interphase thickness to nanoparticle ratio, is relatively high, the interphase extends completely outside the borders of the unit cell, and is indicative of the fourth and final regime, as shown in Figure 2.4. Within the unit cell, only two phases now exist: the nanofiller and the interphase. From this simplified case, the calculation for the unperturbed matrix is trivial. This calculation, as well as the nanoparticle and interphase conditions for Regime Four, is:

$$v_m = 0 \ ; \ r_p \leq l \leq r/\sqrt{3} \tag{2.4}$$

With the unperturbed matrix volume calculated for all possible scenarios of nanofiller loading, nanofiller radius, and interphase thickness, the volume of the interphase within the unit cell can be calculated by simply taking the total volume of the unit cell, and subtracting the volume of unperturbed matrix material, and the volume of the nanoparticle. Then, the volume fraction of each phase within the unit cell is simply the volume of each phase contained within the unit cell, divided by the total volume of the unit cell, as shown below,

$$\phi_p = v_p/8l^3 \ ; \ \phi_i = v_i/8l^3 \ ; \ \phi_m = v_m/8l^3 \tag{2.5}$$

where $\phi_p + \phi_i + \phi_m = 1$. Plots of the interphase and unperturbed matrix volume fractions with respect to particle volume fraction for a 60 nm radius particle are shown in Figures **??** and **??**, respectively, for select interphase thicknesses.

From the shape of the curves in Figures 2.5 and 2.6, a range of nanoparticle loading can be associated with each of the four geometrical regimes. The black curve in both figures can be divided into four different segments. First is a linear segment that is representative of the first regime, and ranges from 0 vol% to low volume fractions. This represents the linear increase of the interphase as particle volume fraction increases. After the linear segment, at slightly higher volume fractions, is a curved segment representative of the second regime that ends at the peak (valley) of the curve. This represents the onset of interphase overlap, and the rate of increase in interphase volume within the unit cell is not as large. The end of this regime corresponds

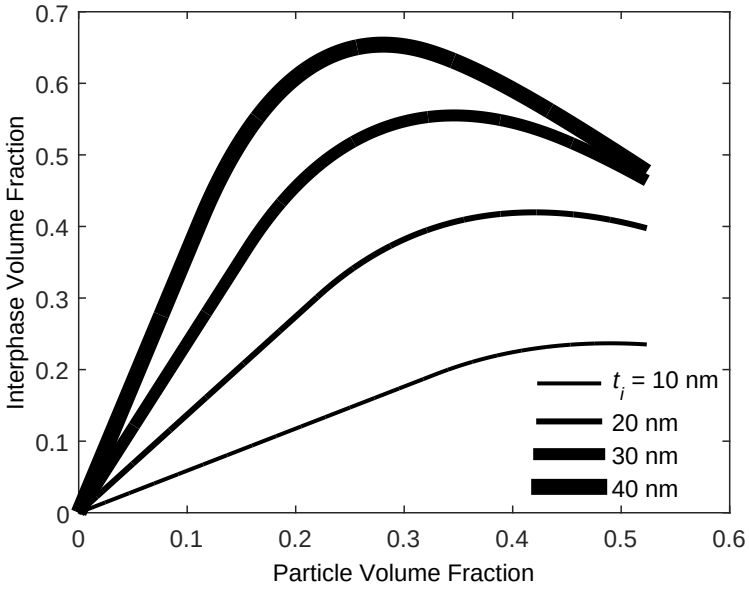

Figure 2.5: (top) The interphase volume fraction with respect to nanofiller loading for various interphase thicknesses surrounding a 60 nm radius, spherical nanoparticle.

to the limit $l = r/\sqrt{2}$, where the interphase boundary extends exactly to the unit cell edge. The second section of the curved segment is representative of the third regime, where the same section of interphase within the unit cell starts to decrease, due to the increase in particle volume fraction. Finally, the last linear segment (negative slope in Figure 2.5) represents the fourth regime, where the unit cell is a two-phase system, comprised of interphase and nanofiller, and the interphase decreases linearly, following the line $y = 1\phi_p$.

2.2.5 Three-Phase Wiener Bounds

The calculated volume fractions for each of the three phases may then be utilized in a three-phase Wiener bound equation to calculate the composite effective permittivity. The Wiener bounds represent the upper and lower limits, respectively, of the effective permittivity of a composite with two or more components, each with their own relative permittivity. Based on the equivalent capacitance for a set of capacitors connected in parallel and in series, the upper and lower Wiener bounds are, respectively,

$$\epsilon_c = \phi_p\epsilon_p + \phi_i\epsilon_i + (1 - \phi_p - \phi_i)\,\epsilon_m \tag{2.6}$$

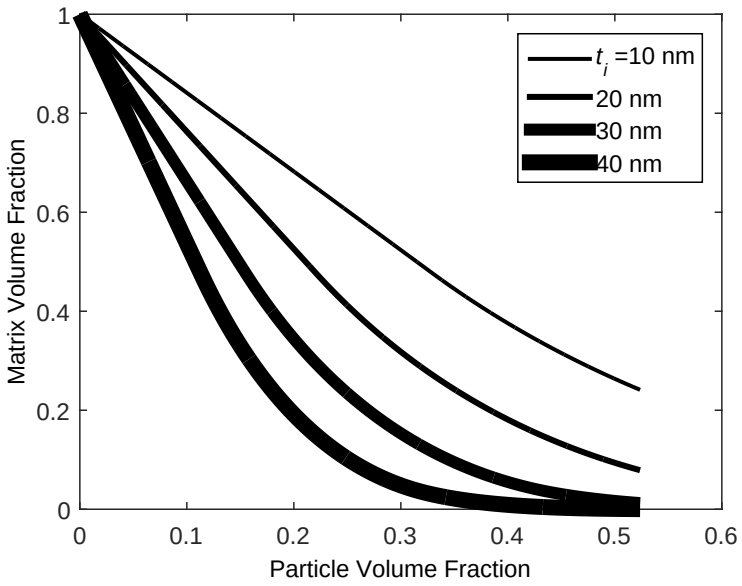

Figure 2.6: The unperturbed matrix volume (corresponding to the interphase volume fraction in Figure 2.5) with respect to nanofiller loading for various interphase thicknesses surrounding a 60 nm radius, spherical nanoparticle.

$$\frac{1}{\epsilon_c} = \left[\frac{\phi_i}{\epsilon_i} + \frac{\phi_p}{\epsilon_p} + \frac{(1-\phi_i-\phi_p)}{\epsilon_m}\right]^{-1} \tag{2.7}$$

where ϵ_c is the effective composite permittivity, and ϵ_p; ϵ_i, and ϵ_m are the relative permittivities of the nanoparticle, interphase, and unperturbed matrix material, respectively.

2.3 Experiment

Silicon nanoparticles (average particle diameter ∼130 nm) were purchased from Nanostructured and Amorphous Materials, Inc; USA. Before composite processing, Si nanoparticles were heat treated in air at 500 °C for 2 hours, resulting in the formation of a continuous surface layer of SiO_2 and to avoid moisture absorption in air. The bisphenol E cyanate ester (BECy) monomer (TenCate Advanced Composites, USA) was mixed with an organometallic-based polymerization catalyst supplied by the manufacturer in a ratio of 100:3. Si nanoparticles were also mixed with BECy monomers to prepare a slurry for composite synthesis. In order to achieve a uniform dispersion of nanofillers, the slurry was ultra-sonicated at 1-2 minute intervals employing a sonic dismembrater (Model 100, Fisher Scientific, USA). Further, the mixture was

placed into a planetary mixer (Mazerustar KK50S, KURABO Industries Ltd; Japan) with a simultaneous rotating and de-aerating section for a period of 30 minutes.

The slurry was passed into a 1.1 mm thick steel mold using a 10 mL syringe and was cured in a rotational oven. Disk-shaped samples (diameter 22 mm) containing 10 and 26 vol% of Si nanoparticles were obtained after the curing process and were polished for subsequent dielectric testing. Fracture surfaces of composite samples were examined by scanning electron microscopy (SEM) (Quanta FEG 250, FEI, USA) to assess the particle dispersion in the polymer matrix. Figure 3 shows the SEM images of the fracture surface of composites with 10 and 26 vol% of Si nanoparticles. It is observed that the nanofillers distribute uniformly in the matrix with little particle agglomeration in the composite with 10 vol% Si loading, shown in Figure 2.7a. Figure 2.7b reveals that the dispersion of Si particles at 26 vol% is more variable, with mild agglomeration in some regions. Dielectric properties of the nanocomposites and neat BECy were characterized with a Novocontrol dielectric spectrometer (Novocontrol Technologies, Germany) in a frequency range from 0.01 Hz to 1 MHz at 20 °C.

2.4 Data Analysis

Permittivity data from polymer-based nanocomposites can be analyzed using the volume fraction model and Wiener bounds described in Section 2, along with surface plotting techniques, to extract reasonable values for the interphase thickness and permittivity for a particular nanocomposite system. To proceed, measured relative permittivity values for a nanocomposite at two or more particle volume fractions are needed, as well as the neat matrix and bulk particle permittivity values. With an average particle size, the volume fraction calculations can be performed.

Rather than assigning a particular value to the interphase a range of thicknesses will be used in the calculations, giving a range of volume fraction ratios amongst the three phases. Similarly, rather than assigning a particular value of relative permittivity to the interphase for use in the Wiener bounds, a range of permittivities is utilized. The example surface plot in Figure 2.8 shows the variation in an effective composite permittivity bound, due to different pairs of interphase thickness and permittivity, for a particular particle volume fraction. The

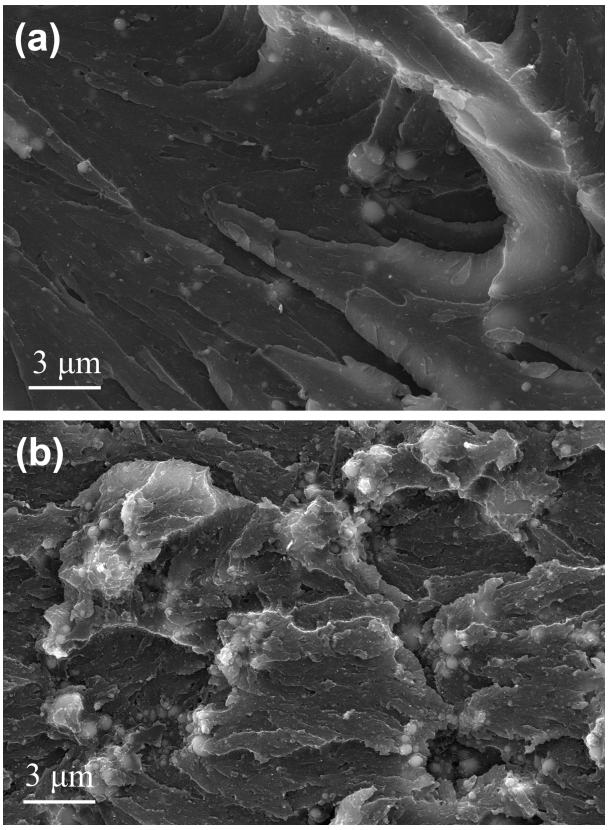

Figure 2.7: SEM images of the fracture surface of composites with (a) 10 and (b) 26 vol% of Si nanoparticles.

interphase ranges from 0 nm (no interphase) to 70 nm (extremely large interphase) while the relative interphase permittivity ranges from 1 (air) to ϵ_p.

Looking at the upper Wiener bound in Figure 2.8, a few characteristics are worth mentioning. When there is no interphase present (0 nm), the three-phase bound is reduced to a two-phase bound, consisting only of matrix and nanofiller, and the composite permittivity remains constant, as indicated by the horizontal edge along the right-hand axis. Similarly, when the relative interphase permittivity is equal to that of the nanofiller, the upper Wiener bound is again reduced from three-phase to two-phase bounds, and the permittivity increases non-linearly with increased interphase thickness, as shown by the edge along the back of the figure. Finally, if the interphase thickness and/or particle volume fraction is high enough, the fourth Regime will be encountered and the system will turn into a two phase system, this time made of interphase and nanofiller. This is exhibited by the close-to-linear edge in Figure 2.8, where the interphase thickness is at 70 nm.

With the upper Wiener bound plotted for a particular volume fraction, the measured effective composite permittivity value can now be added to the plot to compare with the bounds. Represented by the black plane, the measured permittivity value is also shown in Figure 2.8. Any point of intersection between the upper Wiener bound and the measured permittivity plane represents a pair of values for the interphase thickness and permittivity that, when substituted into the volume fraction and three-phase Wiener bound calculations, result in the value of the permittivity measured. The intersections for the same system can be calculated in the same manner for the lower Wiener bound as well, creating a set of interphase intersection arcs for one volume fraction.

Overlaying two sets of intersection arcs, one for each of two volume fractions, may provide an area of overlap, as indicated by the surface spanned by arrows in Figure 2.9. Any point within this overlapped area now represents a pair of interphase thickness and permittivity values that satisfy the Wiener bound and volume fraction calculations for both particle volume fractions and corresponding measured permittivity values. Also, this common area of intersection points provides a range of interphase thickness and permittivity values, which represents a more reasonable approach than a single value for each parameter since the ideal assumptions imposed

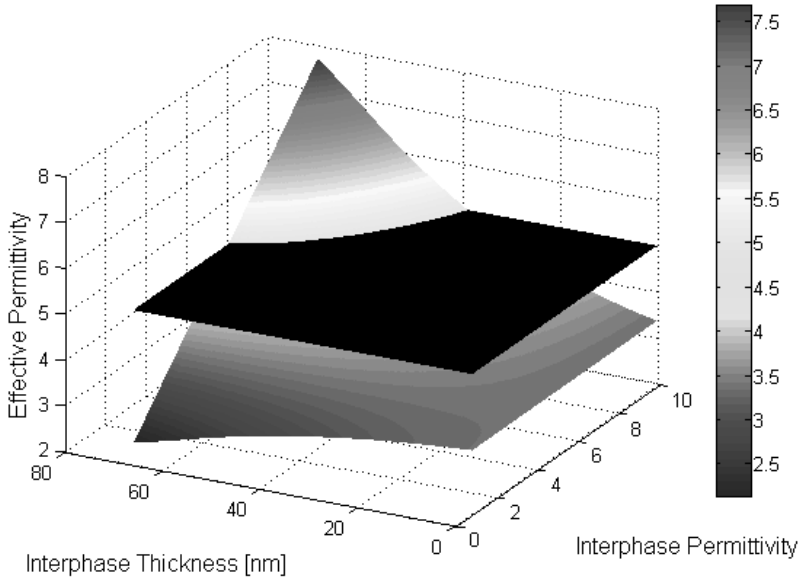

Figure 2.8: Upper Wiener bound showing the variation in effective permittivity of a nanocomposite as a function of both relative interphase permittivity (ϵ_i = 1-10) and thickness (t_i = 0-70 nm) with intersecting measured permittivity plane (at ϵ = 5) at 5 vol% nanofiller. The intersection of the Wiener bound with the plane gives rise to a locus of viable values of ϵ_i and t_i for the interphase. Particle radius = 50 nm; particle permittivity = 10; matrix permittivity = 3.

on the volume fraction calculations do not correspond to the non-ideal conditions present in actual composite processing. An example analysis using two sets of measured permittivity values, one experimental [19] and one literature-based [18], is provided below.

2.4.1 Experimental Analysis

Modeled results of the silicion/bisphenol E cyanate ester system described in Section 3 can be seen in Figure 2.9, where the intersection between the bounds and the permittivity values measured, at two volume fractions, are superimposed upon one another for 1 MHz data. Particle radius 65 nm [1] and relative permittivity 12 [60] were used in the calculations. The matrix relative permittivity was taken as 3.05 at 1 MHz. The area highlighted by arrows indicates pairs of permitted values for interphase thickness, ti, and permittivity, i, that are common to both volume fractions. In Table 2.1, ranges of acceptable interphase thickness values are listed for various allowable permittivity values, for low (0.01 Hz), medium (113 Hz) and high (1 MHz)

frequency. It can be seen that the allowable interphase permittivity shifts to lower values with increasing frequency, as does that of the BECy matrix [1].

Permittivity data of a low-density polyethylene-alumina (LDPE-Al_2O_3) nanocomposite published by Ciuprina et al [2] exhibits the anomalous permittivity minimum described earlier.

The results from the measurements at 1 kHz were chosen for this analysis, to avoid the effects of charge carriers that might appear in the lower-frequency data. Particle radius 20 nm [2] and relative permittivity 9 [60] were used in the calculations. The matrix relative permittivity was taken as 2.195 at 1 kHz. The results of the analysis can be found in Table 2.2 below.

Based on discussions in [46] on the dimensions of the interphase, all results in which the interphase thickness was calculated to be greater than 30 nm were dismissed from the analysis. All of the results in Tables 2.1 and 2.2 were not influenced by this dismissal.

In Figures 2.10 and 2.11, a single pair of interphase thickness and permittivity values (t_i = 30 nm, ϵ_i = 7; t_i = 15 nm, ϵ_i = 1.6, respectively) were chosen from the results of the analysis and substituted into the volume fraction and three-phase Wiener bound calculations, and subsequently compared to their respective data sets. Similarly, two-phase volume fraction and two-phase Wiener bound calculations were also calculated, using the same values used in the above analysis.

2.5 Discussion and Conclusions

It can be seen that the data points of two different data sets, one for a thermosetting matrix and one for a thermoplastic matrix, lie within the range of the three-phase Wiener bounds, calculated utilizing reasonable interphase parameters assigned by the procedure described above, while lying outside of the two-phase Wiener bounds. Comparison of the results in Table 1 with results calculated using a previously described model show good agreement. Reference [52] describes interphases with thicknesses around 30 nm (summing all layers for a 25 nm radius particle), which agree with the present results for the BECy/silicon data. Also, Pitsas model assumes an interphase permittivity ranging between the matrix and nanofiller values, decreasing from the latter exponentially as a function of distance. The present work, while assuming

Table 2.1: Example Pairs of Interphase Parameters for which Experimental Data [1] Falls Within Modeled Three-Phase Wiener Bounds.

Frequency	ϵ_i	t_i
0.01 Hz	8	34 - 42
	9	28 - 40
	10	24 - 38
	11	21 - 37
113 Hz	7	35 - 41
	8	28 - 39
	9	22 - 37
	10	20 - 37
	11	18 - 35
1 MHz	6	32 - 40
	7	23 - 37
	8	19 - 33
	9	17 - 32
	10	15 - 31

Table 2.2: Example Pairs of Interphase Parameters for which Literature Data [2] Falls Within Modeled Three-Phase Wiener Bounds.

ϵ_i	1.2	1.4	1.6	1.8
t_i [nm]	5 - 13	10 - 17	12 - 18	15 - 22

a uniform value for the interphase, also predicts a permittivity value residing between that of the two composite constituents, for the BECy/silicon data, that decreases as the interphase thickness increases.

Comparisons of the results in Table 2 with results using the model found in [52], for LDPE/alumina data that exhibit the anomalous minimum, do not agree, however. While the interphase thicknesses are comparable, depending on the value of interphase permittivity chosen from Table 2, the interphase permittivity values are not. This is due to the anomaly of the minimum permittivity, and the fact that the model in [52] does not account for an interphase permittivity less than that of the matrix, unless a rather large attenuation coefficient is assumed. While the choice of an interphase with permittivity less than that of the matrix results in a better fit to the data, however, a permittivity gradient like that described in [52] is more likely to be realistic.

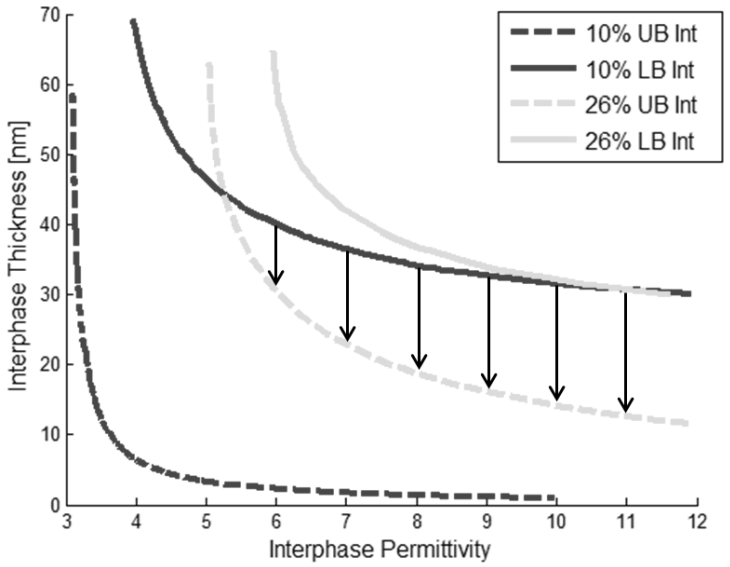

Figure 2.9: Lines of inetersection between calculated three-phase Wiener bounds and measured permittivity values, for two volume fractions of silicon/BECy nanocomposites at 1 MHz. The area highlighted by arrows indicate possible pairs of values for interphase thickness, t_i, and permittivity, ϵ_i, that are common to both volume fractions.

As previously mentioned, the simple nature of the model allows for a range of interphase parameters to be calculated, an approach that more closely resembles the differences between individual particles within a real composite.

However, certain assumptions that insure the simplicity of the model do not simulate realistic conditions. For instance, the constraint that all nanoparticles be fixed on the nodes of a simple-cubic lattice assumes that perfect particle dispersion, free of agglomerations, has taken place, a scenario that often does not occur in real composites. Further, the model constrains the particles, and interphases, to all be uniform in size, respectively, which is also a rare occurrence in practice.

Through the use of randomization techniques, as well as analyzing different microstructures, as opposed to solely spherical particles centered only on a simple-cubic lattice, the authors believe these issues can be dealt with. Starting with the proposed model, the simple-cubic lattice, and respective unit cell, could again be used, except with the constraint that the particle be centered in the unit cell lifted. With the addition of randomly orienting each particle within their respective unit cells, scenarios that more closely resemble actual dispersions can

be simulated. However, lifting these constraints also decreases the ease with which the volume fractions can be calculated analytically, assuming the three-dimensional nature is kept intact. Another randomization technique can also be used to more accurately simulate dispersions encountered in practice, by eliminating another constraint from the proposed model: the fixed particle radius. Using a range of particle radii that reflect distributions found in practice would allow for more realistic permittivity calculations. Again, this makes analytical calculations more complex, though.

Numerical calculations can, however, be utilized in these analytically complex situations. Previous work by Spanoudaki et al [61] has shown that a randomly generated particle distribution can be utilized in the Maxwell-Garnett mixing model to accurately calculate the permittivity of a composite with spherical inclusions. Also, Brosseau et al [62] analyzed changes in the effective permittivity due to spherical, rodlike, and ellipsoidal inclusions, as well as their spatial orientation within a unit cell. However, both of these works do not include an interphase layer. The addition of such a layer in both of these numerical analyses could further improve the accuracy of the calculations, as well as provide values for the interphase parameters.

2.6 Acknowledgements

The authors thank Alun Vaughan for his idea for the work, John Bowler for his assistance with volume fraction calculations, and Andrew D. White, Perry E. Antonelli, and Tim E. Cullinan for their help with the analytical solutions. Further information on the formation and calculation of the five regions in Regime Three can be found at http://crowsandcats.blogspot.com/2013/04/cube-sphere-intersection-volume.html. This work was funded by NASA Cooperative Agreement No. NNX09AP70A.

2.7 APPENDIX: CALCULATION OF REGIME 3

As described in Section 2.2, the calculation of the unperturbed matrix volume fraction is simplified by first dividing the interphase boundary into sixteen identical pieces. Next, each of the sixteenths can be divided into five different regions such that the volume of unperturbed

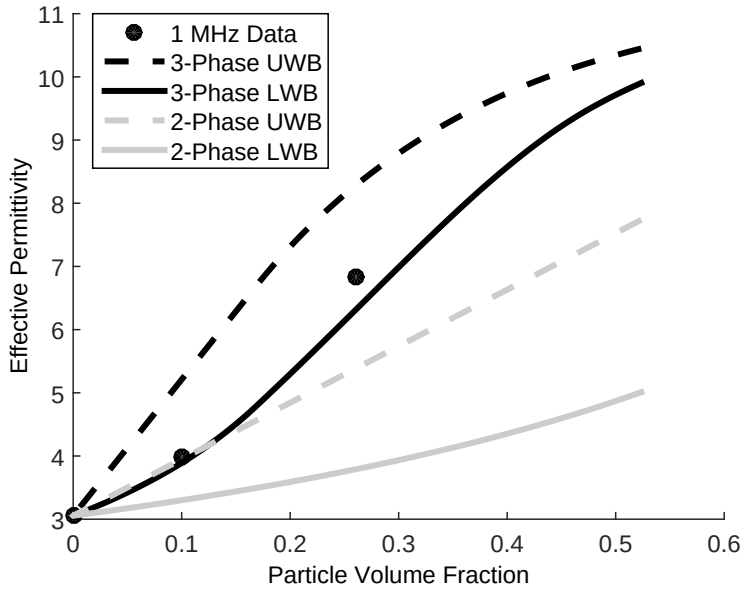

Figure 2.10: Three-phase and two-phase upper and lower Wiener bounds (UWB and LWB) for 1 MHz permittivity data measured on a silicon/bisphenol E cyanate ester nanocomposite [8]. In the calculation the nanoparticle radius = 65 nm and relative permittivity = 12, while the interphase thickness = 30 nm and relative permittivity = 7.

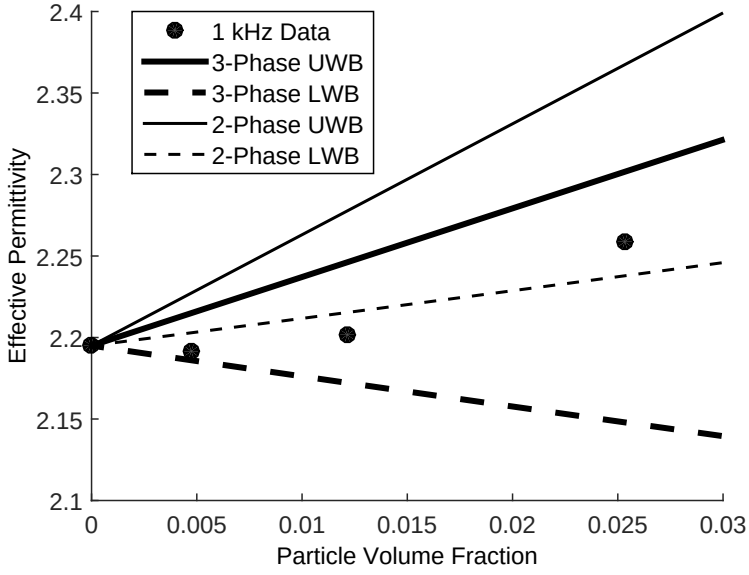

Figure 2.11: Three-phase (thick curves) and two-phase (thin-curves) upper and lower Wiener bounds for 1 kHz permittivity data measured on a LDPE/Al2O3 system [9]. In the calculation the nanoparticle radius = 20 nm and relative permittivity = 9, while the interphase thickness = 15 nm and relative permittivity = 1.6.

matrix material in the third regime, in which the interphase overlap occurs through cell faces and edges, is expressed in equation (3). The equations for the volume of each of the five regions are listed below, where $c = (l/r)^2$. The limit θ_i is also displayed below.

$$v_{R1} = \frac{l^2\sqrt{r^2 - 2l^2}}{3} \tag{2.8}$$

$$v_{R2} = \frac{l^2\sqrt{r^2 - 2l^2}}{6} \tag{2.9}$$

$$v_{R3} = \frac{l^2 r}{3}\left[\frac{(1-c)\tan^{-1}\left[\frac{\sqrt{2c}\sin\theta}{\sqrt{1-2c+\cos(2\theta)}}\right]}{2\sqrt{c}} + \frac{\sqrt{1-2c+\cos(2\theta)}\sec\theta\tan\theta}{2\sqrt{2}}\right]_{\theta_i}^{\pi/4} \tag{2.10}$$

$$v_{R4} = \frac{l^3}{6}\left(\frac{r^2}{l^2} - 1\right)\left(\frac{\pi}{4} - \theta_i\right) \tag{2.11}$$

$$v_{R5} = \frac{r^3}{3}\left[\frac{l}{r}\left(\frac{\pi}{4} - \theta_i\right) - \left(-\sqrt{c}\tan^{-1}\left[\frac{\sqrt{2c}\sin(\theta)}{\sqrt{1-2c+\cos(2\theta)}}\right]\right.\right. \tag{2.12}$$

$$\left.\left. + \frac{\sqrt{1-c}\sin^{-1}\left[\frac{\sin(\theta)}{\sqrt{1-c}}\right]\sqrt{-\frac{1-2c+\cos(2\theta)}{c-1}}}{\sqrt{1-2c+\cos(2\theta)}}\right)\right]_{\theta_i}^{\pi/4} \tag{2.13}$$

Where

$$\theta_i = \cos^{-1}\left(\frac{d}{\sqrt{\rho^2 - d^2}}\right) \tag{2.14}$$

CHAPTER 3. THERMO-OXIDATIVE DEGRADATION ASSESSMENT IN QUASI-ISOTROPIC CARBON FIBER/EPOXY COMPOSITES

Thermo-oxidative Degradation Assessment in Quasi-isotropic Carbon Fiber/Epoxy Composites

C. Daily, D.J. Barnard, R.W. Jones, J.F. McClelland, N. Bowler

Materials Science and Engineering, Iowa State University, Ames IA 50011, USA

Published in *41st Annual Review of Progress in Quantitative Nondestructive Evaluation Proceedings*, 2014.

Abstract

Components made from polymer matrix composites (PMCs) are finding increasing use in armored vehicles for the purpose of weight savings and fuel efficiency. Often times, these PMC components are installed next to engines, or in other high-temperature environments within the vehicle. The present work investigates the change in surface chemistry and its correlation with changes in the interlaminar shear strength (ILSS) due to accelerated thermo-oxidative aging of a quasi-isotropic carbon fiber reinforced epoxy laminate. Samples are aged isothermally at various temperatures whose selection is guided by degradation steps revealed by thermo-gravimetric analysis. Fourier transform infrared (FTIR) photoacoustic spectroscopy is utilized to identify the chemical changes due to aging, and compression-test results reveal a non-linear decrease in ILSS with increasing aging temperature. A correlation between the FTIR and ILSS data sets suggests that nondestructive FTIR techniques may be used for assessing ILSS of PMCs.

3.1 Introduction

Polymer matrix composites (PMCs) are widely used for their high strength-to-weight ratios compared to their metallic counterparts. As the composite field has matured, the ever-increasing benefits of these materials can be measured by their increased use in aircraft. The Boeing 787 is made up of nearly 50 percent carbon-fiber reinforced PMCs, more than previous Boeing aircrafts which opted for more aluminum-based designs [17].

PMCs are also proving to be cost-efficient in terms of maintenance and operation. For example, the Boeing 777 has a PMC tail, while the 767 has 25 percent smaller, aluminum tail. However, despite the size difference, the 767 tail requires 35 percent more labor hours than the 777 [17]. This decreased labor time for the 777 is due to the higher corrosion resistance of PMCs. In addition, PMC-majority designs such as the Boeing 737 MAX lead to lighter overall aircrafts [63]. These lighter structures, along with new aerodynamic designs and engine improvements, are helping reduce fuel costs during operation [63].

Assessing damage in laminated PMCs has long been a focus of nondestructive evaluation (NDE). A variety of defects can be detected using NDE techniques including delaminations, matrix-rich or poor regions, and matrix cracking. Now a mature field, there are currently numerous guides encompassing these NDE techniques [64, 65]. Many have been used to detect damage in aged carbon-fiber/epoxy composites, such as ultrasonics [37], Terahertz ultrasonics [66], and Fourier-transform infrared spectroscopy (FTIR) [67], among others. However, while degradation solely of the matrix may lead to detectable delaminations or cracks, there is still a chance of composite failure when these defects are not detected in an aged matrix.

The present work aims to establish indicators of reduced serviceability of PMCs due to thermo-oxidative matrix degradation. An untoughened epoxy/carbon fiber-reinforced laminate was pressed, cured, and cut into samples. Degradation took place after cutting via accelerated isothermal aging based on thermogravimetric analysis results. Chemical changes in the composite were analyzed with photoacoustic spectroscopy, which measures IR absorptions. Degradation kinetics were modeled via two iso-conversional model-free methods, the Friedman model and the Ozawa-Flynn-Wall model, and the activation energies for the fractional degra-

dation were determined. Additionally, the interlaminar shear strength of aged composites was determined via the double-notch compression test. Finally, the work proposes a coupling between the characterization of the degradation states and the weakened mechanical properties of the composites.

3.2 Experiment

3.2.1 Materials

Square-foot laminae were cut from untoughened unidirectional carbon-fiber epoxy tape supplied by Renegade Materials (RM-2002). The reinforcment is HexTow IM7 carbon fibers [68]. A 24-ply quasi-isotropic lay-up was utilized, $[0, +45, -45, 90]_s$, and the lay-up was cured and pressed using a Wabash Genesis series hydraulic press at 350 °C under 85 psi and vacum. The cured laminate was scanned for defects using air-coupled, back-wall ultrasonic testing (UT), and uniform sections were cut into nominally 12.7 mm strips using an IMER Combi 1000 saw for compression tests, in accordance with ASTM D3846-08 [32]. The 12.7 mm strips were then cut into 79.5 mm, nominally, long samples using a 0.635 mm thick Dremel diamond wheel.

Following ASTM D3846-08 [32], one notch was cut 36.3 mm from the end of the samples, on both sides and opposite ends, so that the notches had a separation of $\sim$ 6.4 mm. The notches were cut to half the thickness of the samples. Once all cuts were made to the samples, they were placed in a furnace at 120 °C to dry for two hours with one surface not exposed, and another two hours with the opposing surface unexposed, for a total of four hours drying. After drying, the samples were immediately placed into a desiccator until needed.

3.2.2 Thermogravimetric Analysis

In order to determine an appropriate range of aging temperatures, thermogravimetric analysis (TG) was first performed. TG measures the instantaneous mass of a small sample ($\sim$5-20 mg) subjected to elevated temperatures which volatilize the sample. Thermograms are produced, which record the weight percent of the sample as a function of temperature. From

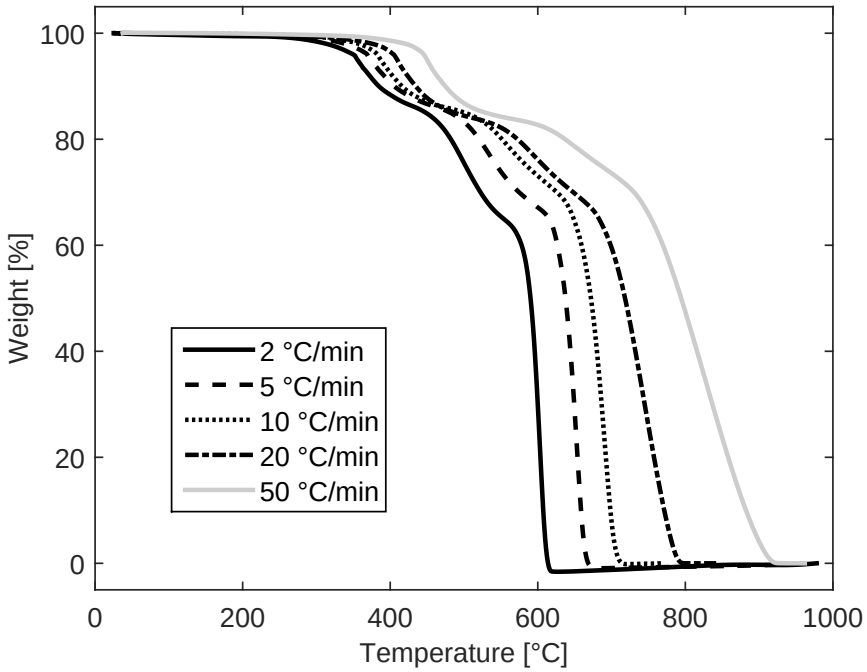

Figure 3.1: Thermograms of untoughened epoxy/carbon fiber composites.

thermograms, and their derivative, various degradation mechanisms are revealed. In addition, subjecting the samples to a variety of heating rates can allow for the analysis and extraction of certain kinetic parameters.

TG was performed on a set of undried samples cut into small cubes or platelets, with weights between 5-15 mg. A Q50 TGA from TA Instruments was used, and samples were placed in a platinum pan. The sample was purged with air at a flow rate of 60 mL/min, while the balance was purged with nitrogen at a rate of 40 mL/min. The samples were exposed to five different heating rates, and ran from room temperature to between 800 and 950 °C, the instrument upper limit. The thermograms and temperature derivatives for untoughened epoxy/carbon fiber samples are shown in Figures 3.1 and 3.2. The thermograms, and more clearly the thermogram derivatives, indicate that there are three primary degradation steps.

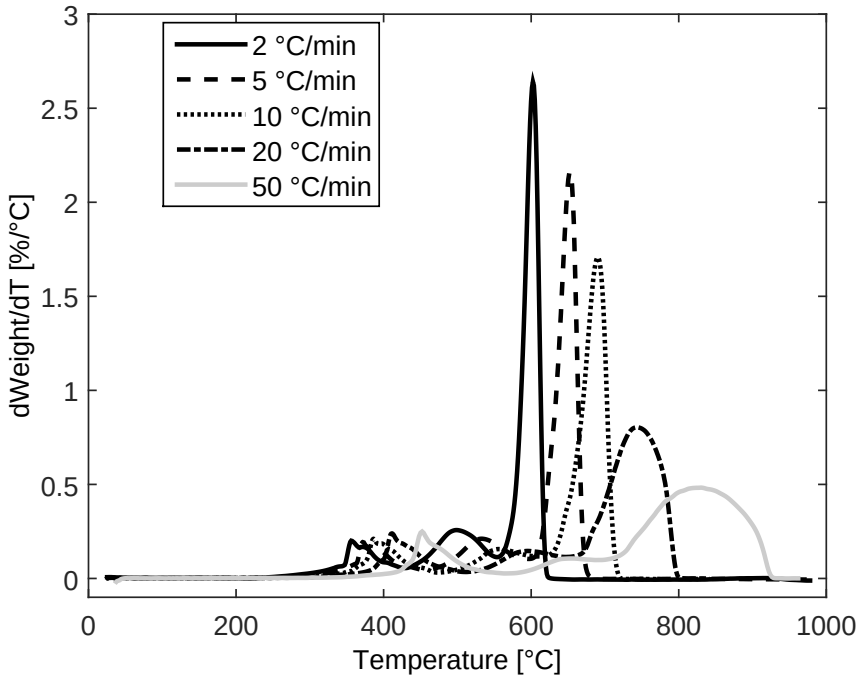

Figure 3.2: Temperature derivative of the thermogram in Figure 3.1.

3.2.3 Accelerated Isothermal Aging

As toughened epoxy (also supplied by Renegade, RM-2005) is rated to 300 °F (∼150 °C) [69], the lowest aging temperature was selected to be 150 °C. This will act as a control test. Based on the TG results, the initial degradation mechanism begins roughly between 250 and 300 °C. Therefore, the maximum aging temperature was chosen to be 275 °C. Two more aging temperatures, 200 and 225 °C, were chosen to fill in the gaps between the control and maximum temperatures. This lead to a total of four different aging temperatures: 150, 200, 225, and 275 °C.

Aging was performed in a Barnstead Thermolyne furnace, with the mass of the samples measured immediately before being placed in the furnace. The furnace was allowed to stabilize at the temperature for an hour before placing the samples inside. Similar to the drying procedure, samples were aged for four total hours: two hours with one side exposed, the next two with the same side not exposed.

3.2.4 Interlaminar Shear Strength

The mechanical integrity of the aged materials was analyzed via the interlaminar shear strength. Following the previously described standard [32], the aged samples were secured in a supporting jig to prevent buckling of the compressed fibers. Samples were centered in the jig and evenly flushed on both ends and the along the width. Compression was applied and measured via an Instron 5960 Dual Column Tabletop Universal Testing System at a compression speed of 1.3 mm/min. The maximum load ($\sigma_{\max}$) was recorded (at rupture), along with the pre-measured width between the notches (w) and the failed area (l). Following the standard, the in-plane shear strength is calculated as

$$\tau = \frac{\sigma \max}{wl} \tag{3.1}$$

It has been reported [33] that the procedure detailed in [32] more accurately reports the interlaminar shear strength (ILSS), as opposed to the in-plane shear strength. Although this test also tends to measure lower ILSS values than other tests, due to the high stress concentrations near the notches, relative comparisons are sufficient for the present work. Additionally, to account for the variability caused by the notches, ten samples were tested at each aging temperature, the averages of which will be reported.

3.2.5 Photoacoustic Spectroscopy

To analyze the chemical changes on the surface of the composites, infrared data was obtained using photoacoustic spectroscopy (PAS). PAS can detect chemical changes by exposing a small sample to IR radiation which is intensity modulated. As the sample surface absorbs the radiation, deexcitation occurs as heat dissipated through the sample. Some of the heat then begins to flow from the sample and into the surrounding purge gas, which consequently expands. As the energy dissipates, the gas returns to its neutral state, and the process is repeated. These gas expansions and contractions, oscillating at the modulation frequency, are detected acoustically with microphones in the sample cell, and this data is Fourier transformed to obtain the IR-spectra [70].

For the present work, small square samples (∼5 mm) were cut from both one corner and one side of three aged samples, resulting in six PAS samples per aging condition. The samples were placed into the sample holder on a platform above a small layer of desiccant, and purged with helium gas to remove any moisture from the sample and surrounding air before entering the PAS detector (MTEC Photoacoustic, Inc. Model 200). A Digilab FTS 7000 FT-IR spectrometer was used in rapid-scan mode at 2.5 kHz, with a spectral resolution of 8 cm^{-1} and range from 400-4000 cm^{-1}. Each spectrum was the average of 128 scans.

3.2.6 Kinetic Modeling

As previously mentioned, certain kinetic parameters can be extracted from TG data measured for multiple heating rates. A variety of models can be utilized to determine these parameters, although the vast majority, if not all, incorporate the reaction rate equation.

General Reaction Rate The general rate of a reaction is defined as the time derivative of the amount reacted, or α. When calculating the reaction rate from a thermogram, α can be defined as $\alpha = 1 -$ wt%, for each instantaneous weight percent.

$$\frac{\mathrm{d}\alpha}{\mathrm{d}t} = K(T)f(\alpha) \tag{3.2}$$

where $K(T)$ is the rate constant, and $f(\alpha)$ is a function of the reaction mechanism. Often in kinetic analysis, the reaction rate with respect to temperature is desired, rather than time. This is accounted for by multiplication of the constant heating rate:

$$\begin{aligned} \beta\left(\frac{\mathrm{d}\alpha}{\mathrm{d}T}\right) &= K(T)f(\alpha) \\ \beta &= \frac{\mathrm{d}T}{\mathrm{d}t} \end{aligned} \tag{3.3}$$

The rate constant is commonly approximated by the well-known Arrehnius equation:

$$K(T) = Ae^{(-E_a/RT)} \tag{3.4}$$

The following two models induce various modifications to the general reaction rate equation in order to obtain the activation energy.

Friedman Analysis The kinetic analysis first proposed by Friedman [71] was one of the initial model-free, isoconversional methods. This type of methodology assumes no particular mechanism(s) of degradation or reaction, and does not require one. Using this 'model-free'analysis, the Friedman method is able to characterize the activation energies of multiple degradation mechanisms, that may or may not range in complexity. In the case of this research, the Friedman analysis naturally lends itself as a viable tool for retreiving the activation energies.

The basis of the Friedman method involves taking the natural logarithm of each side of the reaction rate equation, Eq. 3.3 with Eq. 4.4 substituted, to produce

$$\ln\left[\beta\frac{\mathrm{d}\alpha}{\mathrm{d}T}\right] = \ln\left(Af(\alpha)\right) - \frac{E_a}{RT} \tag{3.5}$$

which results in a linearization of the rate reaction equation. Plotting the left side of Eq. 4.5 vs. the reciprocal of the absolute temperature is known as a Friedman plot. A Friedman plot of the data from Figure 3.1, created using Thermokinetics (version 3.1) software by Netzsch, is presented in Figure 3.3. In order to determine the activation energy at a particular stage of conversion, particular α values are selected and identified for each heating rate curve. Then, the points are fit linearly, and the slope of these constant fractional mass loss (CFML) lines are equal to $-E_a/RT$, from which the activation energy can be calculated. A plot of the activation energies calculated in this manner, at a variety of CFML values, is shown in Figure 3.4. Knowledge of $f(\alpha)$ can lead to calculation of the frequency factor using the y-intercept.

Ozawa-Flynn-Wall Analysis A second 'model-free' analysis is the Ozawa-Flynn-Wall (OFW) method [72, 73]. Similar to the Friedman method, the OFW method utilizes a modified form of the general reaction rate equation. However, where the Friedman method rearranged and took the natural logarithm of the general reaction rate equation, the OFW method is mathematically more complex. First, the rate equation is rearranged to have all α terms on the same side.

$$\frac{\mathrm{d}\alpha}{f(\alpha)} = \frac{A}{\beta}e^{(-E_a/RT)}\mathrm{d}T \tag{3.6}$$

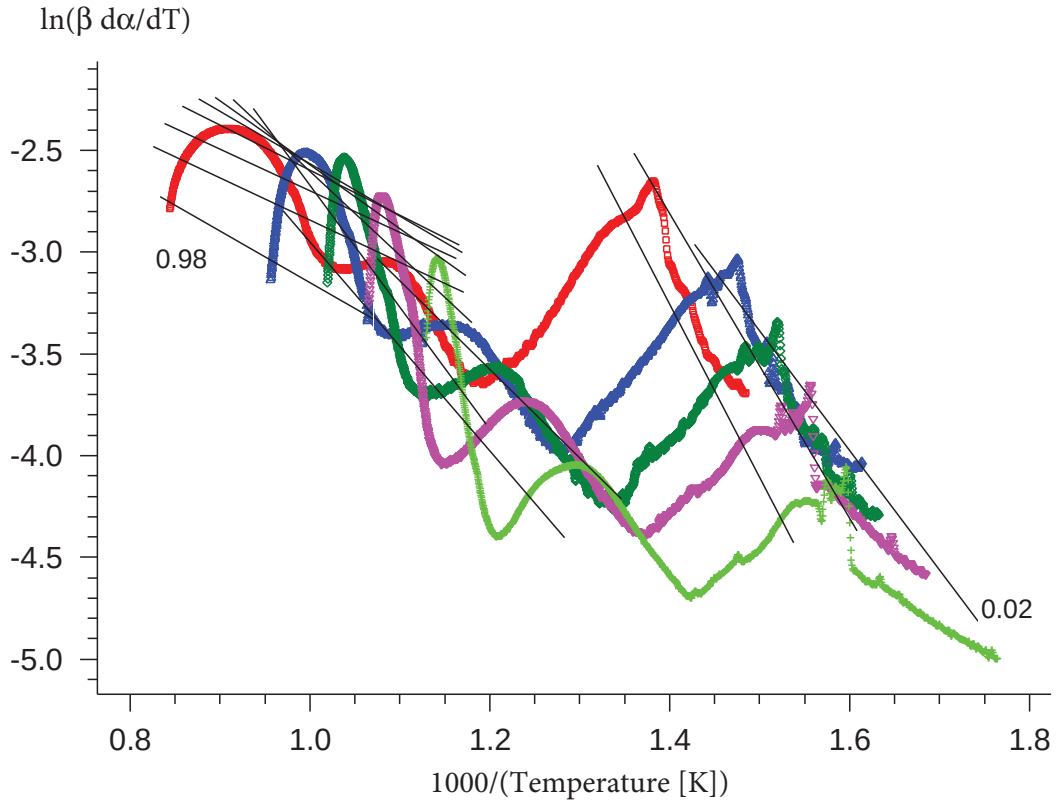

Figure 3.3: Friedman plot of the TG data from Figure 3.1. Constant fractional mass loss (CFML) lines are represented in black for increasing (from right to left) fractional mass. Heating rates are increasing from bottom right (2 °C/min) to top left (50 °C/min).

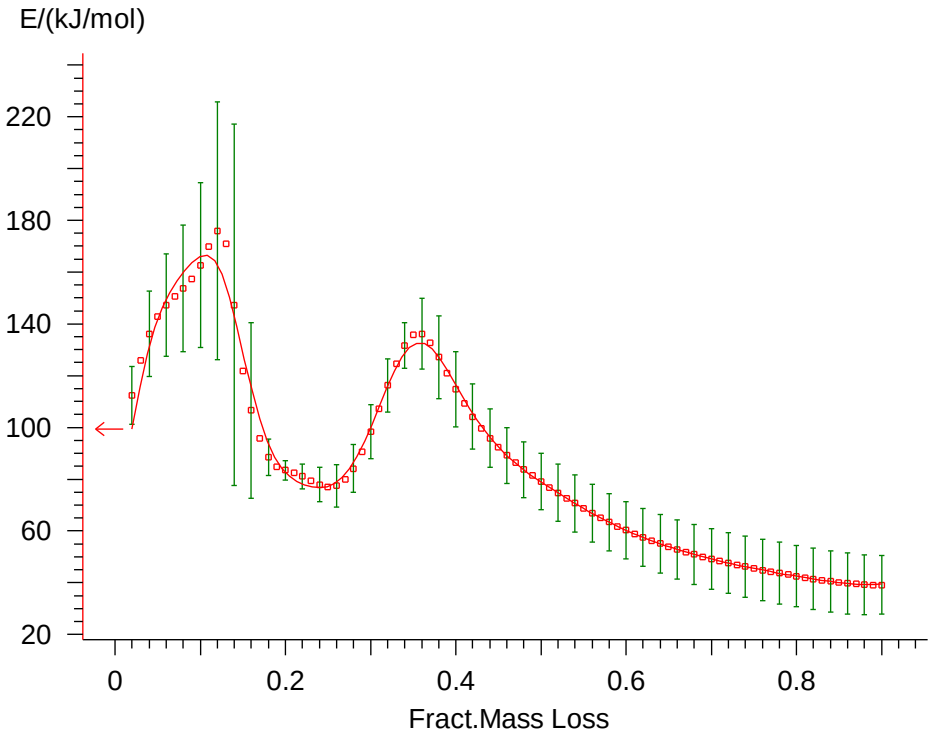

Figure 3.4: Activation energy as a function of fractional mass loss based on the Friedman plot from Figure 3.3.

Then, taking the integral of both sides leads to

$$F(\alpha) = \int_0^{\alpha} \frac{\mathrm{d}\alpha}{f(\alpha)} = \frac{A}{\beta} \int_{T_0}^{T} e^{(-E_a/RT)} \mathrm{d}T \tag{3.7}$$

where $F(\alpha)$ is equal to $\int \mathrm{d}\alpha / f(\alpha)$. Eq. 3.7 can be simplified by substituting x for E_a/RT

$$F(\alpha) = \frac{AE_a}{\beta R} \int_{x_0}^{x} \frac{e^{-x}}{x^2} \mathrm{d}x = \frac{AE_a}{\beta R} p(x)$$

where $p(x)$ equals the integral of $(e^{-x}/x^2)\,\mathrm{d}x$ from x_0 to x. Taking the logarithm of each side

$$\log F(\alpha) = \log\left(\frac{AE_a}{R}\right) - \log\beta + \log p(x) \tag{3.8}$$

Doyle [74, 75] approximated $\log p(x)$ as

$$\log p(x) \cong -2.315 - 0.4567x$$

Substituting into Eq. 4.7 and differentiating at constant α:

$$\frac{\mathrm{d}\,\log\beta}{\mathrm{d}\,(1/T)} \cong -0.4567 \frac{E_a}{R}$$

assuming A, $f(\alpha)$, and E_a are independent of T, and A and E_a and independent of α [73]. Rearranging and integrating leads to

$$\log\beta \cong -0.4567 \frac{E_a}{RT} \tag{3.9}$$

The activation energy can be extracted from a plot of $\log\beta$ vs $1/T$ and, similar to the Friedman method, taking the slope of CFML lines. Using Eq. 4.8, with $R = 8.314$ J/mol K^{-1}, the activation energy is found to be

$$E_a \cong -18.20m \tag{3.10}$$

where m is the slope of the CFML line. An Ozawa-Flynn-Wall plot, with CFML lines, for the untoughened epoxy/carbon fiber system is shown in Fig. 3.5. Similar to Figure 3.4 for the Friedman analysis, the activation energy can be plotted as a function of CFML values, shown in Figure 3.6.

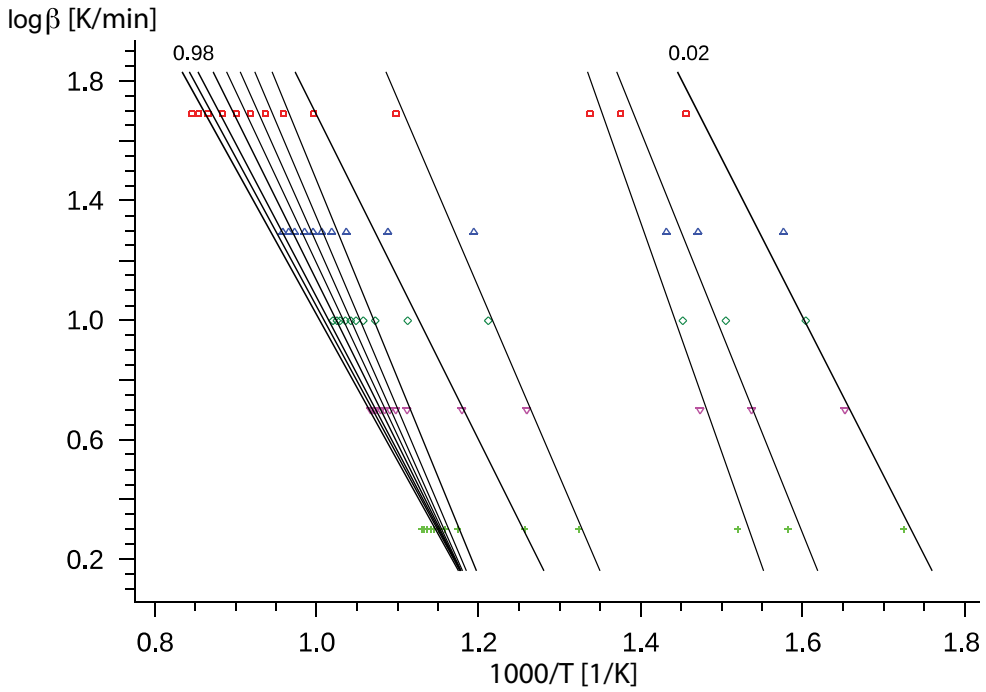

Figure 3.5: Ozawa-Flynn-Wall plot of the TG data from Figure 3.1. Constant fractional mass loss (CFML) lines are represented in black for increasing (from right to left) fractional mass. Heating rates are increasing from bottom (2 °C/min) to top (50 °C/min)

3.3 Results and Discussion

The isothermal aging results are found in Figure 3.7, as a percentage of total resin with the samples. The percentages were calculated from the densities of the resin (1.2 g/cc) and the reinforcing fibers (1.78 g/cc) [68], as well as the percentages of both constituents in the composite (38.56 vol% resin; 30.52 wt% resin), calculated according to ASTM D3171-11: Procedure G [11]. There appears to be an exponential-type increase in the mass lost as the aging temperature increases.

The results of the ILSS measurements are found in Figure 3.8. A slight drop in the ILSS, from ∼42 MPa to ∼35 MPa, is observed from the 150 to 200 and 225 °C samples. Further decreases, down to ∼28 MPa, are seen between the 200 and 225 °C samples and the 275 °C sample.

Photoacoustic spectroscopy results are shown in Figure 3.9. All spectra are normalized to the maximum at 1153 cm^{-1} and minimum at 3958 cm^{-1}. As the aging temperature increases,

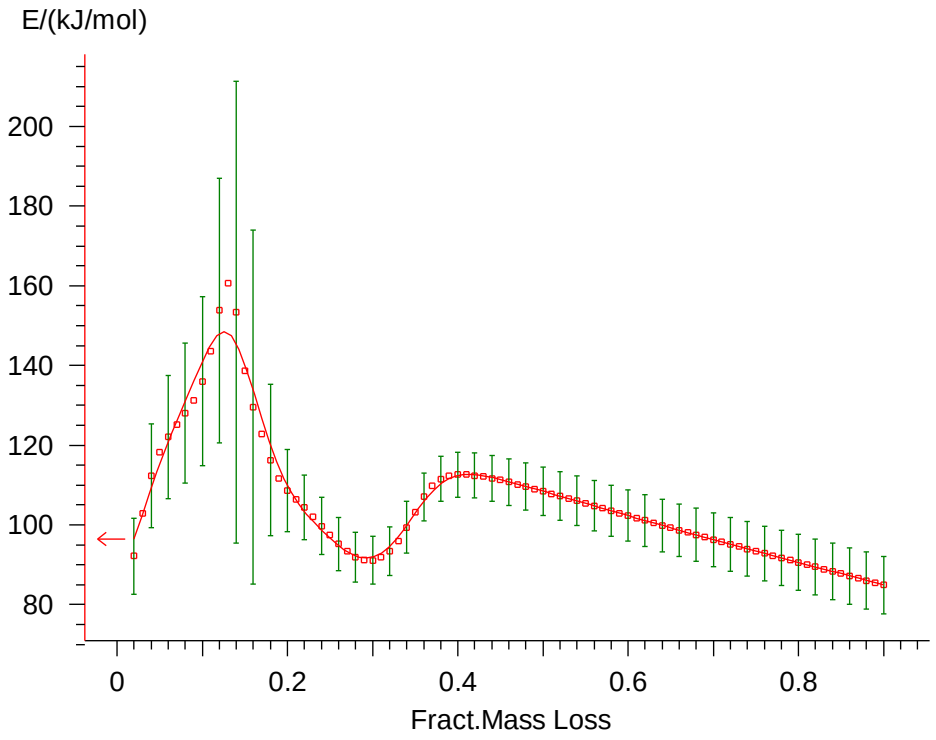

Figure 3.6: Activation energy as a function of fractional mass loss based on the Ozawa-Flynn-Wall plot from Figure 3.5.

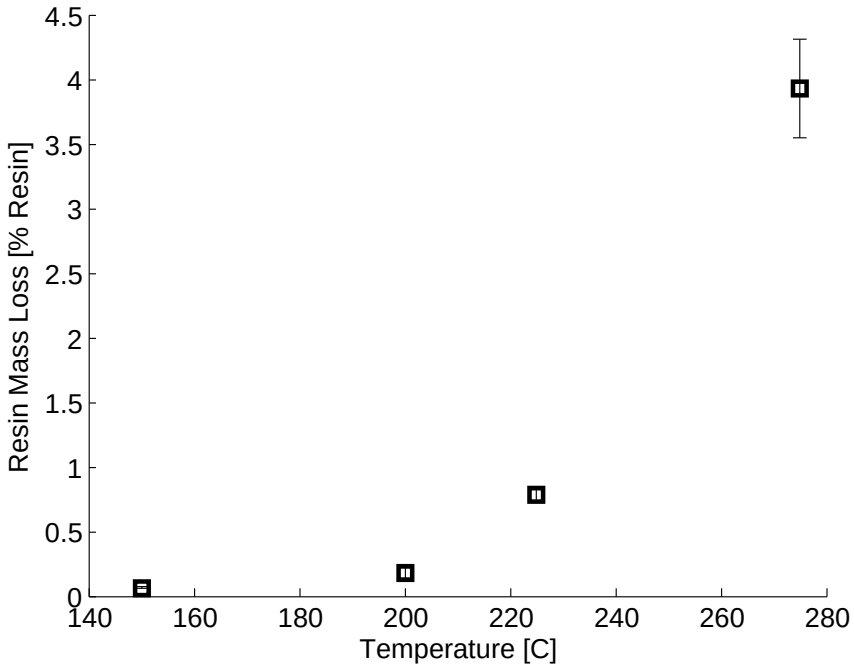

Figure 3.7: Resin mass loss results for the untoughened epoxy/carbon fiber samples. The squares represent the average of 10 measurements and the error bars represent one standard deviation.

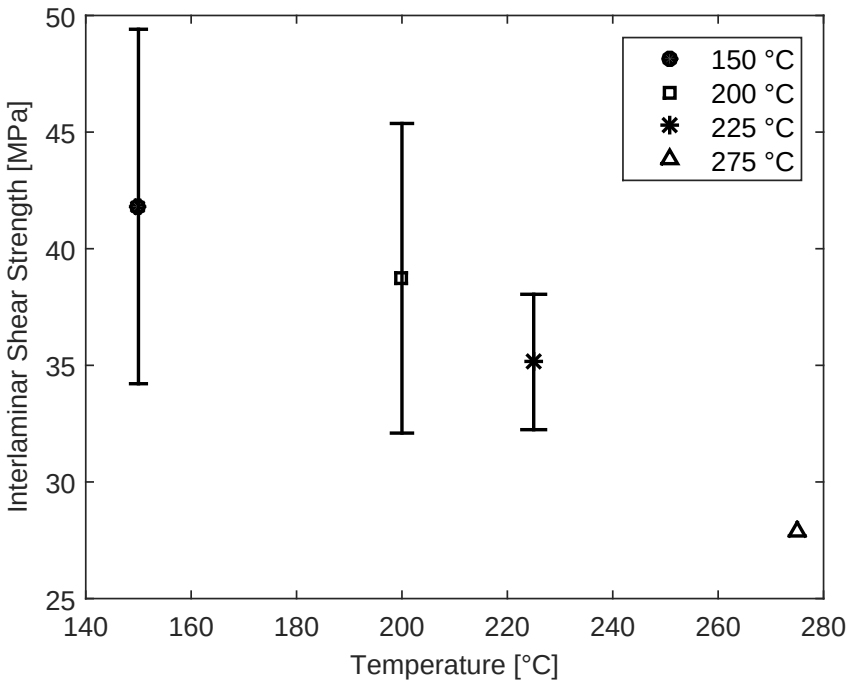

Figure 3.8: ILSS results for the untoughened epoxy/carbon fiber samples. The squares represent the average of 10 measurements (except for 275 °C, which represents one measurement), and the error bars represent one standard deviation.

the spectra reveal certain features at a variety of particular wavenumbers. Around 1682 cm^{-1}, a peak arises, initially, in the 200 °C spectrum, and more strongly in the 225 and 275 °C spectra. This feature is not present in the 150 °C spectrum. The appearance of this peak, representative of a carbonyl functional group, is generally indicative of oxidation.

At higher wavenumbers, further indicators of chemical changes in the matrix are evident. In the 150 °C spectra, a peak is present around 3400 cm^{-1}, with a shoulder around 3480 cm^{-1}. As the aging temperature was increased to 200 °C, both the peak and its shoulder decreased slightly in intensity. Finally, as the aging temperature was increased even further to 225 and 275 °C, the peak intensity decreased even further, and the shoulder disappered completely. Additionally, a peak near 2920 cm^{-1} with a shoulder around 2880 cm^{-1} decreases in intensity as the aging temperature is increased, all but disappearing in the 275 °C spectrum. Conversely, a weak peak near 3070 cm^{-1} becomes stronger as the aging temperature increases.

With these results, a few correlations can be observed between them, and a practical use for the correlations can be seen. Obtaining the IR spectra from a composite aircraft non-

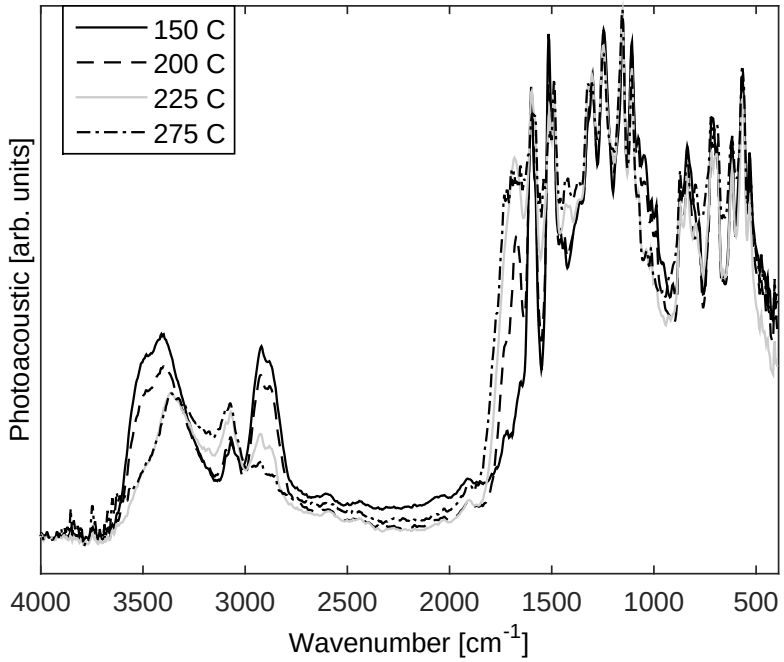

Figure 3.9: IR spectra for untoughened epoxy/carbon fiber composites. All spectra are normalized to the maximum at 1153 cm^{-1} and minimum at 3958 cm^{-1}. Higher temperature aging shows an increase near the 1682 cm^{-1} peak, representative of the introduction of more carbonyl groups due to oxidation.

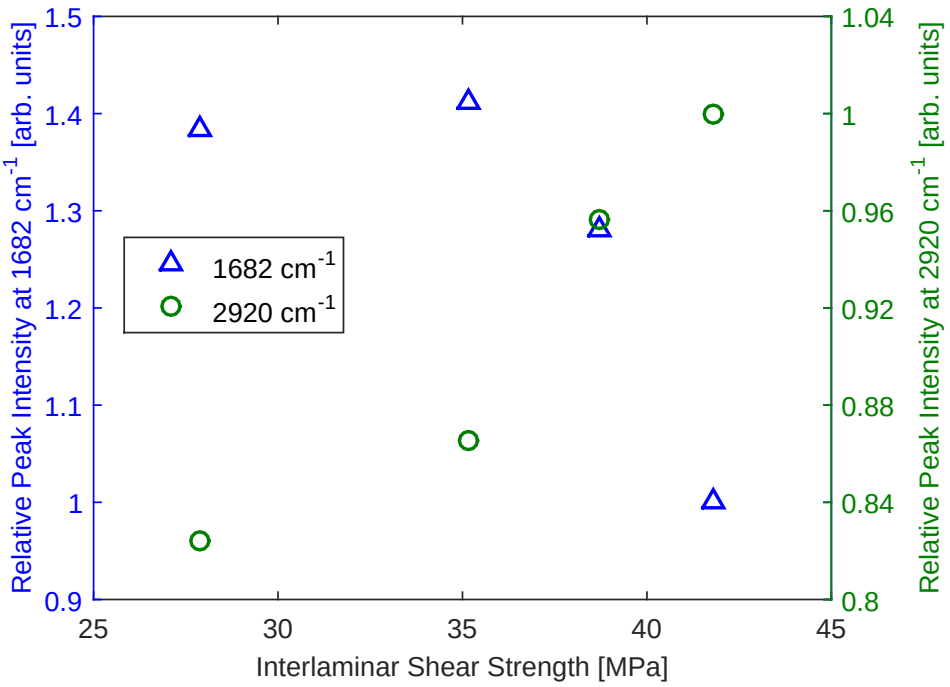

Figure 3.10: ILSS values from Figure 3.8 vs the relative peak intensities for the 1682 cm^{-1} peak (squares) and the 2920 cm^{-1} peak (circles) extracted from Figure 3.9. Error bars for the ILSS data (shown in Figure 3.8) have been omitted for clarity. The peak intensities for the 150 °C spectra were normalized to the value of 1.

destructively is becoming more prominent as advances in IR technology become more readily available [76, 77]. Therefore, the particular chemical changes induced on the surface of an in-use aircraft can be compared to the neat, unaged spectra of the same material, or even the same sample. Based on the difference in intensity between the two measurements, at around 1682 cm^{-1} or at other characteristic wavenumbers, the value can be compared to differences between the photoacoustic spectra of the isothermally aged samples.

After determining the equivalent isothermal aging temperature of the in-use sample, the ILSS of the sample can then be directly estimated. Figure 3.10 shows this relationship for the ILSS values from Figure 3.8 at two different wavenumbers from Figure 3.9: ∼1682 and ∼2920 wavenumbers. Similarly, the amount of mass loss can be estimated, and from this the amount of energy that has already been supplied to the material. All of these material characteristics can be estimated from one IR measurement.

3.4 Conclusion

Untoughened epoxy/carbon-fiber quasi-isotropic composites were isothermally aged to degrade the matrix component. As the aging temperature was increased, the measured ILSS values of the composites decreased, and various chemical changes were detected in IR spectra. In addition, the activation energy was calculated at various points in the composite degradation via two 'model-free' isoconversional methods: the Friedman method, and the Ozawa-Flynn-Wall method. Correlations between the chemical indicators detected by PAS and the mechanical properties measured by ILSS have been described. Future work will involve characterizing a toughened epoxy/carbon-fiber system in the same manner presented here, and differences between the two epoxy systems explored.

3.5 Acknowledgements

The authors would like to thank Hugh Schuster and Sunil Chakrapani for their help with laminate pressing, and Joseph Schaefer for assistance with mechanical testing. This material is based on work supported the Army Research Laboratory as part of cooperative agreement number W911NF0820036 at the Center for Nondestructive Evaluation at Iowa State University.

CHAPTER 4. DIELECTRIC PROPERTIES AND KINETIC STUDY ON THE DEGRADATION OF BISMALEIMIDE RESIN

Connor Daily, Nicola Bowler

Materials Science and Engineering, Iowa State University, Ames IA 50011, USA

Accepted for presentation at PolyChar 23: 23rd World Forum on Advanced Materials, Lincoln, Nebraska, U.S.A. May 11-15, 2015

Abstract

Bismaleimide, a thermosetting resin, is attracting interest in the aerospace industry due to its epoxy-like processability, but better high-temperature performance than epoxy. As this industry shifts towards using higher overall percentages of fiber-reinforced polymer-matrix composites, understanding how these systems degrade, in particular the polymer matrix component, becomes increasingly important. Additionally, these materials are now being exposed to a wider variety of environmental and physical conditions, as new areas of usage, for both primary and secondary roles, are being explored. In this context, the thermo-oxidative degradation kinetics of bismaleimide are explored. Two model-free isoconversional methods, the Friedman and Ozawa-Flynn-Wall methods, are used to analyze results from thermogravimetric analysis at a variety of heating rates (2, 5, 10, 20, and 50 °C/min) from room temperature to 800 °C. From these methods, the activation energies associated with particular degradation mechanisms have been determined. Additionally, the dielectric properties of the bismaleimide resin were measured as a function of frequency (0.10 Hz to 1 MHz) and temperature (-140 °C to 160 °C)

using spectroscopic techniques. One primary dielectric relaxation (gamma) was observed in the temperature and frequency ranges used and modeled using a Havriliak-Negami model. The associated activation energy of the relaxation was calculated to be 43 kJ/mol.

4.1 Introduction

A thermosetting resin material recently seeing greater use in aerospace composites [78, 79] is bismaleimide (BMI). BMIs are low molecular weight polymers or monomers, with at least difunctionality, all characterized by maleimide end groups on each repeating unit [28]. Different BMIs can have a variety of groups linking these two maleimide terminations together, however. Aliphatic linkages lead to more flexible resins, while aromatic linkages result in resins with greater high-temperature resistance [80, 81]. Additionally, the unsaturated carbon-carbon bond on the maleimide groups is highly activated due to the neighboring carbonyls, making it the region where crosslinking proceeds.

While much work has been documented on BMI cure kinetics [82, 83], the degradation of BMI is also an important factor to consider as implementation of this material into aircraft increases due its high-temperature usage ($\sim$290 °C),. Torrecillas *et al* studied the thermal degradation and stability of BMI-based networks by using mass-chromatography to analyze its degradation products [84, 85]. Musto *et al* reported extensively on the degradation mechanisms produced by long-term thermo-oxidative aging on epoxy-bismaleimide networks [86].

The present work is study on the degradation kinetics of a pure BMI resin. Small resin samples were degraded under a thermo-oxidative environment at constant heating-rates. The degradation profiles were modeled kinetically using two commonly utilized isoconversional kinetic models. Additionally, the dielectric properties of pure BMI resin were investigated as a function of both frequency and temperature. Dielectric relaxations were modeled using a Havriliak-Negami function, and the activation energies of the relaxation were determined via an Arrhenius extrapolation.

4.2 Experiment

Two sources of BMI resin were used in the analysis, both of which were RM-3002 resin supplied by Renegade Materials Corporation [10]. One source was BMI flash (excess resin) produced by the curing of BMI/glass-fiber prepregs (fiber weaves with resin pre-impregnated) purchased from Renegade. This resin (and prepreg composite laminate) was cured at 127 °C (260 °F) for one hour, followed by four hours at 190 °C (375 °F). The full temperature profile is shown in Figure 5.1. Once the laminate was finished curing, it was cut from the vaccuum bag into which excess resin had flown. This cured resin was removed in small chunks from the bag and placed in a desiccator until further use.

The second source of BMI resin was a cured resin casting prepared and supplied by Renegade. The casting had dimensions of 6.35 mm x 111.76 mm x 12.7 mm. This resin was cured under a different cycle from the BMI flash. The casting was under 127 °C (260 °F) for one hour, followed by six hours at 204 °C (400 °F). The casting was not post cured.

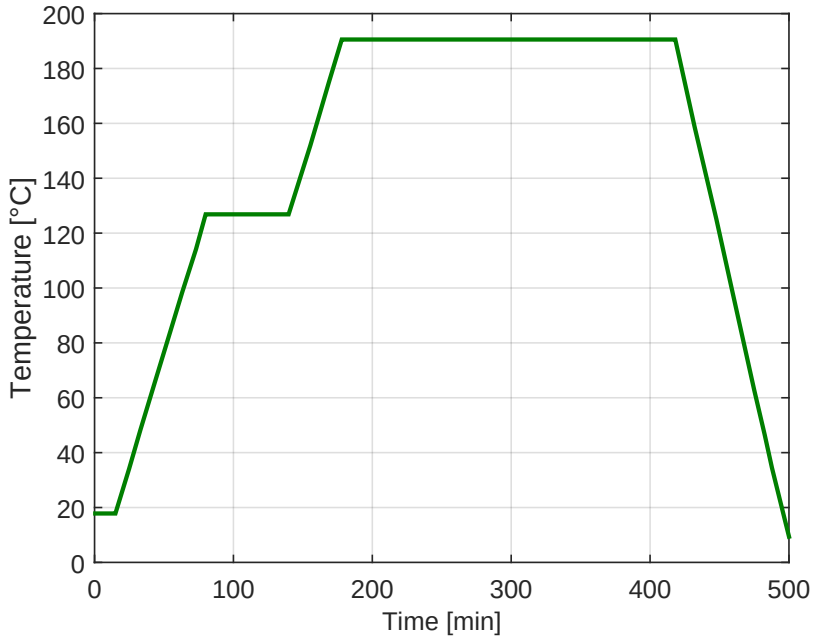

Figure 4.1: Temperature profile of the curing procedure for RM-3002 BMI flash, as detailed in [10].

4.3 Thermogravimetric Analysis

For thermogravimetric analysis (TGA), small flakes of resin, totaling ∼10-12 mg, were cut or broken from the larger chunks of flash. The samples were subjected to a degrading environment via a TA Instruments Q50 thermogravimetric analyzer. The furnace was purged with air at 60 mL/min, while the Q50 balance was purged with nitrogen at 40 mL/min. The temperature was increased at four heating rates, 5, 10, 20, and 50 °C/min, proceeding from room temperature to 900 °C. At all heating rates, the resin was fully degraded. The results of the degradation are shown in the themograms in Figure 5.3, and their temperature derivatives in Figure 4.3.

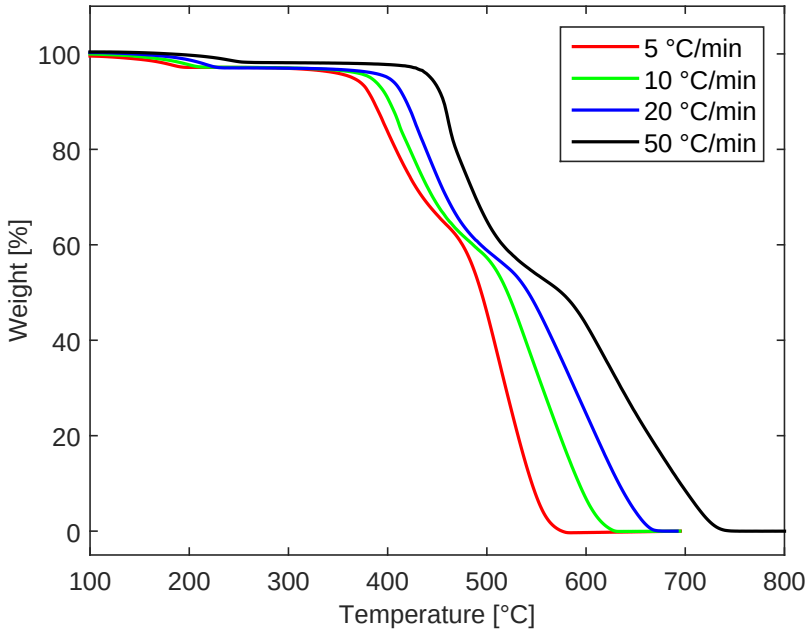

Figure 4.2: BMI mass loss as a function of temperature for four different heating rates.

4.4 Kinetic Modeling

The results in Figure 5.3 were analyzed kinetically. To aid in the complex analysis, NETZSCH ThermoKinetics3 software package was used, specifically the Friedman and Ozawa-Flynn-Wall analysis functions included in the software. Both models are based on the general reaction rate, which is defined as the time derivative of the amount reacted, or α. When calculating the reaction rate from a thermogram, such as Figure 5.3, α can be defined as $\alpha = 1-$

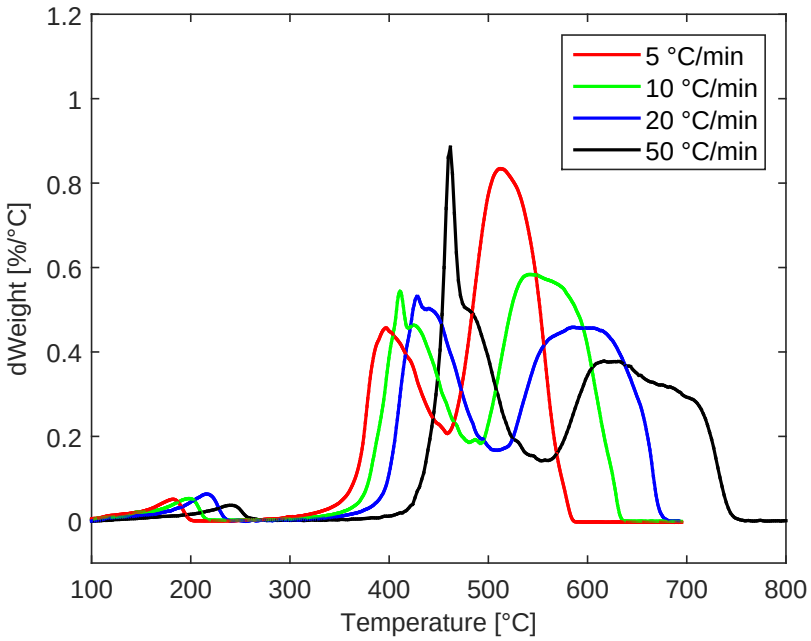

Figure 4.3: Temperature derivatives of the thermograms in Figure 5.3.

wt%, for each instantaneous weight percent. The reaction rate can then be written as:

$$\frac{\mathrm{d}\alpha}{\mathrm{d}t} = K(T)f(\alpha) \tag{4.1}$$

where $K(T)$ is the rate constant, and $f(\alpha)$ is a function of the reaction mechanism. Rather than determining the change with respect to time, the reaction rate with respect to temperature is often desired, as is the case in this research. This can be accounted for by multiplication of the constant heating rate β (dT/dt):

$$\beta\left(\frac{\mathrm{d}\alpha}{\mathrm{d}T}\right) = K(T)f(\alpha) \tag{4.2}$$

$$\tag{4.3}$$

The rate constant can be approximated by the Arrehnius equation:

$$K(T) = Ae^{(-E_a/RT)} \tag{4.4}$$

where E_a is the activation energy, and R is the gas constant. The Friedman and Ozawa-Flynn-Wall models utilize various reaction rate transformations in order to obtain the activation energy.

Friedman Analysis One of the initial model-free, isoconversional kinetic analysis methods was proposed by Friedman [71]. Model-free methodologies assume no particular mechanism(s) of degradation or reaction. Further, they do not require one to perform the analysis. The Friedman method is able to characterize the activation energies of multiple degradation mechanisms, that may or may not range in complexity. In the case of this research, the Friedman analysis presents itself as a viable tool for extracting the activation energies of the degradation steps.

The basis of the Friedman method involves taking the natural logarithm of each side of the reaction rate equation, Eq. 4.1 with Eq. 4.4 substituted, to produce

$$\ln\left[\beta\frac{\mathrm{d}\alpha}{\mathrm{d}T}\right] = \ln\left(Af(\alpha)\right) - \frac{E_a}{RT} \tag{4.5}$$

resulting in a linearization of the reaction rate equation. Plotting the left side of Eq. 4.5 against the inverse of the absolute temperature is referred to as a Friedman plot. A Friedman plot of the data from Figure 5.3 is presented in Figure 4.4. To determine the activation energy at a particular stage of conversion, corresponding α values are selected for each heating rate curve. A linear fit of these points form constant fractional mass loss (CFML) lines. The slopes of CFML lines are equal to $-E_a/RT$, from which the activation energy can be calculated. Additionally, obtaining the y-intercept of the CFML, as well as knowledge of $f(\alpha)$, can lead to calculation of the pre-exponential frequency factor A.

Ozawa-Flynn-Wall Analysis Another model-free isoconversional analysis method, the Ozawa-Flynn-Wall method, .

$$\frac{\mathrm{d}\alpha}{f(\alpha)} = \frac{A}{\beta}e^{(-E_a/RT)}\mathrm{d}T$$

Taking the integral of both sides leads to

$$F(\alpha) = \int_0^\alpha \frac{\mathrm{d}\alpha}{f(\alpha)} = \frac{A}{\beta}\int_{T_0}^{T} e^{(-E_a/RT)}\mathrm{d}T \tag{4.6}$$

Eq. 4.6 can be simplified as

$$F(\alpha) = \frac{AE_a}{\beta R}\int_{x_0}^{x}\frac{e^{-x}}{x^2}\mathrm{d}x = \frac{AE_a}{\beta R}p(x)$$

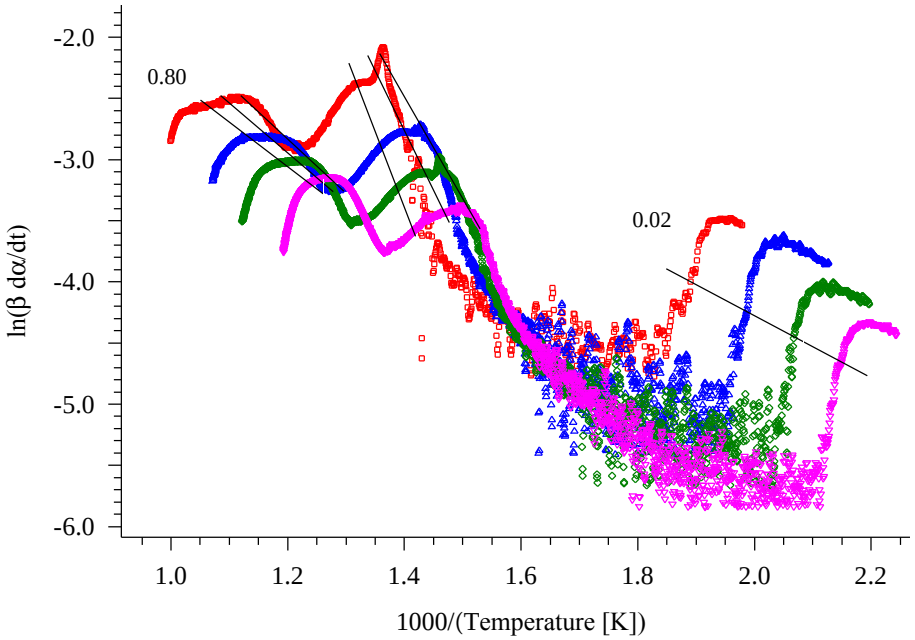

Figure 4.4: Friedman plot of the thermograms in Figure 5.3. CFML lines indicated in black are (increasing from right to left): α= 0.02, 0.10, 0.20, 0.30, 0.60, 0.70, and 0.80.

where $x = E_a/RT$. Taking the logarithm of each side

$$\log F(\alpha) = \log\left(\frac{AE_a}{R}\right) - \log\beta + \log p(x) \tag{4.7}$$

Doyle [74, 75] approximated $\log p(x)$ as

$$\log p(x) \cong -2.315 - 0.4567x$$

Substituting into Eq. 4.7 and differentiating at constant α:

$$\frac{\mathrm{d}\,\log\beta}{\mathrm{d}\,(1/T)} \cong -0.4567\frac{E_a}{R}$$

assuming A, $f(\alpha)$, and E_a are independent of T, and A and E_a and independent of α [73]. Rearranging and integrating leads to

$$\log\beta \cong -0.4567\frac{E_a}{RT} \tag{4.8}$$

The activation energy can be extracted from a plot of $\log\beta$ vs $1/T$ and, similar to the Friedman method, taking the slope of CFML lines. Using 4.8, with $R = 8.314$ J/mol K^{-1}, the activation energy is found to be

$$E_a \cong -18.20m \tag{4.9}$$

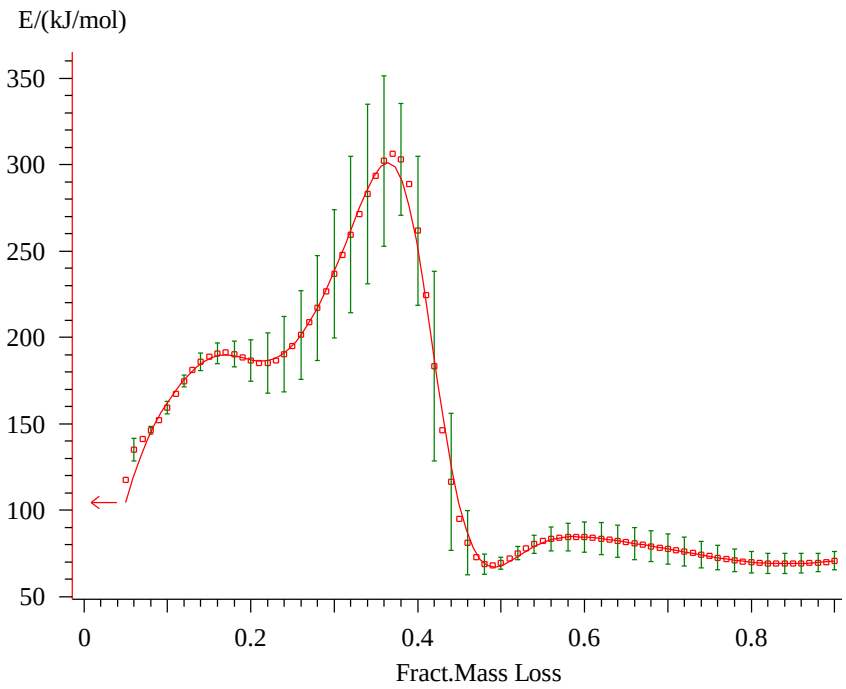

Figure 4.5: Calculated activation energy as a function of mass loss based on the Friedman plot in Figure 4.4.

where m is the slope of the CFML line. An Ozawa-Flynn-Wall plot, with CFML lines, for BMI resin is shown in Figure 4.6.

4.5 Dielectric Spectroscopy

For dielectric testing, a small rectangular sample of approximately 10 cm x 8 cm was cut from the resin casting using an Isomet 11-1180 Low Speed Saw. The sample was polished down to a thickness ~0.63 mm using a LECO Spectrum System 1000 polisher with 800 grit silicon carbide PSA discs, followed by 6 and 3 micron diamond suspensions. The thickness of the sample was measured with a Fowler Sylvac Mark IV digital indicator. Ten measurements at different points on the sample surface were made and the average used for permittivity calculations.

After polishing, the sample was dried in order to remove any potential data-skewing moisture. A Barnstead Thermolyne muffle furnace at 120 °C was used to dry the sample. The sample was placed on a steel shim in the furnace for two hours. After two hours, it was flipped

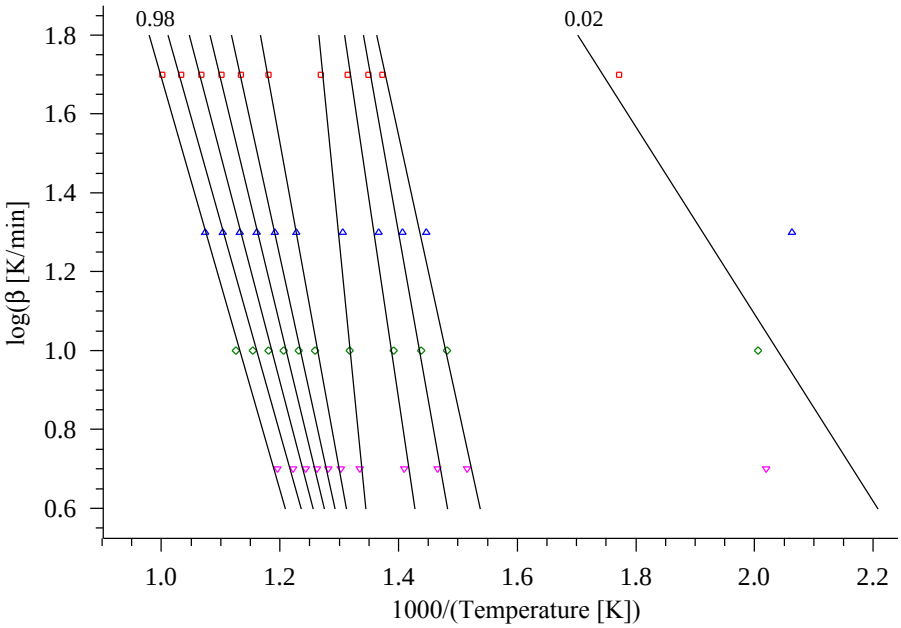

Figure 4.6: Ozawa-Flynn-Wall plot of the thermograms in Figure 5.3. CFML lines indicated in black are (increasing from right to left): α= 0.02, 0.10 to 0.90 by 0.10 increments, and 0.98.

to expose the covered side to the environment, and left in the furnace for another two hours. Once the four total hours of drying had passed, the sample was removed and placed in a desiccator to cool to room temperature.

Dielectric properties of the resin were measured using a Novocontrol dielectric broadband spectrometer (Novocontrol Technologies, GmbH & Co. KG) equipped with a ZGS active sample cell. The sample was sandwiched between two 10 mm-diameter brass electrodes (1.63 mm thick) and tightened between the two lead electrodes on the sample cell. The entire cell was then submerged into the cryostat of the Quatro Cryosystem. The sample was then cooled to -140 °C, stopping every ten degrees to take a measurement. After the measurement at -140 °C, the sample was heated back to room temperature for a measurement. The sample was then heated up to 160 °C, again stopping every ten degrees for a measurement, with the full temperature range being -140 °C to 160 °C. At each of the 31 temperatures, the real and imaginary permittivities were measured across a frequency range of 0.1 Hz - 1 MHz. Surface plots showing the real and imaginary parts of the permittivity as a function of both temperature and frequency are shown in Figures 4.8 and 4.9, respectively.

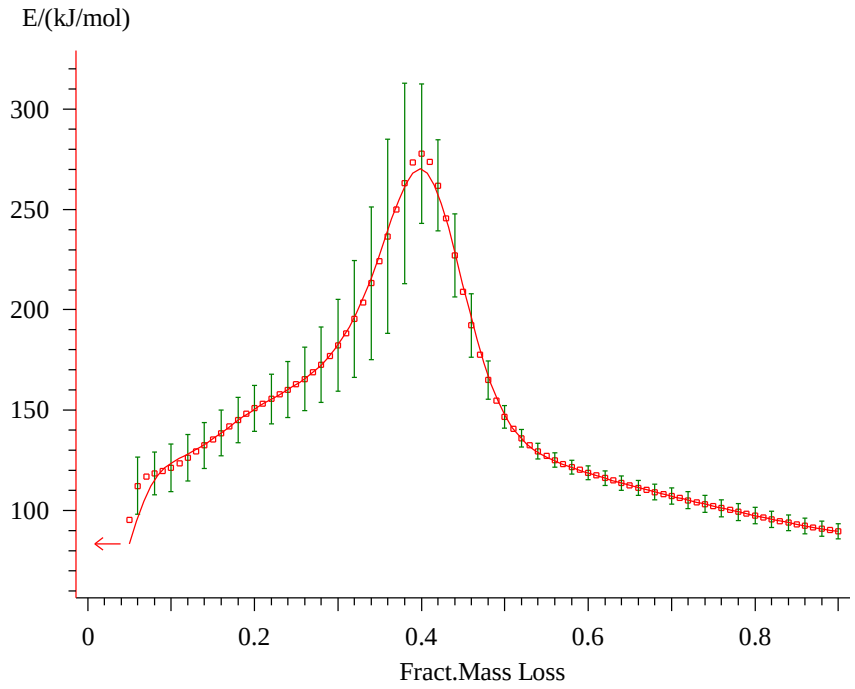

Figure 4.7: Calculated activation energy as a function of mass loss based on the Ozawa-Flynn-Wall plot in Figure 4.6.

At each temperature in the surface plot in Figure 4.8, the relative permittivity value decreases as the frequnecy increases. Additionally, at each frequency the relative permittivity increases as the temperature increases, up to ∼50 °C. At temperatures above this the permittivity starts to decrease.

The permittivity undergoes one major relaxation in the selected temperature and frequency ranges, as shown in Figure 4.9. The relaxation starts from ∼-120 °C and 0.1 Hz and extends to ∼50 °C and 1 MHz. This is a sub-T_g relaxation (T_g of the resin is ≥235 °C [10]), and a more detailed analysis of the relaxation will be described in the next section.

4.6 Dielectric Relaxation Modeling

In order to describe and model the behavior of dielectric relaxors, Debye proposed a model based on polar molecules, specifically polar liquids [87]. In Debye's model, each polar molecule in an electric field relaxes from a static, low-frequency, relative permittivity value (ϵ_s) to an optical, higher-frequency, relative permittivity value (ϵ_∞). This relaxation will be centered at

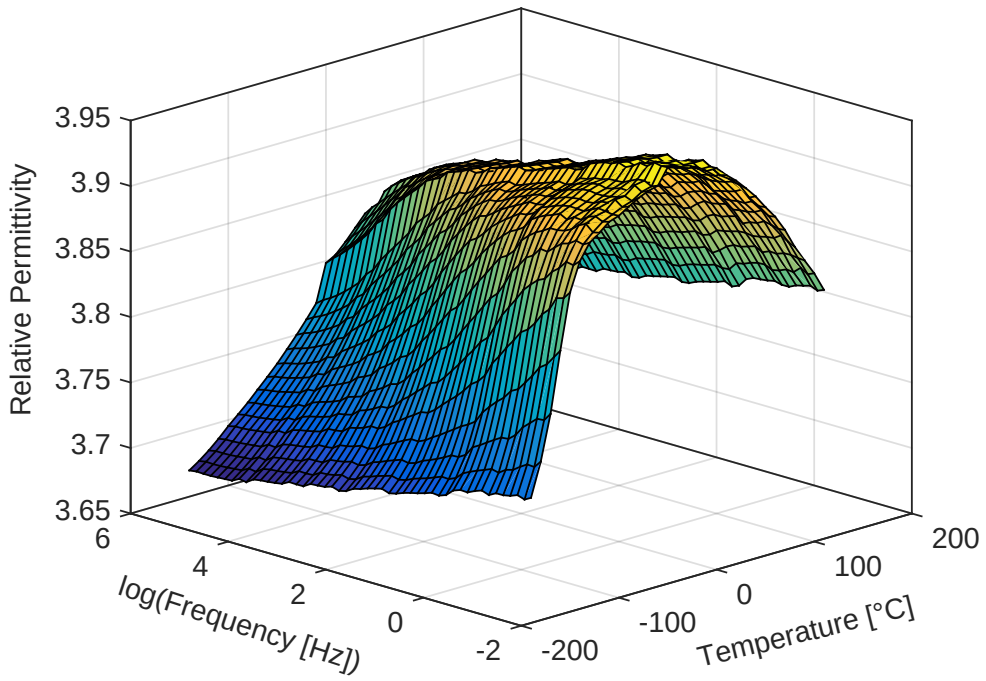

Figure 4.8: Surface plot of the relative permittivity as a function of both temperature (-140 °C - 160 °C) and frequency (10^{-1} - 10^{6} Hz).

a characteristic frequency described by the relaxation time τ. This is the time it takes for the polarization to decrease to $1/e$ of its maximum value. This can be thought of as the time a polarized molecule aligned with the electric field takes to 'relax ' back to a less-aligned state.

This relaxation from ϵ_s to ϵ_∞ is accompanied with a dielectric loss as well. This loss is represented as a peak, where the maximum is also centered at the characteristic frequency. The equation proposed by Debye to describe both components of the complex permittivity ϵ^* is

$$\epsilon^* - \epsilon_\infty = \frac{\epsilon_s - \epsilon_\infty}{1 + j\omega\tau} \tag{4.10}$$

where ω is the angular frequency.

Debye's model is able to aptly describe the behavior of gases and some liquids. The behavior of a large portion of solid dielectrics, however, cannot be described by this model. Modifications to Debye's model which have been widely accepted are the Cole-Cole model [88] and the Davidson-Cole model [89], which added shape and skewness parameters to the Debye model.

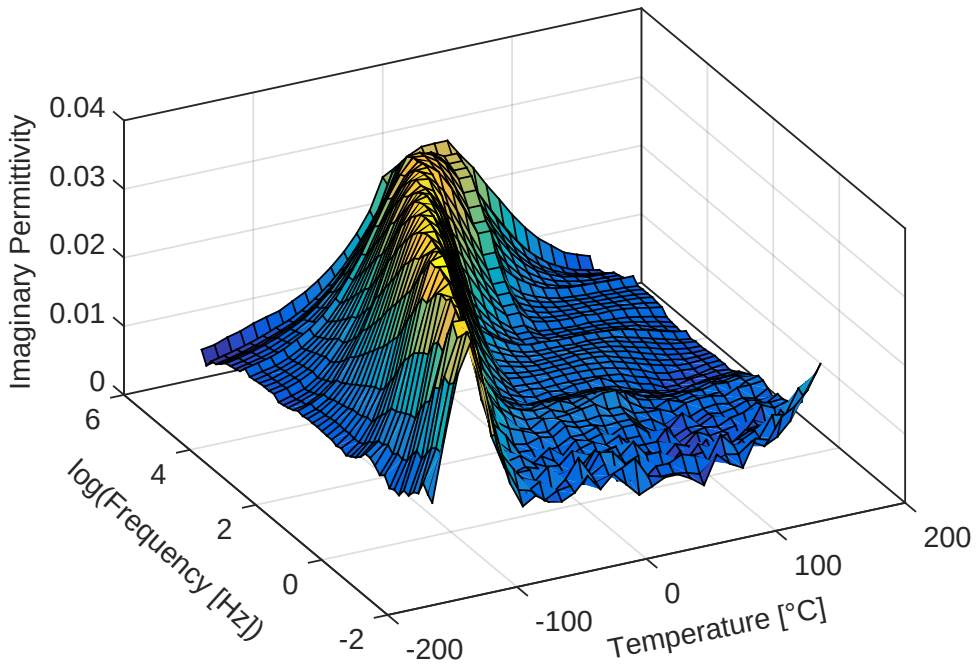

Figure 4.9: Surface plot of the imaginary permittivity as a function of both temperature (-140 °C - 160 °C) and frequency (10^{-1} - 10^{6}) Hz.

Both of these modifications allowed a larger variety of solid dielectric, non-Debye-like behaviors to be described.

Havriliak and Negami later proposed a further modification to the Debye model by incorporating both sets of changes from the Cole-Cole and Davidson-Cole models into

$$\epsilon^* = \epsilon_\infty + \frac{\epsilon_s - \epsilon_\infty}{[1 + (j\omega\tau)^\alpha]^\beta} \tag{4.11}$$

where α is a shape parameter, and β is a skewness parameter [90].

In addition to the behavior described by the Havriliak-Negami (HN) model, many dielectrics exhibit a conductivity at low-frequencies. To characterize this behavior, a conductivity term can be added to the HN model to fully describe the behavior of the dielectric, as shown below:

$$\epsilon^* = \epsilon_\infty + \frac{\epsilon_s - \epsilon_\infty}{[1 + (j\omega\tau)^\alpha]^\beta} - \frac{\sigma}{\epsilon_0 \omega^A} \tag{4.12}$$

where A is an exponential factor, and σ is the conductivity. However, as the data presented above does not appear to have experience any discernible low-frequency conduction, this con-

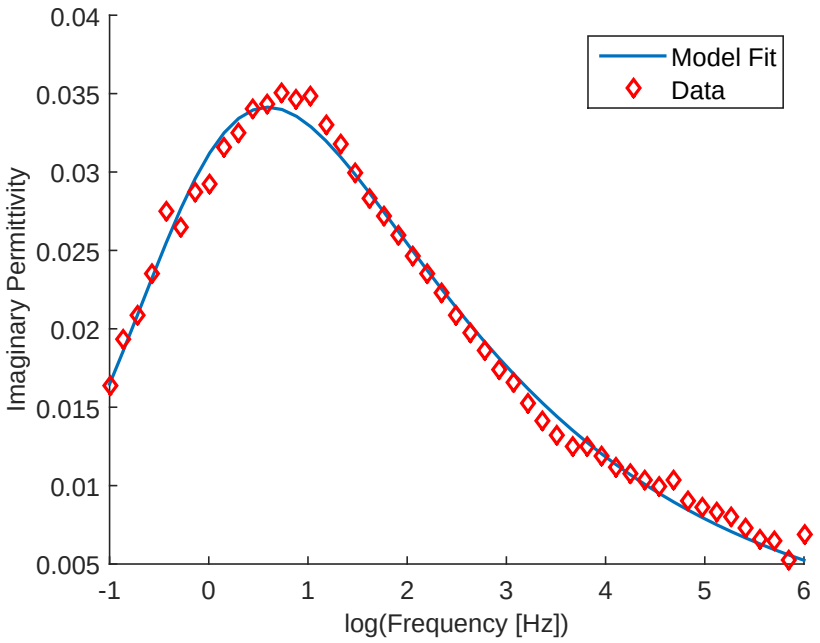

Figure 4.10: The model fit (blue line) of the measured imaginary permittivity of BMI resin at 183 K (-90 °C) from 0.1 Hz to 1 MHz. Model fit parameters are found in Table 4.1.

ductivity term will not be used in the following analysis.

The HN model can be fit to single-temperature dielectric spectra using computational minimization techniques. WinFit Dielectric Data Evaluation and Non Linear Curve Fitting software (version 3.2) provided by Novocontrol Technologies was utilized to obtain optimized data fits. Of the 31 tempeartures surveyed, the large relaxation shown in Figure 4.9 was primarily visible in ten temperature scans, from 163 K (-110 °C) to 253 K (-20 °C). The fit parameters for all ten temperatures are displayed in Table 4.1. As an example, a comparison between the model fit and measured data is shown for the imaginary permittivities at 183 K (-90 °C) and 203 K (-70 °C) in Figures 4.10 and 4.11, respectively.

Additionally, the relaxation time τ_{max}, the time where the imaginary permittivity is a maximum, was also calculated via WinFit. This calculation is dependent on the HN-calculated τ, as well as alpha and beta parameters. From Kremer and Schönhals [91]:

$$\tau_{max} = \tau_{HN} \left[\frac{\sin\left(\frac{\alpha\beta\pi}{2+2\beta}\right)}{\sin\left(\frac{\alpha\pi}{2+2\beta}\right)} \right]^{1/\alpha} \tag{4.13}$$

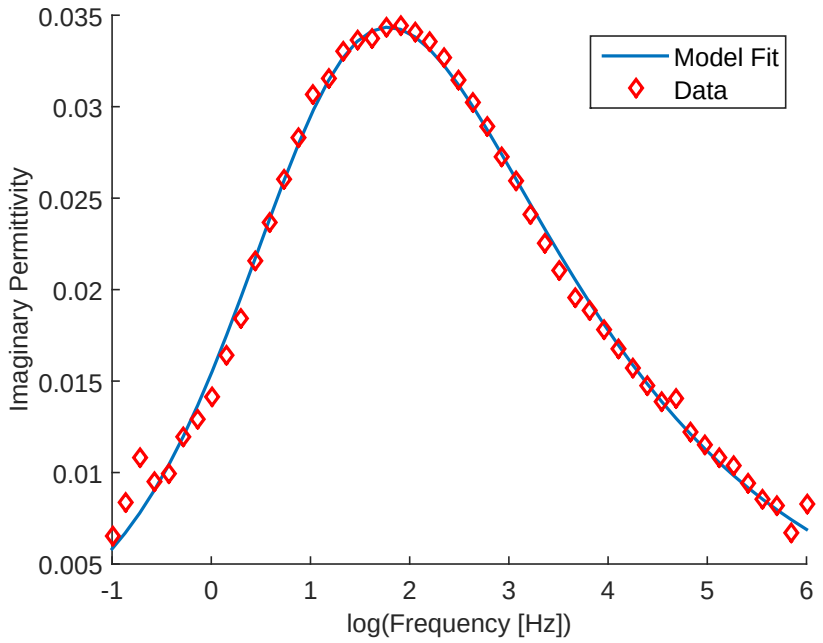

Figure 4.11: The model fit (blue line) of the measured imaginary permittivity of BMI resin at 203 K (-70 °C) from 0.1 Hz to 1 MHz. Model fit parameters are found in Table 4.1.

where the maximum frequency can be determined as $[\tau_{max} 2\pi]^{-1}$. Sub-T_g relaxations tend to follow an Arrhenius relationship [91, 92], and the maximum frequency data is used in an Arrhenius plot in Figure 4.12.

4.7 Discussion and Conclusions

From the kinetic analysis, BMI degrades via two major degradation mechanisms. From the Friedman plot in Figure 4.4, the first major degradation step appears to be either a normal or slightly accelerated reaction, based upon the slope of the data being slightly larger than that of the corresponding CFML lines. Similarly the second degradation step is accelerating for the same reasoning. The initial step appears to be the rate limiting step as both the Friedman and Ozawa-Flynn-Wall activation energy plots in Figures 4.5 and 4.7 have maximum activation energies near 0.3 to 0.4 fractional mass loss, which comprise the end of the first degradation step. Additionally, for both the Friedman and Ozawa-Flynn-Wall energy plots, the maximum energy is ~310 kJ/mol. The Friedman energy maximum occurs around 0.35 fractional mass loss, while that from the Ozawa-Flynn-Wall analysis occurs around 0.40.

Table 4.1: Havriliak-Negami Fit Parameters for Gamma Relaxation

T [K]	$\Delta\epsilon$	τ [s]	α	β
253	0.217	1.48e-05	0.352	1.00
243	0.216	3.35e-05	0.367	1.00
233	0.219	7.82e-05	0.370	1.00
223	0.226	3.38e-04	0.386	0.835
213	0.232	2.50e-03	0.444	0.565
203	0.236	1.33e-02	0.504	0.423
193	0.239	5.66e-02	0.537	0.363
183	0.245	2.77e-01	0.561	0.317
173	0.237	1.29	0.683	0.232
163	0.216	6.25	0.999	0.139

After both of these energy maximums, there is a severe drop in activation energy. For the Friedman case, the energy drops to between 70 and 80 kJ/mol and remains relatively constant for the rest of the degradation, with slight fluctuations. The Ozawa-Flynn-Wall energy shows a sharp drop to near 150 kJ/mol, and the proceeds to drop to just below 100 kJ/mol in linear fashion. This also agrees with the second major degradation step being accelerated. Accelerated mechanisms can often be auto-catalytic in nature, as has been shown for other imides [93].

From the beta parameters it is clear that for higher temperatures (253 K-233 K), the data is capable of being modeled using only the Cole-Cole equation ($\beta = 1$). This shows that as the temperature increases the relaxation becomes more symmetric. From the slope of the linear fit of the data in Figure 4.12, the activation energy of the relaxation was calculated as 43 kJ/mol. This is in agreement with gamma relaxations found in other imide-based materials [39]. For instance, the polyimide Matrimid® analyzed by Comer displays a similar relaxation from around 160 K to around 260 K, a similar range in which the relaxation described here resides. Similarly, this relaxation, identified as a gamma relaxation, displays linear Arrhenius behavior and an apparent activation energy of 43 kJ/mol, which again follows the BMI behavior. The magnitude of the relaxation times are somewhat different, however, despite a similar range of measurement frequencies (1 Hz to 1 MHz vs 0.1 Hz to 1 MHz in this study). The Matrimid® relaxation times span from 10^{-1} to 10^{5} Hz, while those for BMI range from 10^{-2} to almost 10^{10} Hz.

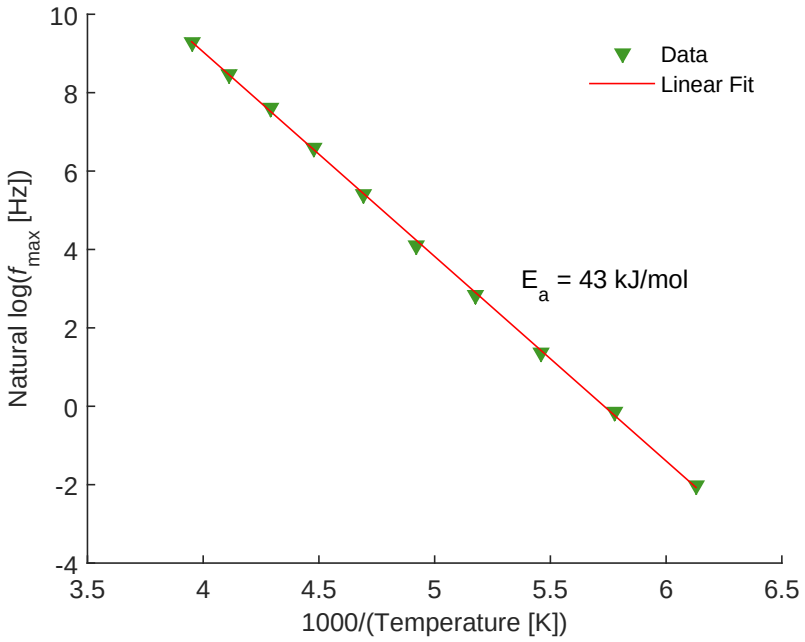

Figure 4.12: Arrhenius plot of the natural log of the maximum frequency for the relaxation at each temperature. Red line shows a linear fit with a calculated activation energy of 43 kJ/mol from the slope.

Comer describes the gamma relaxation as originating from motions involving the anhydride units (i.e. imide units) within the Matrimid® structure. This same imide unit is present in BMI, except that the nitrogen atom is the linking point to the other aromatic groups in the backbone. Motions from these units are thought to be primarily due to the permanent dipoles within them, which are mainly from carbonyl groups. The larger frequency range of the data in Figure 4.12 compared to that in Comer's work may be explained by the imide units in BMI presumably having more freedom due to the connectivity to the rest of the chain, as mentioned above.

4.8 Future Work

As two major degradation steps of BMI have been identified by kinetic modeling, future work will involve developing a degradation model to better describe the degradation. Additional use of the ThermoKinetics3 software by NETZSCH provides a variety of reaction models which can be tailored the types of reactions for each degradation step. These techniques have been

utilized to describe the degradation of Kapton, another imide-based thermoset [93].

With respect to the dielectric properties, additional studies will involve investigating how major relaxations, such as the gamma relaxation above, change as a function of thermo-oxidative aging. As the gamma relaxation in this study was determined to be due to carbonyl motions on the maleimide unit, changes to this or nearby structures could lead to changes in the characteristics of the relaxation. These changes, and similar changes for other relaxations, could potentially be utilized in monitoring composite systems containing BMI.

CHAPTER 5. DIELECTRIC AND INFRARED INFERENCE OF THERMO-OXIDATIVE AGING OF A BISMALEIMIDE COMPOSITE MATERIAL

Connor Daily, Nicola Bowler

Materials Science and Engineering, Iowa State University, Ames IA 50011, USA

To be submitted to *NDT & E International*.

Abstract

The degradation of a thermally-aged bismaleimide-glass fiber composite system was assessed via spectroscopic methods. Composite samples were subjected to accelerated isothermal aging at temperatures (275, 300, 325, 350 and 375 °C) near or above the upper usage limit of 290 °C. Broadband dielectric spectroscopy was used to measure changes in the dielectric spectra of aged composites from 200 Hz to 2 MHz, while chemical changes in the resin were identified with Fourier transform infrared photoacoustic spectroscopy. Additionally, samples were mechanically assessed via a double-notch compression test. Relationships between the dielectric, photoacoustic, and mechanical properties are inferred from the results.

5.1 Introduction

Polymer-matrix composite (PMC) usage in aerospace structures has steadily increased since one of their initial uses in aircrafts as sailplanes in the 1960s [12]. No more than five percent

of aircraft structures were made up of composite materials until the mid-1980s when the Airbus A320 and the McDonnell Douglas (Boeing) F-18A Hornet were produced, among others, having around twenty and ten percent of their structures made up of composites, respectively [13]. This percentage has continued to rise as improvements have been made in composite manufacturing, composite physical properties (structural, corrosive, thermal, etc.), as well as composites becoming more affordable. More recently, the Boeing 787 [17, 94] and the Airbus A350 [18, 94] have continued the increasing trend as their structures are comprised with over half of composite materials.

Composites are also finding increasing use in low-earth orbit (LEO) vehicles. The Dream Chaser Space System, a spacecraft designed by Sierra Nevada, uses composites in both primary and secondary structures (cabin, canted fins, etc.) [95]. Similarly, the Falcon Heavy rocket by SpaceX will utilize a composite fairing to transport cargo or smaller spacecraft, while the Falcon 9 rocket is equipped with both a composite fairing and composite interstage which holds the release and separation system [21, 22].

A resin material which has experienced wider use throughout the aerospace field in recent years is bismaleimide (BMI). BMI is a class of polyimide, with higher temperature resistance (up to 290 °C) than typical epoxies, but with similar processability [28]. In the Boeing 787, a BMI composite was used for fuselage barrel tooling as an enabler for its lighter tooling and faster heating and cooling rates, in comparison to the commonly used nickel-iron alloy Invar [96].

BMIs can be made from a variety of aromatic diamines [28], with a common feature among all being two maleimide end groups on each BMI unit. Depending on the desired use, different groups can used to link the two maleimide groups. Aliphatic groups are used for flexibility, while aromatic groups are used for high-temperature stability [80]. Crosslinking occurs at a double bond in these maleimide endgroups via a free-radical mechanism [81].

5.2 Experiment

5.2.1 Materials

BMI/glass-fiber prepregs (rolls of fibers pre-impregnated with partially cured resin) were purchased from Renegade Materials Corporation (RM-3002) [10]. The glass-fibers are style 7781 E-glass with a silane (497A) coating, and are in an eight-harness satin (8HS) weave. Single, 305 x 305 mm^2 (12 x 12 $in.^2$) plies (nominal thickness 0.31 mm) were cut from the larger roll then stacked and pressed to form laminates. For the dielectric measurements, to reduce uncertainty, the laminates comprised eight laminae, while those used for mechanical testing and IR analysis were made from sixteen laminae.

Once the laminae were stacked and pressed, they were sealed in high-temperature vacuum bags between perforated release film, which was sandwiched between bleeder cloth. The laminates were then pressed and cured in a Wabash Genesis Series Hydraulic Press (model G30H-15-BCLPX). Vacuum was pulled for a short period, followed by venting the vacuum and applying 586 kPa of presure, conditions specified in [10]. The temperature profile of the cure is described in Figure 5.1.

Upon removal from the heat press and vacuum bag, the cured laminates were subjected to a post-cure at 232 °C (450 °F) for six hours.

Following the post-cure, the samples were analyzed for uniformity by ultrasonic C-scan using an AIRSCAN SONDA-007CX Digital Ultrasonic Air-Coupled Test Instrument. The SONDA was equipped with 120 kHz transducers. The most uniform sections of the laminate, indicated by relatively low signal attenuation, were identified and marked. Using an IMER COMBI 1000 with a 355 mm (∼14 in) water-cooled diamond blade, samples were cut from the most uniform sections of the laminate. For the sixteen-ply laminates, strips 12.7 mm (0.5 in.) wide were cut, according to the requirements of ASTM standard D3846-08, for the mechanical testing [32]. Square 38 x 38 mm^2 (1.5 x 1.5 $in.^2$) samples were cut from the eight-ply laminates to be used for dielectric measurements, based on available electrode sizes. Thinner eight-ply rather than sixteen-ply samples were used for dielectric testing to reduce uncertainties due to fringing field (edge) effects.

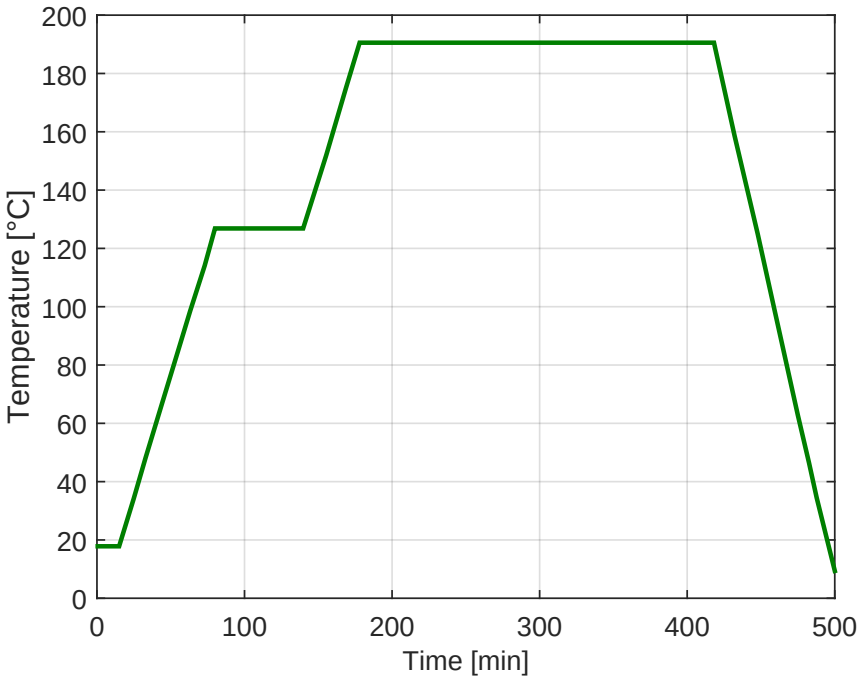

Figure 5.1: Temperature cure cycle for the BMI/glass-fiber composites (RM-3002). Vacuum was pulled initially, followed by venting and application of 586 kPa of pressure for the remainder of the cure cycle.

From each of the sixteen-ply strips, three samples with a nominal length of 79.5 mm (∼3.13 in.) were cut using a large diamond Dremel wheel ∼0.635 mm (∼0.025 in.) thick. To cut notches into these samples, detailed in [32], two small diamond Dremel wheels (also ∼0.635 mm thick) were stacked upon one another for a nominal thickness of ∼1.32 mm (∼0.052 in.), which is within the range specified for notch widths in [32]. Notches on each side were cut to half the strip thickness, approximately 36.3 mm (1.43 in.) from each end, as shown in Figure 5.2.

Additionally, a small block of cured BMI resin (1 hour at 260 °F, 6 hours at 400 °F, no postcure), supplied by Renegade, was cut into small squares with 13-mm sides. The resin was then polished to sub-millimeter thickness with a LECO Spectrum System 1000 polisher with 6 and 3 micron diamond suspensions. The samples were then subjected to the same drying and heat treatment as the composite samples above, with the exception of the 275 °C aging. Due to small amounts of material, only one sample was aged at each condition.

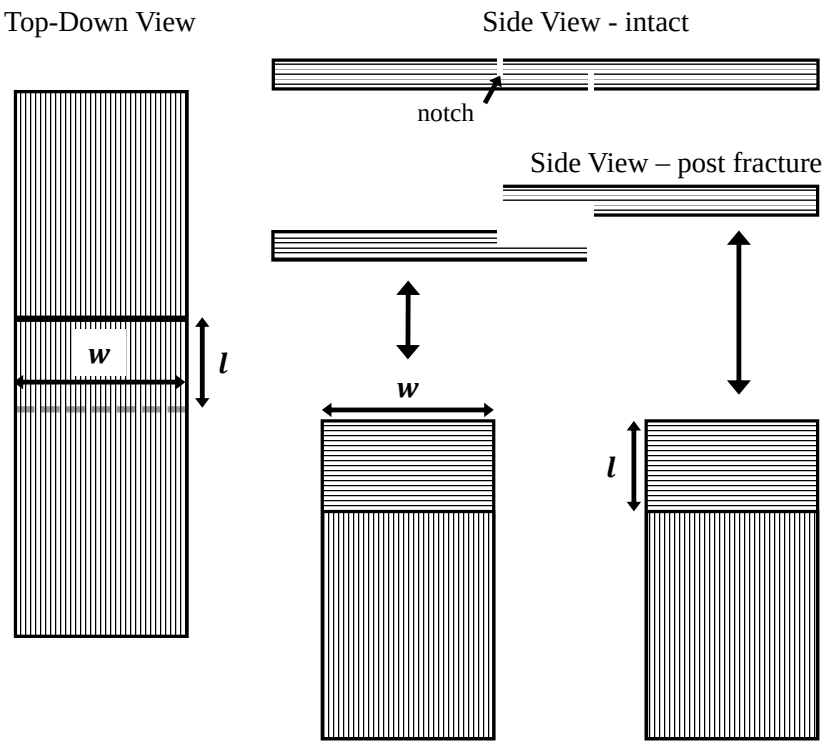

Figure 5.2: Schematic diagram showing the resultant fractured halves of the composite samples after compression testing. Multiplication of the width in the area between the two notches (w) and the failed length (l) leads to the failed area, and is utilized to calculate the ILSS in Equation 5.2.

5.2.2 Thermogravimetric Analysis

In order to help determine an appropriate range of aging temperatures, as well as investigate the degradation kinetics of the BMI, small samples (∼5-12 mg) of BMI flash (excess cured resin left in the vacuum bag) were subjected to thermogravimetric analysis (TGA). A TA Instruments Q50 thermogravimetric analyzer was used with platinum sample pans and a balance purge of nitrogen gas at 40 mL/min. Samples were purged under air at a flow rate of 60 mL/min.

Five different heating rates were used for TGA of the pure BMI resin samples: 2, 5, 10, 20, and 50 °C/min. The heating range was from room temperature (∼25 °C) to 800 °C, to ensure full sample degradation. The TGA results are shown as thermograms in Figure 5.3, with their temperature derivatives in Figure 5.4.

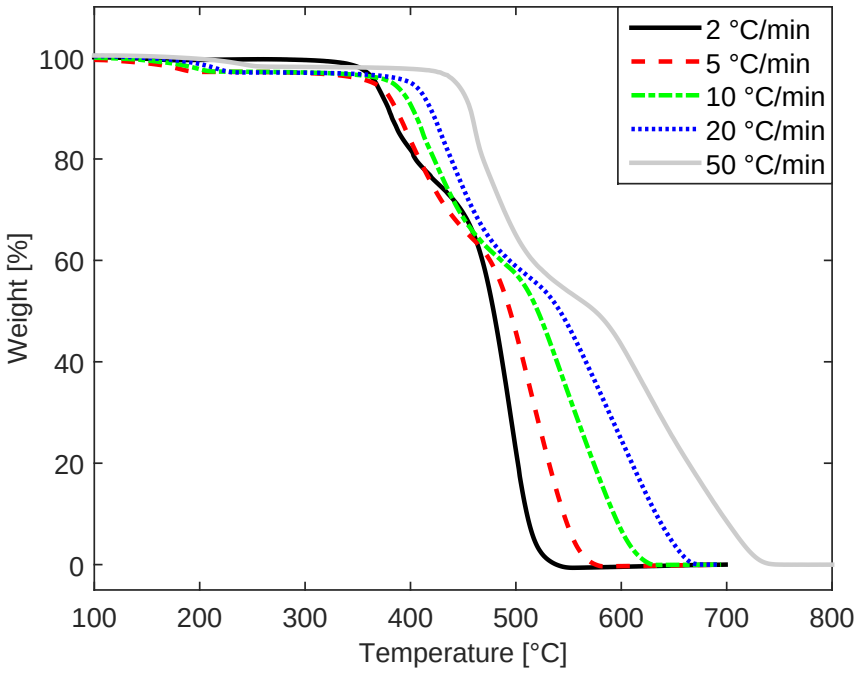

Figure 5.3: Mass loss percentages of cured BMI resin at five different heating rates: 2, 5, 10, 20, and 50 °C/min.

5.2.3 Isothermal Aging

Looking at the results shown in Figures 5.3 and 5.4, in particular the 2 °C/min trace (the closest to isothermal), it appears that significant degradation of the resin initially occurs near 350 °C. With a greater focus on varying aging temperature than on varying aging time, a set of aging temperatures were selected in the vicinity of 350 °C. An initial starting temperature of 150 °C was selected, but according to Stenzenberger [28], certain BMIs should have good temperature resistance up to 290 °C. A temperature slightly lower than this (275 °C) was selected as a baseline, therefore. Four additional aging temperatures, at 25 °C increments, complete the set: 300, 325, 350, and 375 °C.

A Barnstead Thermolyne benchtop muffle furnace was used to dry (at 120 °C) and subsequently age the samples, both eight- and sixteen-ply sets. The mass of each sample was measured and recorded before drying or aging using a Denver Instrument S-64 analytical balance (0.0001 g resolution). Upon equilibrating at the desired temperature (as verified by an external thermocouple), the samples were placed in the furnace on a 0.305 mm (0.012 in.) thick

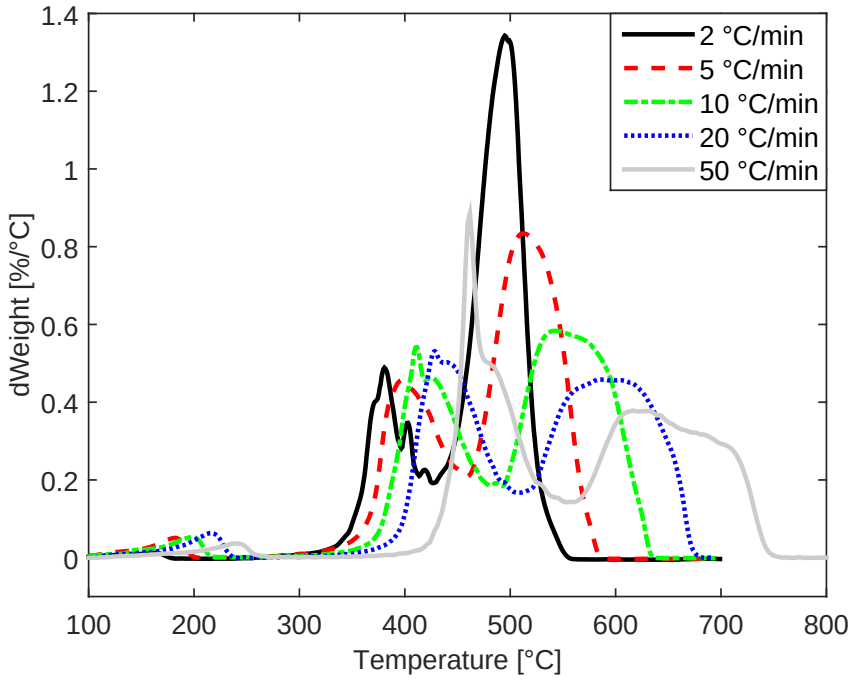

Figure 5.4: Temperature derivative of the weight percentages in Figure 5.3.

stainless steel shim. After the first two hours of aging, the samples were turned over so that both large surfaces were equally exposed to the environment. To reduce any potential effects of thermal shock, the furnace was turned off after the four hours of aging and the samples were allowed to cool *in situ* overnight. After arriving at room temperature, the samples were stored in a desiccator. Within one hour the sample masses were measured, and the samples were returned to the desiccator until further use.

The constituent percentages of the unaged sixteen ply samples were determined by following ASTM D3171: Procedure G [11]. The initial densities of three rectangular samples (not used in testing or aging) were calculated by dividing their measured masses by the product of their measured widths, lengths, and thicknesses using a Mitutoyo Digimatic Caliper (Model CD-4"CSX; 0.01 mm resolution).

Each of the three samples was then placed in a beaker of known mass and subsequently placed into the same muffle furnace described above at 500 °C. Each sample was left in the furnace for five hours, after which the beaker was removed and placed in a desiccator to dry overnight. Upon removal from the desiccator, the mass of the beaker and residual material

inside (glass-fiber weave) were then measured. Assuming all of the mass lost was resin, and using 1.26 g/cc and 2.57 g/cc for the resin and fiber densities, the mass and volume percentages of BMI resin in the sixteen-ply composites were calculated to be 21.25% and 34.26%, respectively.

5.2.4 Dielectric Spectroscopy

The capacitive properties of the aged eight-ply composites and BMI resin were measured using an Agilent E4980A LCR Meter equipped with a parallel-plate Agilent 16451B Dielectric Test Fixture. A 52-mm-diameter guarded ball-bearing electrode was used in conjunction with a secondary brass electrode (31.75 mm diameter, 3.175 mm thickness, R&B Wagner) to increase the electrode area on the composite. Both sides of the brass disc were polished using 1200 grit paper. The disc was then centered on one face of the composite sample. The guarded electrode was subsequently brought into contact with the secondary electrode, and sandwiched finger-tight using the fixture micrometer.

Measurements were taken in C_p mode at standard voltage 1 V in the frequency range from 20 Hz to 2 MHz, with each data point representing the average of 32 measurements. To further reduce the uncertainty in the data, three different sets of measurements were taken per sample, with the average and standard deviation of all three data sets being reported. For the aged resin samples, a 5-mm-diameter guarded electrode supplied with the 16451B was utilized without a secondary electrode.

Due to the geometry of the dielectric test fixture, the dielectric constant as a function of frequency was easily inferred from the capacitance using the following relation:

$$\epsilon_r'(\omega) = \frac{C(\omega)d}{A\epsilon_0} \tag{5.1}$$

where ϵ_r' is the dielectric constant, ω is the angular frequency (rad/s), C is the measured capacitance (F), d is the thickness of the composite (m), A is the electrode area (m^2), and ϵ_0 is the permittivity of free space (8.854×10^{-12} F/m). The electrode area was taken as the area of the secondary electrode (for composite measurements) and the area of the 5-mm-diameter guarded electrode (for resin measurements) while the thickness of each sample was the average of ten, 5 mm-diameter micrometer measurements taken at various points on the sample surfaces.

Similarly, the dissipation factor, D, of the composites and resin as a function of frequency was also measured. The dissipation factor is also known as the loss factor, and represents any conductivities or other dielectric losses. The dissipation factor can be related to the complex permittivity ϵ^* through

$$\epsilon^* = \epsilon'_r (1 - jD)$$

where D is

$$D = \frac{\epsilon''}{\epsilon'_r}$$

and ϵ'' is the imaginary component of the permittivity.

5.2.5 Mechanical Testing

The interlaminar shear strength of the sixteen-ply composite samples was measured according to ASTM D3846-08 [32]. According to [32], the procedure results in a measure of the in-plane shear strength of the material. It has been reported, however, that this procedure more accurately determines the interlaminar shear strength [33], and will be assumed as such from here on.

The widths of the sixteen-ply samples were individually measured in the area between the two notches (labeled w in Figure 5.2) and recorded, as an input to calculating the ILSS. The samples were then centered in a stainless steel jig detailed in [32], designed to prevent buckling of the fibers, and secured finger tight. The loaded jig was sandwiched between two compression plates on an Instron 5960 Dual Column Tabletop Universal Testing System and compressed at a speed of 1.3 mm/min.

Upon sample rupture the run was stopped, and the maximum load, $\sigma_{\max}$ (generally the load at rupture), was recorded. After removing the fractured sample halves, the failed length (labeled l in Figure 5.2) was measured on each half with calipers (0.01 mm resolution) and an

average of the two recorded. The ILSS was then calculated according to the following formula:

$$S_{\text{il}} = \frac{\sigma_{\max}}{wl} \tag{5.2}$$

The average ILSS of ten nominally identical samples per aging condition is reported.

5.2.6 FTIR Photoacoustic Spectroscopy

Photoacoustic spectroscopy (PAS) is an absorption-based technique used to otain an infrared spectra of a small amount of material [70]. A small amount of material is sealed in a sample cell with a gas, in this case helium. The sample is exposed to intensity-modulated IR radiation at a particular frequency (2.5 kHz) which heats the sample surface. As the intensity is lowered, the heat on the sample surface flows into the surrounding gas, leading to expansion. Once this heat dissipates, the gas contracts back to its original state. The system oscillates between these two states at the same frequency as the intensity modulation of the IR radiation. A small microphone, coupled with both lockin and preamplifiers, can detect the pressure oscillations created by the gas. This data is then Fourier transformed to obtain the IR spectra as a function of wavenumbers (cm^{-1}). Due to the absorption-based nature of the technique, PAS is useful for samples where transmission or reflectance is non-ideal, such as for opaque composites [30].

The photoacoustic spectra were obtained with a Digilab FTS 7000 FTIR spectrometer and an MTEC Photoacoustic, Inc. Model 200 photoacoustic detector. The spectral range was 450-4000 cm^{-1} and the spectral resolution 8 cm^{-1}. 256 scans of each sample were co-added to produce a single spectrum, with the spectrometer in rapid-scan mode. An initial background scan on a carbon-black foam was ran to measure the the spectral features from the sample cell and IR source, which are ratioed and subtracted from sample spectra. Afterwards, small square samples ($\sim$4 mm/side) cut from the fractured composites were placed in the sample holder. A small amount of desiccant was placed below the sample platform in the holder to help absorb any moisture residing on the sample surface. After placing the sample holder into the sample cell of the detector, helium purge gas at a flow of 10-20 cc/min was passed over

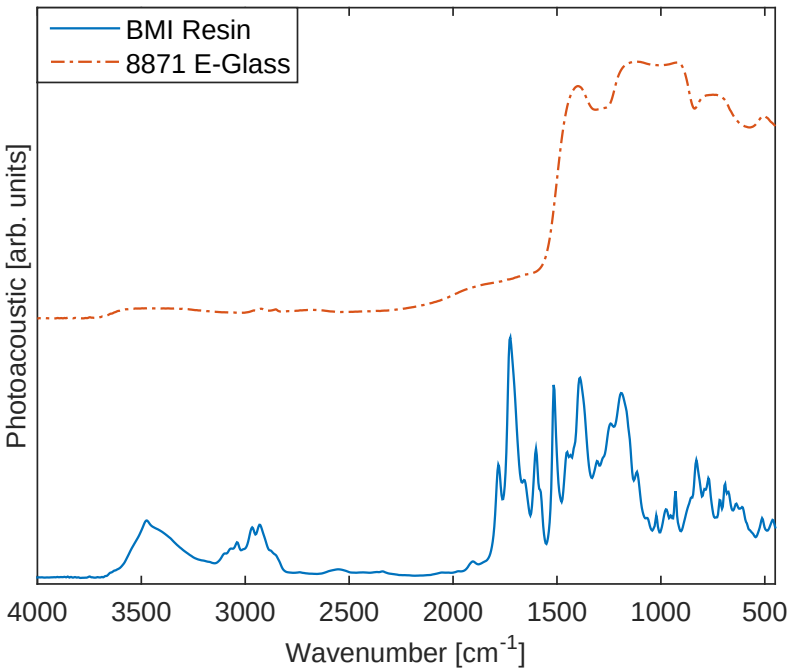

Figure 5.5: IR spectra for unaged BMI resin (bottom, solid) and 8-harness satin 8871 style E-glass fiber weave obtained from constituent measurements of BMI/glass-fiber composites, as outlined in [11](top, dashed). While feature and peak locations are maintained, intensity comparisons between the two spectra should not be assessed.

the sample to help remove any further moisture. PAS FTIR measurements were made on six nominally-identical samples and the results averaged.

5.3 Results and Discussion

The average mass loss resulting from the isothermal aging procedure is shown in Figure 5.6. Both the eight- and sixteen-ply samples exhibited similarly increasing trends in the percentage of composite mass lost. Precise percentage variation between the two data sets at corresponding temperatures can be credited to differences in surface area due to sample geometry.

Assuming that all of the composite mass lost in the aging procedure was from the resin, results from constituent calculations were used to determine the resin percentage lost. The percentage of resin lost within the 16-ply composites was near 18% for the samples aged at 375 °C, and under 5% for all other aging conditions.

Relative permittivity and dissipation factor spectra of the eight-ply aged composites are

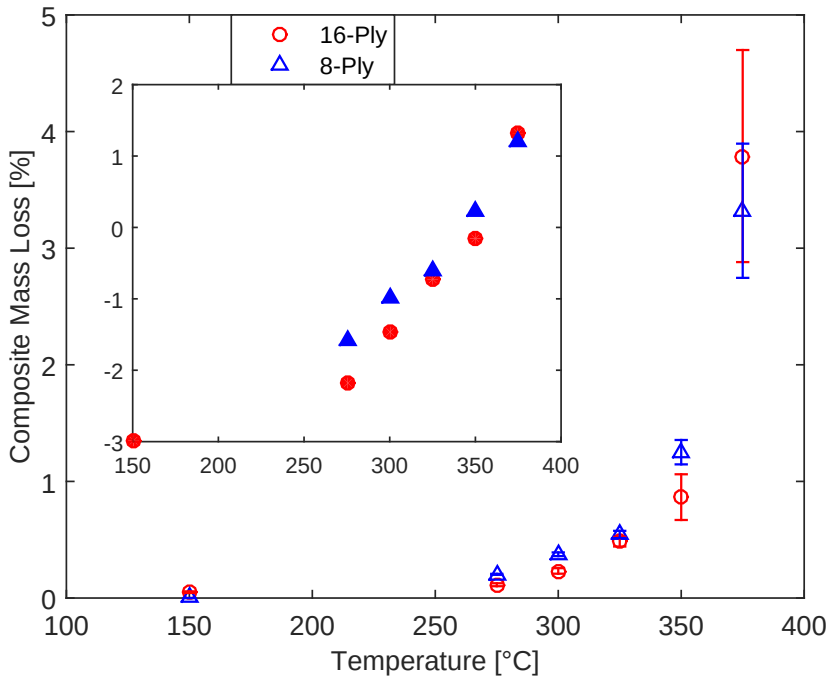

Figure 5.6: Percent of sixteen-ply (circles) and eight-ply (triangles) composite mass lost at each aging temperature. Error bars represent one standard deviation above and below the average of ten samples (sixteen-ply) and three samples (eight-ply). Inset shows natural log of percent composite mass loss, at each aging temperature.

presented in Figures 5.7 and 5.8. Looking at the relative permittivity data in Figure 5.7, there is little to no change in the dielectric constant between the neat (120 °C) sample, and the 275 °C, and 300 °C aged samples. At higher aging conditions, there is a general decrease in the dielectric constant at all frequencies, with the decrease becoming more severe at higher aging temperatures, except at 350 °C.

The dissipation factor spectra also reveal some trends due to different aging conditions. At aging temperatures above 275 °C, the onset of a loss peak is either decreased or shifted to higher frequencies. This holds true for the 350 °C samples as well. Low frequency results (¡1 kHz) were not included due to increased noise.

The dielectric results for the BMI resin are shown in Figures 5.9 and 5.10. The real permittivity results in Figure 5.9 share some trends with those for the composite permittivity in Figure 5.7. For instance, the resin permittivity also decreases as the aging temperature increases, except for the 350 °C case. The dissipation factor results, however, do not follow the

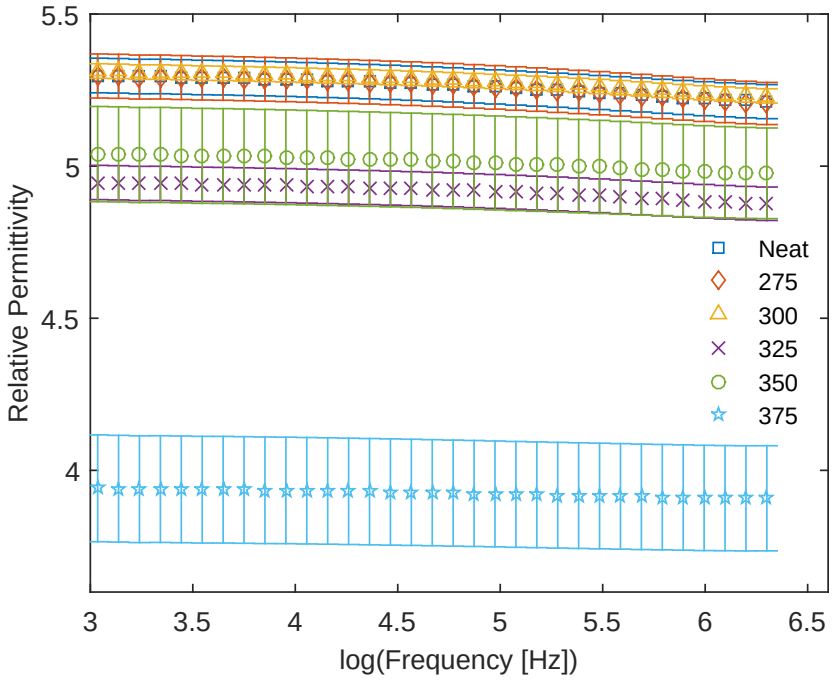

Figure 5.7: Relative permittivity results for eight-ply composite samples. Each spectrum represents the average of nine spectra, with error bars representing one standard deviation above and below the average.

same trends. An increase in dissipation factor is observed for aging temperatures above 150 °C at frequencies above 10^5 Hz. The sample aged at 375 °C shows similar behavior as the sample aged at 150 °C, however.

For the 350 °C scenario in both the composite and resin material, the increase in permittivity above the 325 °C aged sample may be caused by a variety of changes due to aging. One common change due to aging is residual curing in the resin. This can cause polymer molecules to become more restricted, which can lead to a decrease in the dielectric constant. Once the resin is fully cured, further aging will begin to lead to degradation, which generally gives molecules more freedom, and increases the dielectric constant.

To investigate this explanation, dynamic scanning calorimetry (DSC) was performed on a variety of composite and resin samples, using a TA Instruments Q20 at 20 °C/min, to possibly observe any exothermic signals, indicating residual curing. In Figure 5.11, a large, broad exothermic peak is observed for a sample of uncured prepreg material, starting around 160 °C and ending just after 300 °C. Looking at the scans for aged composites, however, there

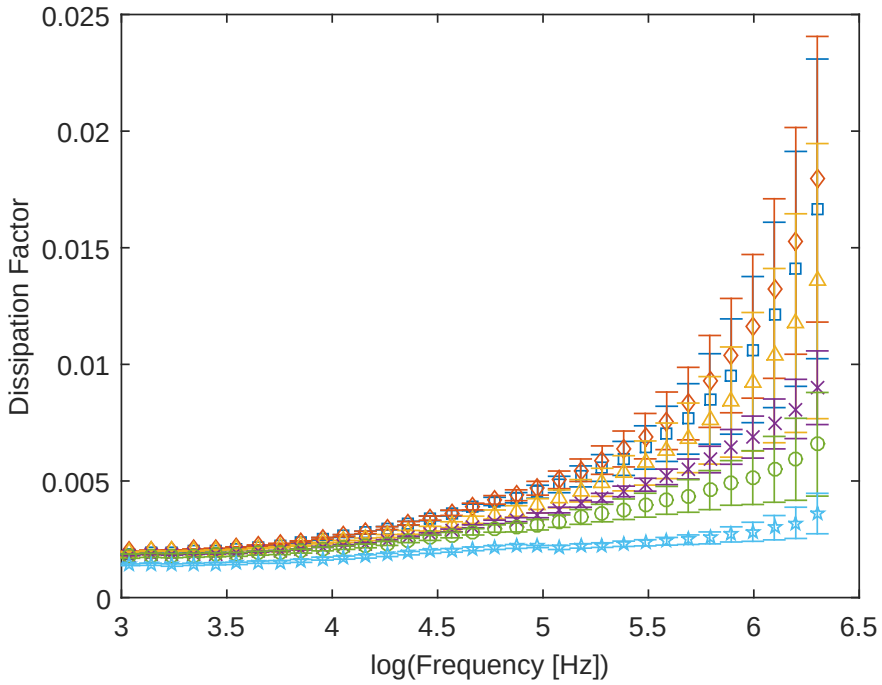

Figure 5.8: Dissipation factor results for eight-ply composite samples. Each spectrum represents the average of nine spectra, with error bars representing one standard deviation above and below the average.

appear to be no signs of any exotherms, indicating a fully cured resin. Further inspection of the derivitatives, shown in Figure 5.12 reinforce this.

DSC results on the BMI resin samples show similar trends. For a larger temperature range, BMI resin samples also did not show any exothermic signals, indicating fully cured resin. There appears to be an endothermic signal, however, which appears in all of the aged samples. This is most likely a crystallization peak, as BMI is a crystalline polymer. This crystallization endotherm appears to shift to lower temperatures as the aging temperature increased. Possible changes in the crystalline structure of the BMI could be affecting its dielectric properties. These changes could be identified with x-ray diffraction techniques, but were not investigated in this research.

The interlaminar shear strength results from compression testing are given in Figure 5.15. Little variation occurred in the ILSS values between the 150 and 275 °C samples, with a slight increase at 275 °C attributed to residual curing of the matrix at the elevated temperature. At aging temperatures above 275 °C there is a significant decrease in the ILSS values. Variations

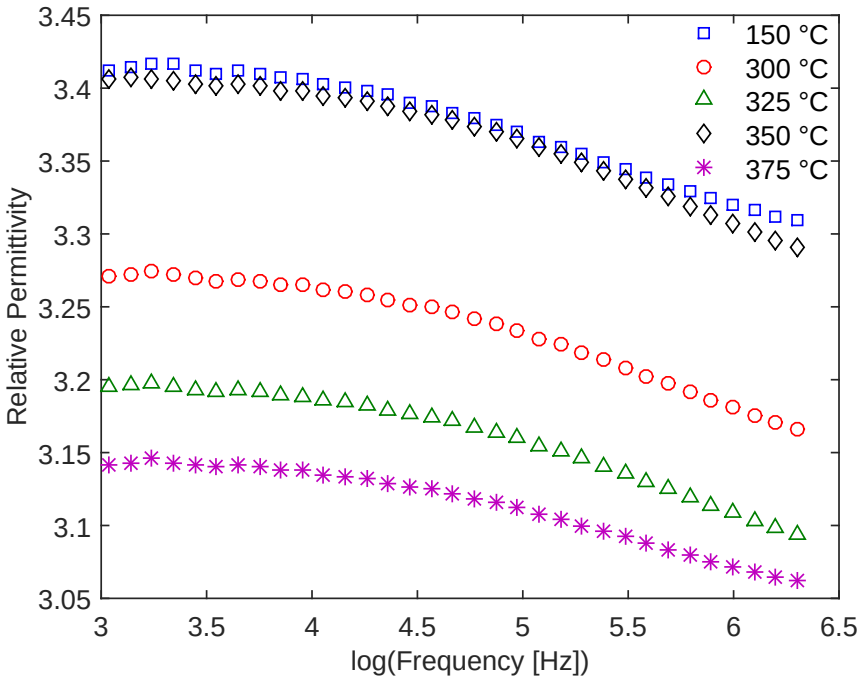

Figure 5.9: The real permittivity results for aged BMI resin.

in the results can be attributed to the uncertainty in the compression test.

Akay *et al* has performed long-term aging results on BMI-based composites [35], where mass losses at 210 °C totaled around 4% after 2000 hours, similar to the 375 °C aged samples in the present work. Increased mass losses are observed for higher temperatures (230 and 250 °C), reaching as high as 16% composite mass lost after 2000 hours, in some cases. Additionally, for the 250 °C case, 4% mass loss is reached near the 200 hour mark. The severity of the mechanical property deterioration shown in the present work at only 4% mass loss would presumably be enhanced after 16%.

Normalized photoacoustic spectra measured from the aged samples are given in Figure 5.16. The spectra were normalized by selecting maximum and minimum wavenumbers at which the corresponding features were unaffected by the aging procedure. In Figure 5.16, 2200 cm^{-1} was chosen as the minimum, while the feature near 1395 cm^{-1} was chosen as the maximum. The difference in photoacoustic signal between the two wavenumbers in a reference spectrum was used as the value to scale to. In the case of Figure 5.16, the spectrum produced by the samples aged at 150 °C was used as the reference.

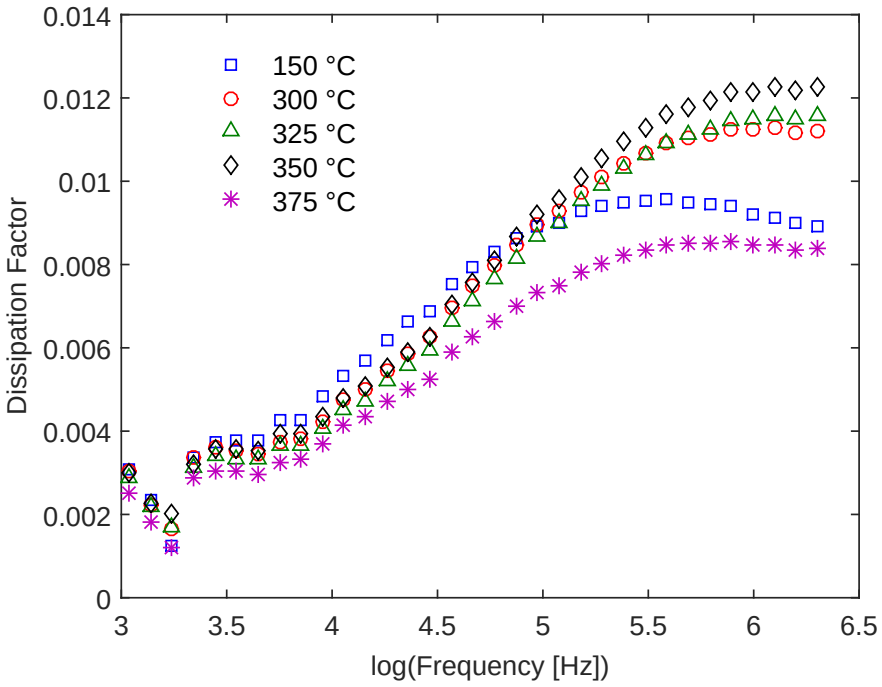

Figure 5.10: The dissipation factor results for aged BMI resin.

The feature of interest is the peak near 1720 cm^{-1}, representative of the carbonyl functional group. In a single BMI unit, or mer, each of the two maleimide end groups contain two carbonyls: a total of four per unit. This relative carbonyl abundance within BMI is reflected by the large photoacoustic signal at 1720 cm^{-1} in the spectrum of the 150 °C aged samples. As the aging temperature was increased, however, the peak at 1720 cm^{-1} started to decrease. This is in addition to overall broadening of BMI features as aging occurs, due to changes in chemical bonds affecting IR absorbtion frequencies.

It is difficult to determine whether the characteristic carbonyl peak is decreasing in intensity due to actual loss of carbonyl groups in the resin, which is mentioned to occur during pyrolysis [85, 84, 97], or as the entire absorbance from the BMI is decreasing across the spectral range by the aging process. Regardless, the carbonyl peak is a good indicator of determining different aged states of the composite.

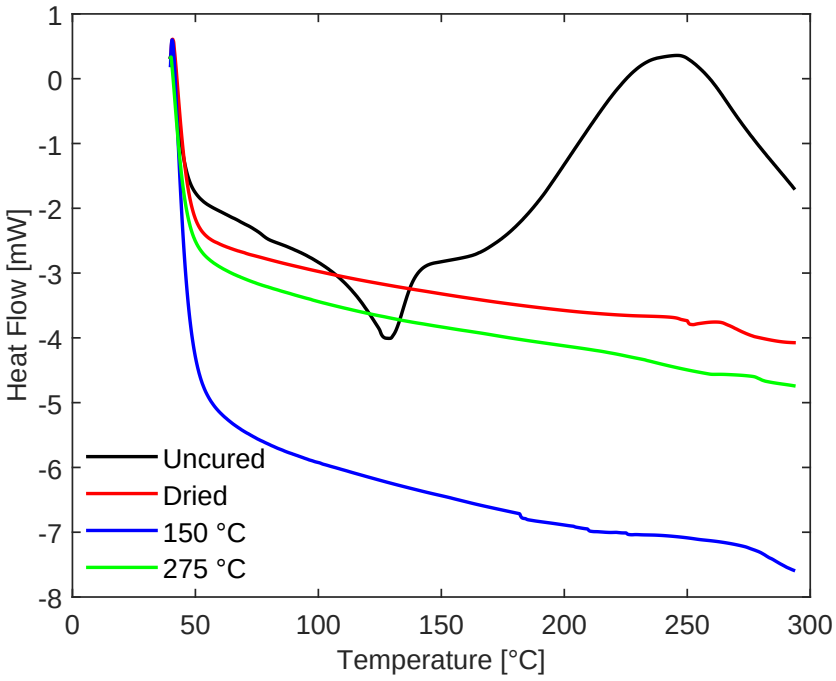

Figure 5.11: DSC scans for uncured and aged composites (exotherm up). Aged composites show no exothermic signals.

5.4 Conclusion

The viability of dielectric and IR sensing as an NDE technique for detecting thermo-oxidative aging has been explored. From the correlation values in Table 5.1, clear trends are visible between the destructive properties (ILSS and mass loss) and the NDE indicators (permittivity and IR). For dielectric correlations, the 8-ply mass loss was used, while with ILSS and IR correlations, 16-ply mass loss was used. Changes in the permittivity could be due to degradation and chemical changes in the resin, small voids on the surface and/or throughout the sample, from slight residual curing after the manufacturer recommended cure cycle, or a combination of all three.

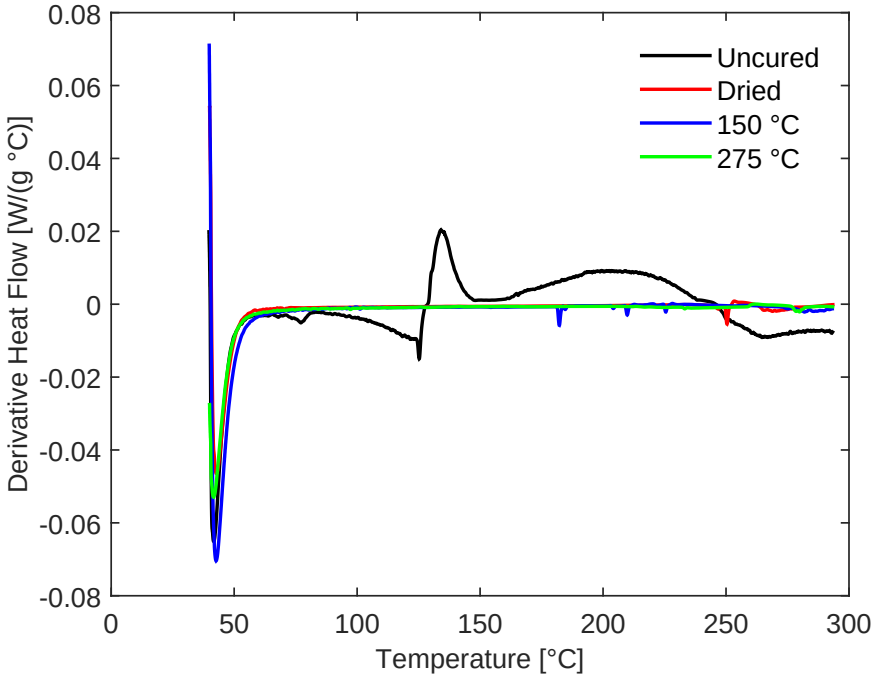

Figure 5.12: Derivative of the DSC scans in Figure 5.11 for uncured and aged composites.

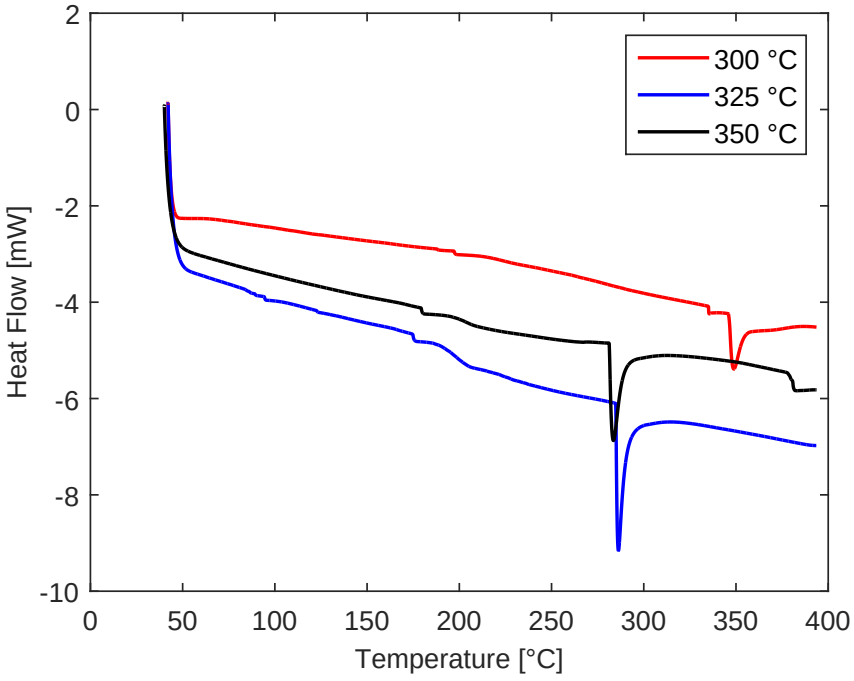

Figure 5.13: DSC scans for aged BMI resin (exotherm up). Aged resin samples show no exothermic signals, but do show crystallization endotherms.

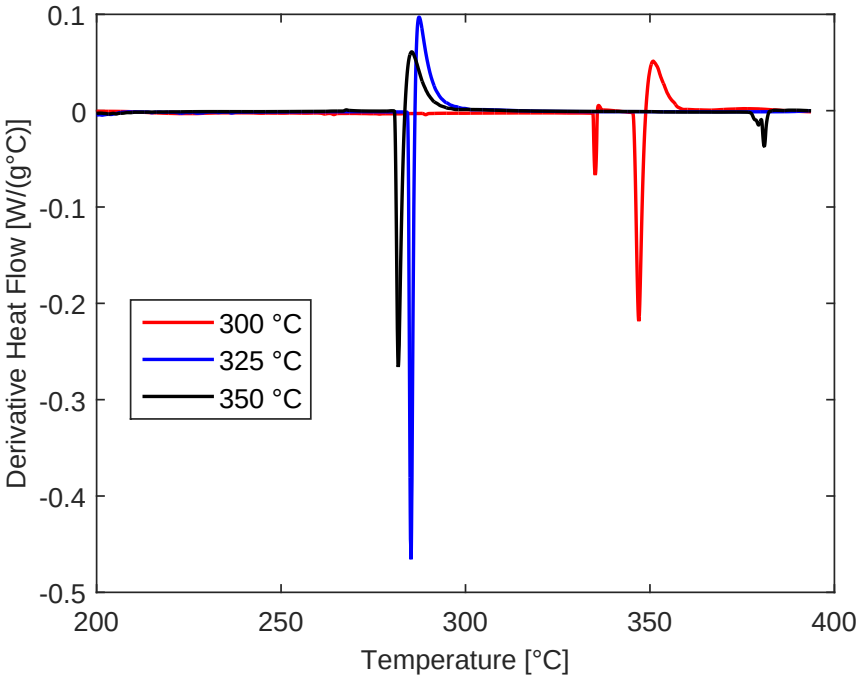

Figure 5.14: Derivative of the DSC scans in Figure 5.13for aged BMI resin.

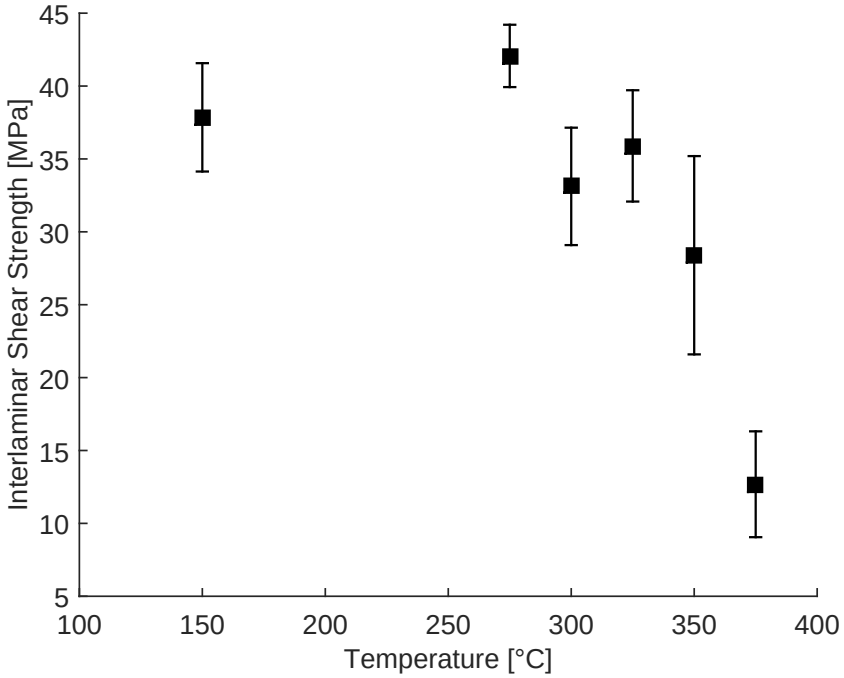

Figure 5.15: Interlaminar shear strength values for sixteen-ply composites at their corresponding aging temperatures. Error bars represent one standard deviation above and below the average of ten samples.

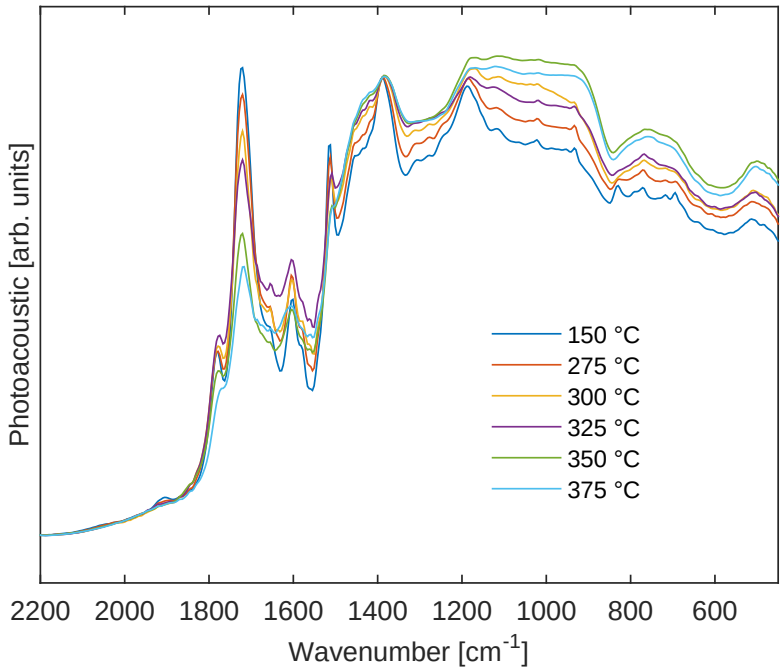

Figure 5.16: Photoacoustic spectra measured from six differently aged composite samples. The spectra are normalized to the 2200 cm^{-1} band as a minimum, and 1395 cm^{-1} for the maximum. A sequential decrease in the carbonyl band around 1720 cm^{-1} was observed as the aging temperature increased. Each spectrum is the average of six sample measurements.

Table 5.1: Correlation Values Between Selected Inidicators and ILSS and Mass Loss

		ILSS	Mass Loss
ϵ'_r	1 kHz	**0.92**	**-0.98**
	1 MHz	**0.92**	**-0.98**
D	1 kHz	**0.94**	**-0.98**
	1 MHz	**0.90**	-0.84
FTIR 1720 cm^{-1} peak magnitude (relative)		0.88	-0.81
ILSS		1	-0.95
Mass Loss		-0.95	1

CHAPTER 6. CONCLUSIONS

The two goals of this research, as stated in the introduction, were to utilize a new interphase model to help explain discrepancies between and theoretical and experimental properties of nano-composites, and to identify new indicators of thermo-oxidative aging in polymer-matrix composites. From the preceding chapters, it has been shown that these discrepancies can be modeled with use of reasonable interphase parameters, and changes in the dielectric and IR spectra can provide indication of thermo-oxidative aging, which can lead to loss of mechanical strength, specifically the ILSS.

The interphase dielectric model was able to successfully fit data from two different systems: one experiencing an anomolous drop in permittivity at low volume fractions of nanoparticles; one a thermosetting resin. The system showing anomolous behavior (LDPE/Al_2O_3) was determined to have a range of interphase properties. The interphase thickness varied from 5 to 22 nm (for average nanoparticle radius of 20 nm) with increasing interphase relative permittivity values as the thickness increases. In this case, the interphase permittivity was taken to be less than that of the matrix, to account for the permittivity drop at low loadings.

For the thermoset data (BECy/Si), the interphase thickness spanned a wider possible range than in the previous system, ranging from 15 to 42 nm. The average nanoparticle radius for this system, however, was 65 nm. Additionally, the possible values predicted for the interphase permittivity tended to decrease as the interphase thickness increased, as the interphase permittivity was able to be larger than the matrix value.

For both systems, although discrete values were given to the interphase parameters, a more realistic description of the interphase properties is a gradient of values slowly changing as the distance from the particle increases. For this reason, the ranges of interphase thickness and permittivity values presented represent possible points along this gradient, offering more realistic characteristics.

Regarding the dielectric properties of thermo-oxidatively aged bismaleimide-based polymer-matrix composites, the permittivity was generally shown to decrease as the aging temperature was increased. It is believed that this decrease is caused by factors due to aging. The first is a decrease in the permittivity of the BMI resin component. This was verified by subjecting small samples of resin to the same aging conditions as the composite samples, and measuring the dielectric constant and dissipation factor.

Another factor may be the presence of voids in the composite material which are promoted by aging. Due to the sensitivity of the permittivity measurements, these new small air gaps lead to a measurement of a three-phase composite material: BMI resin, glass-fiber reinforcement, and air. Additionally, the degree of mass loss in each of the samples (no greater than 5% of the composite) is comparable to other BMI-based composite studies of long-term isothermal aging [35]. For instance, there is a clearer decrease in the dielectric constant and dissipation factor for samples aged at 325 °C than the unaged samples. The same mass lost by the 325 °C sample is the same for a similar-sized BMI-based composite at 210 to 230 °C for less than 200 hours [35].

From the kinetic study of BMI, it was found from the CFMLs in the Friedman analysis that the main degradation mechanisms in BMI were accelerated. This means that the steps were not diffusion-based, and that time is not a primary factor in determining how it degrades. However, it has been shown that BMI degradation is extremely sensitive to oxygen [84, 85]. This means that with increased time, even further degradation than observed in this research would be expected to occur.

The two types of permittivity changes expressed above can provide insight into the behavior of possible types of electrode configurations used to monitor in-service composites. If flat, on-surface electrodes are to be used, slight increases in surface voids due to mass loss could

show permittivity changes. Additionally, if electrodes are to be painted or sputtered onto the composites, then below-surface voids and BMI resin changes due to aging could be detected.

For IR-spectroscopy, its usefulness in identifying aging indicators was shown for two different systems. For a BMI/glass-fiber system, the sensitivity of a major carbonyl peak was used with normalization techniques to distinguish between different aged states of the composite. An interesting point is that this might not be a reflection of lost carbonyl groups, but instead a measure of the total resin being lost. This is evident as features from the glass-fiber weave become more prominent as the aging temperatures are increased.

For the epoxy/carbon-fiber system, a similar technique was utilized. In this case, however, there was a large increase in the carbonyl peak, which is essentially non-existent in the unaged samples. Since epoxy is generally devoid of carbonyls in its structure, any oxidation introduces carbonyls which can show up in the IR spectra. Additionally, features at higher wavenumbers near 2920 cm^{-1} and 3070 $^{-1}$ show aging trends, with the feature at 2920 cm^{-1} decreasing with increasing aging temperature, and the feature at 3070 cm^{-1} increasing with increasing aging temperature. As described with the BMI composites, however, at high enough aging temperatures the general epoxy features start to become less distinct, and a general broadening of features occurs due to characteristic vibration frequencies changing because of chemical changes.

As previously discussed, obtaining IR spectra non-destructively has become more common as IR technology has advanced [76, 77]. These advancements can lead to practical utilization of the techniques described above. An initial scan on an unaged composite could be compared to subsequent scans at various points throughout the composites' service-life. Coupled with dielectric spectroscopy, these two NDE techniques could help to monitor thermo-oxidative aging in composites, and become part of the NDE repertoire with UT.

For instance, UT could be used on an in-service composite to check for larger defects or flaws: disbonds, delaminations, large voids. In addition, the IR spectrum could be measured with a handheld device [76] and compared to the spectrum of the same composite at an earlier stage in its service-life. Finally, the dielectric properties could be measured via a patch electrode, or one already painted on. Similarly, this spectrum could be compared to an earlier service-life

spectrum. Any spectral changes in either the IR spectra (1720 cm^{-1} peak intensity; permittivity drop at 1 kHz) could be correlated to a loss of ILSS. These spectra could be recorded, and compared against the spectra obtained in the following check-up.

For the interphase model, future work could be applying it to more material systems to determine its wider applicability. For individual systems, data fits can be made at a range of frequency values. From these values, an interphase spectrum could be created as a function of frequency. Then, using the Kramers-Krönig relations [98, 99], which relate the real part of the permittivity to the imaginary part (and vice versa), the imaginary permittivity could be determined for the interphase. This could lead to observing interphase relaxations, or noting other losses that could occur.

With regards to identifying aged composite indicators, future work could include further characterization of the resin materials dielectrically (model BMI beta and alpha relaxations; determine activation energy changes due to aging; characterize epoxy relaxations for use in glass-fiber composites), and chemically via IR (more feature identification, quantitative IR). From a practical standpoint, how these molecular changes can be identified over a coat of paint or other covering must be investigated. Microscopy, optical and/or electron, could be used to observe possible microvoids in the surfaces of the aged BMI/glass-fiber samples. Additionally, a comparison of the current accelerated aging results to those obtained from long-term isothermal aging, to confirm the applicability of the above techniques.

Bibliography

[1] Weixing Sun, Xiaoli Tan, Michael R. Kessler, and Nicola Bowler. Dielectric properties of cyanate ester/silicon nanocomposites for multifunctional structural capacitors. In *2012 Annual Report Conference on Electrical Insulation and Dielectric Phenomena*. Institute of Electrical & Electronics Engineers (IEEE), oct 2012. doi: 10.1109/ceidp.2012.6378847. URL http://dx.doi.org/10.1109/CEIDP.2012.6378847.

[2] Florin Ciuprina, Ilona Plesa, Petru V. Notingher, Tiberiu Tudorache, and Denis Panaitescu. Dielectric properties of nanodielectrics with inorganic fillers. In *2008 Annual Report Conference on Electrical Insulation and Dielectric Phenomena*. Institute of Electrical & Electronics Engineers (IEEE), oct 2008. doi: 10.1109/ceidp.2008.4772905. URL http://dx.doi.org/10.1109/CEIDP.2008.4772905.

[3] Coporate Research Centre EADS Deutschland GmbH. The research requirements of the transport sectors to facilitate an increased usage of composite materials. June 2004. URL http://cekomat.sav.sk/data/files/21.pdf.

[4] Evan E. Bolton, Yanli Wang, Paul A. Thiessen, and Stephen H. Bryant. Pubchem: Integrated platform of small molecules and biological activities. *Annual Reports in Computational Chemistry*, 4, 2008. URL https://pubchem.ncbi.nlm.nih.gov/compound/83648.

[5] Safa Kasap. *Principles of Electronic Materials and Devices*. McGraw-Hill Science/Engineering/Math, 2005. ISBN 0073104647.

[6] Taku Matsuo. Carbonyl absorption bands in the infrared spectra of some cyclic imides with a five-membered ring. *Bulletin of the Chemical Society of Japan*, 37(12):1844–1848, 1964. doi: 10.1246/bcsj.37.1844. URL http://dx.doi.org/10.1246/bcsj.37.1844.

[7] Marc Loudon. *Organic Chemistry, 5th Edition*. Roberts and Company Publishers, 2009. ISBN 0981519431.

[8] Tetsuya Hanai, Naokazu Koizumi, and Rempei Gotoh. Dielectric properties of emulsions. *Kolloid-Zeitschrift & Zeitschrift für Polymere*, 184(2):143–148, aug 1962. doi: 10.1007/bf01795086. URL http://dx.doi.org/10.1007/BF01795086.

[9] Enis Tuncer, Isidor Sauers, D Randy James, Alvin R Ellis, M Parans Paranthaman, Tolga Aytuğ, Srivatsan Sathyamurthy, Karren L More, Jing Li, and Amit Goyal. Electrical properties of epoxy resin based nano-composites. *Nanotechnology*, 18(2):025703, dec 2006. doi: 10.1088/0957-4484/18/2/025703. URL http://dx.doi.org/10.1088/0957-4484/18/2/025703.

[10] Rm-3002 bismaleimide (bmi) prepreg product information. Technical report, Renegade Materials Corporation, Miamisburg, OH 45342, July 2013. URL http://www.renegadematerials.com/_CE/pagecontent/Documents/RM-3002%20BMI%20Prepreg%20Datasheet%20%2007-22-13.pdf.

[11] ASTM Standard D3171-11. *Standard Test Methods for Constituent Content of Composite Materials*. ASTM International, West Conshohocken, PA, 2011.

[12] Mark Huber. Beached starship. *Air & Space Magazine*, September 2004. URL http://www.airspacemag.com/military-aviation/beached-starship-5429731/.

[13] A. Baker, S. Dutton, and D. Kelly. *Composite Materials for Aircraft Structures, Second Edition (AIAA Education)*. AIAA, 2004. ISBN 1563475405.

[14] Huntsman International LLC. Lighter-weight composite airplane, Accessed November 2014. URL http://www.huntsman.com/advanced_materials/a/Your%20Industry/Lighter-weight%20composite%20airplane.

[15] Guy Norris and Mark Wagner. *Airbus Jetliners (Enthusiast Color Series)*. Zenith Press, 1999. ISBN 076030677X.

[16] Guy Norris. *Airbus A380: Superjumbo of the 21st Century*. Zenith Press, 2005. ISBN 076032218X.

[17] Justin Hale. Boeing 787 from the Ground Up. *AERO*, 4:17–23, 2006. URL http://www.boeing.com/commercial/aeromagazine.

[18] Airbus. Eco-efficiency, Accessed November 2014. URL www.a350xwb.com/eco-efficiency.

[19] Chris Red. The outlook for thermoplastics in aerospace composites, 2014-2023. *High-Performance Composites*, 22(5), 2014.

[20] Hiroko Tabuchi. Japan re-emerges in the aerospace arena with a new jet. *New York Times*, April 9 2013. URL http://www.nytimes.com/2013/04/10/business/global/japan-re-emerges-in-the-aerospace-arena-with-a-new-jet.html.

[21] Fairing, April 2013. URL www.spacex.com/news/2013/04/12/fairing.

[22] Falcon 9, Accessed November 2014. URL www.spacex.com/falcon9.

[23] James K. Sutter, Brian J. Benson, Thomas S. Gates, Roger J. Morgan, John C. Thesken, and S. Leigh Phoenix. Material issues in space shuttle composite overwrapped pressure vessels. *NASA Technical Reports Server*, 2006. URL http://ntrs.nasa.gov/archive/nasa/casi.ntrs.nasa.gov/20060020264.pdf.

[24] M. Akay, G. R. Spratt, and B. Meenan. The effects of long-term exposure to high temperatures on the ilss and impact performance of carbon fibre reinforced bismaleimide. *Comp. Sci. Technol.*, 63:1053–1059, 2003.

[25] Xiaoliang Zeng, Shuhui Yu, and Rong Sun. Thermal behavior and dielectric property analysis of boron nitride-filled bismaleimide-triazine resin composites. *Journal of Applied Polymer Science*, pages n/a–n/a, 2012. doi: 10.1002/app.38276. URL http://dx.doi.org/10.1002/app.38276.

[26] H.-G. Zhu, C. K. Y. Leung, J.-K. Kim, and M.-Y. Liu. Degradation of glass fiber-reinforced plastic composites containing nanoclay in alkaline environment. *Journal of Composite Materials*, 45(21):2147–2156, may 2011. doi: 10.1177/0021998311401064. URL http://dx.doi.org/10.1177/0021998311401064.

[27] Krzysztof Pielichowski and James Njuguna. *Thermal Degradation of Polymeric Materials*. Rapra Technology Limited, Shawbury, UK, 2005.

[28] Horst Stenzenberger. Bismaleimide resins. *ASM Handbook*, 21:97–104, 2001.

[29] Xinying Lv, Rongguo Wang, Wenbo Liu, and Long Jiang. Effect of thermal-oxidative aging on carbon fibre-bismaleimide composites. *Pigment & Resin Technology*, 41(1):34–41, jan 2012. doi: 10.1108/03699421211192262. URL http://dx.doi.org/10.1108/03699421211192262.

[30] Jeffrey J. Sweterlitsch, Roger W. Jones, David K. Hsu, and John F. McClelland. Prediction of interlaminar shear strength of a thermally aged carbon/epoxy composite material by fourier transform infrared photoacoustic spectroscopy. *Appl Spectrosc*, 58(12):1420–1423, dec 2004. doi: 10.1366/0003702042641407. URL http://dx.doi.org/10.1366/0003702042641407.

[31] Chengyu Zhang, Jianjie Gou, Shengru Qiao, Xuanwei Wang, and Jun zhang. Interlaminar shear strength of sic matrix composites reinforced by continuous fibers at 900 c in air. *Materials & Design*, 53(0):93 – 98, 2014. ISSN 0261-3069. doi: http://dx.doi.org/10.1016/j.matdes.2013.06.080. URL http://www.sciencedirect.com/science/article/pii/S0261306913006146.

[32] ASTM Standard D3846-08. *Standard Test Method for In-Plane Shear Strength of Reinforced Plastics*. ASTM International, West Conshohocken, PA, 2008.

[33] Donald F. Adams. The double-notch shear test specimen for composite materials. *High-Performance Composites*, 21(5):15–16, 2013.

[34] Andrzej Garbacz and Edward J. Garboczi. Ultrasonic evaluation methods applicable to polymer concrete composites. *NISTIR 6975*, 2003.

[35] M. Akay and G. R. Spratt. Evaluation of thermal ageing of a carbon fibre reinforced bismalemide. *Comp. Sci. Technol.*, 68:3081–3086, 2008.

[36] R. A. Roberts. Computational prediction of micro-crack induced ultrasound attenuation in CFRP composites. *Journal of Nondestructive Evaluation*, 33(3):443–457, apr 2014. doi: 10.1007/s10921-014-0240-1. URL http://dx.doi.org/10.1007/s10921-014-0240-1.

[37] M Rojek, J Stabik, and G Wrobel. Ultrasonic methods in diagnostics of epoxy–glass composites. *Journal of Materials Processing Technology*, 162-163:121–126, 2005.

[38] Ari Sihvola. *Electromagnetic Mixing Formulae and Applications (IEEE Electromagnetic Waves Series, 47)*. The Institution of Engineering and Technology, 1999. ISBN 0852967721.

[39] Anthony C. Comer, Douglass S. Kalika, Brandon W. Rowe, Benny D. Freeman, and Donald R. Paul. Dynamic relaxation characteristics of matrimid® polyimide. *Polymer*, 50(3): 891–897, jan 2009. doi: 10.1016/j.polymer.2008.12.013. URL http://dx.doi.org/10.1016/j.polymer.2008.12.013.

[40] Jack L. Koenig. *Spectroscopy of Polymers (ACS Professional Reference Books)*. Wiley-VCH, 1992. ISBN 0841219044.

[41] C. Reed. Advances in polymer dielectrics over the past 50 years. *IEEE Electrical Insulation Magazine*, 29(4):58–62, 2013. doi: 10.1109/mei.2013.6545261. URL http://dx.doi.org/10.1109/MEI.2013.6545261.

[42] J.K. Nelson, J.C. Fothergill, L.A. Dissado, and W. Peasgood. Towards an understanding of nanometric dielectrics. In *Annual Report Conference on Electrical Insulation and Dielectric Phenomena*. Institute of Electrical & Electronics Engineers (IEEE), 2002. doi: 10.1109/ceidp.2002.1048793. URL http://dx.doi.org/10.1109/CEIDP.2002.1048793.

[43] J. K. Nelson. *Dielectric Polymer Nanocomposites*. Springer, 2010. ISBN 978-1-4419-1591-7.

[44] T.J. Lewis. Nanometric dielectrics. *IEEE Trans. Dielect. Electr. Insul.*, 1(5):812–825, 1994. doi: 10.1109/94.326653. URL http://dx.doi.org/10.1109/94.326653.

[45] T.J. Lewis. Interfaces are the dominant feature of dielectrics at the nanometric level. *IEEE Trans. Dielect. Electr. Insul.*, 11(5):739–753, oct 2004. doi: 10.1109/tdei.2004.1349779. URL http://dx.doi.org/10.1109/TDEI.2004.1349779.

[46] T. Tanaka. Dielectric nanocomposites with insulating properties. *IEEE Trans. Dielect. Electr. Insul.*, 12(5):914–928, oct 2005. doi: 10.1109/tdei.2005.1522186. URL http://dx.doi.org/10.1109/TDEI.2005.1522186.

[47] George Tsagaropoulos and Adi Eisenberg. Dynamic mechanical study of the factors affecting the two glass transition behavior of filled polymers. similarities and differences with random ionomers. *Macromolecules*, 28(18):6067–6077, aug 1995. doi: 10.1021/ma00122a011. URL http://dx.doi.org/10.1021/ma00122a011.

[48] M. Roy, J.K. Nelson, R.K. MacCrone, L.S. Schadler, C.W. Reed, R. Keefe, and W. Zenger. Polymer nanocomposite dielectrics - the role of the interface. *IEEE Trans. Dielect. Electr. Insul.*, 12(4):629–643, aug 2005. doi: 10.1109/tdei.2005.1511089. URL http://dx.doi.org/10.1109/TDEI.2005.1511089.

[49] Stephanie Raetzke and Josef Kindersberger. Role of interphase on the resistance to high-voltage arcing, on tracking and erosion of silicone/SiO_2 nanocomposites. *IEEE Trans. Dielect. Electr. Insul.*, 17(2):607–614, apr 2010. doi: 10.1109/tdei.2010.5448118. URL http://dx.doi.org/10.1109/TDEI.2010.5448118.

[50] M.G. Todd and F.G. Shi. Molecular basis of the interphase dielectric properties of microelectronic and optoelectronic packaging materials. *IEEE Transactions on Components and Packaging Technologies*, 26(3):667–672, sep 2003. doi: 10.1109/tcapt.2003.817862. URL http://dx.doi.org/10.1109/TCAPT.2003.817862.

[51] M.G. Todd and F.G. Shi. Complex permittivity of composite systems: a comprehensive interphase approach. *IEEE Trans. Dielect. Electr. Insul.*, 12(3):601–611, jun 2005. doi: 10.1109/tdei.2005.1453466. URL http://dx.doi.org/10.1109/TDEI.2005.1453466.

[52] D. Pitsa and M. G. Danikas. Modeling relative permittivity and electrical treeing in polymer nanocomposites. In *2013 IEEE International Conference on Solid Dielectrics (ICSD)*. Institute of Electrical & Electronics Engineers (IEEE), jun 2013. doi: 10.1109/icsd.2013.6619709. URL http://dx.doi.org/10.1109/ICSD.2013.6619709.

[53] DESPOINA PITSA and MICHAEL G. DANIKAS. INTERFACES FEATURES IN POLYMER NANOCOMPOSITES: A REVIEW OF PROPOSED MODELS. *NANO*, 06(06): 497–508, dec 2011. doi: 10.1142/s1793292011002949. URL http://dx.doi.org/10.1142/S1793292011002949.

[54] Thomas Andritsch, Roman Kochetov, Yonas T. Gebrekiros, Peter H. F. Morshuis, and Johan J. Smit. Short term DC breakdown strength in epoxy based BN nano- and micro-composites. In *2010 10th IEEE International Conference on Solid Dielectrics*. Institute of Electrical & Electronics Engineers (IEEE), jul 2010. doi: 10.1109/icsd.2010.5568098. URL http://dx.doi.org/10.1109/ICSD.2010.5568098.

[55] Santanu Singha and M. Thomas. Dielectric properties of epoxy nanocomposites. *IEEE Trans. Dielect. Electr. Insul.*, 15(1):12–23, 2008. doi: 10.1109/t-dei.2008.4446732. URL http://dx.doi.org/10.1109/T-DEI.2008.4446732.

[56] Santanu Singha and M. Joy Thomas. Reduction of permittivity in epoxy nanocomposites at low nano-filler loadings. In *2008 Annual Report Conference on Electrical Insulation and Dielectric Phenomena*. Institute of Electrical & Electronics Engineers (IEEE), oct 2008. doi: 10.1109/ceidp.2008.4772804. URL http://dx.doi.org/10.1109/CEIDP.2008.4772804.

[57] Connor S. Daily, Michael R. Kessler, Xaoli Tan, and Nicola Bowler. On the nanoparticle interphase. In *2012 Annual Report Conference on Electrical Insulation and Dielectric Phenomena*. Institute of Electrical & Electronics Engineers (IEEE), oct 2012. doi: 10.1109/ceidp.2012.6378831. URL http://dx.doi.org/10.1109/CEIDP.2012.6378831.

[58] P. A. M. Steeman and F. H. J. Maurer. An interlayer model for the complex dielectric constant of composites. *Colloid & Polymer Sci*, 268(4):315–325, apr 1990. doi: 10.1007/bf01411674. URL http://dx.doi.org/10.1007/BF01411674.

[59] W. R. Tinga. Generalized approach to multiphase dielectric mixture theory. *J. Appl. Phys.*, 44(9):3897, 1973. doi: 10.1063/1.1662868. URL http://dx.doi.org/10.1063/1.1662868.

[60] David R. Lide. *CRC Handbook of Chemistry and Physics, 82nd Edition*. CRC Press, 2001. ISBN 0849304822.

[61] Anna Spanoudaki and Rolf Pelster. Effective dielectric properties of composite materials: The dependence on the particle size distribution. *Physical Review B*, 64(6), jul 2001. doi: 10.1103/physrevb.64.064205. URL http://dx.doi.org/10.1103/PhysRevB.64.064205.

[62] C. Brosseau, A. Beroual, and A. Boudida. How do shape anisotropy and spatial orientation of the constituents affect the permittivity of dielectric heterostructures? *J. Appl. Phys.*, 88 (12):7278, 2000. doi: 10.1063/1.1321779. URL http://dx.doi.org/10.1063/1.1321779.

[63] Michael Teal. New 737 MAX: Improved Fuel Efficiency and Performance. *AERO*, 1:5–11, 2014. URL http://www.boeing.com/commercial/aeromagazine.

[64] David K Hsu. Nondestructive inspection of composite structures: Methods and practice. In *17th World Conference on Nondestructive Testing*, Shanghai, China, oct 2008. URL http://www.ndt.net/article/wcndt2008/papers/612.pdf.

[65] Ajay Kapadia. Non Destructive Testing of Composite Materials. Technical report, National Composites Network, 2006.

[66] Kwang-Hee Im, David K Hsu, Chien-Ping Chiou, Daniel J Barnard, Jong-An Jung, and In-Young Yang. Terahertz Wave Approach and Application on FRP Composites. *Advances in Materials Science and Engineering*, 2013(563962), 2013. doi: 10.1155/2013/563962. URL http://dx.doi.org/10.1155/2013/563962.

[67] J Wolfrum, S Eibl, and L Lietch. Rapid evaluation of long-term thermal degradation of carbon fibre epoxy composites. *Composites Science and Technology*, 69:523–530, 2009.

[68] HexTow IM7 Carbon Fiber Product Data. Technical report, Hexcel Corporation, Stamford, CT 06901, July 2014.

[69] RM-2005 350 °F Cure Toughened Epoxy Prepreg. Technical report, Renegade Materials Corporation, Miamisburg, OH 45342, September 2013.

[70] John F McClelland and Richard N Kniseley. Photoacoustic spectroscopy with condensed samples. *Applied Optics*, 15:2658–2663, November 1976.

[71] Henry L. Friedman. Kinetics of thermal degradation of char-forming plastics from thermogravimetry. application to a phenolic plastic. *Journal of Polymer Science Part C: Polymer Symposia*, 6(1):183–195, 1964. doi: 10.1002/polc.5070060121.

[72] Takeo Ozawa. A new method of analyzing thermogravimetric data. *Bulletin of the Chemical Society of Japan*, 38(11):1881–1886, 1965. doi: 10.1246/bcsj.38.1881. URL http://dx.doi.org/10.1246/bcsj.38.1881.

[73] Joseph H. Flynn and Leo A. Wall. A quick direct method for the determination of activation energy from thermogravimetric data. *Journal of Polymer Science Part B: Polymer Letters*, 4(5):323–328, 1966. doi: 10.1002/pol.1966.110040504.

[74] C. D. Doyle. Kinetic analysis of thermogravimetric data. *Journal of Applied Polymer Science*, 5(15):285–292, 1961. doi: 10.1002/app.1961.070051506.

[75] C. D. Doyle. Estimating isothermal life from thermogravimetric data. *Journal of Applied Polymer Science*, 6(24):639–642, 1962. doi: 10.1002/app.1962.070062406.

[76] John Seelenbinder. Composite heat damage measurement using the handheld Agilent 4100 ExoScan FTIR. Technical report, Agilent Technologies, Santa Clara, CA 95051, May 2011.

[77] Celia Henry Arnaud. Handheld ir in the hangar. *Chemical & Engineering News*, 89(34):43–45, aug 2011. URL http://cen.acs.org/articles/89/i34/Handheld-IR-Hangar.html.

[78] Cytec Industries Inc. (NYSE:CYT). *Lockheed Martin Extends Cytec Contract for Advanced Materials JSF Program through 2020.* 2011. URL http://www.cytec.com/company/news/press-release/lockheed-martin-extends-cytec-contract-advanced-materials-jsf-program.

[79] CompositesWorld. The markets: Aerospace (2014). 2014. URL http://www.compositesworld.com/articles/the-markets-aerospace-2012.

[80] J Hopewell. Quantitative analysis of bismaleimide-diamine thermosets using near infrared spectroscopy. *Polymer*, 41(23):8221–8229, nov 2000. doi: 10.1016/s0032-3861(00)00198-1. URL http://dx.doi.org/10.1016/S0032-3861(00)00198-1.

[81] S.J. Shaw and A.J. Kinloch. Toughened bismaleimide adhesives. *International Journal of Adhesion and Adhesives*, 5(3):123–127, jul 1985. doi: 10.1016/0143-7496(85)90052-1. URL http://dx.doi.org/10.1016/0143-7496(85)90052-1.

[82] M. Satheesh Chandran, M. Krishna, Sheshappa Rai, M. S. Krupashankara, and K. Salini. Cure kinetics and activation energy studies of modified bismaleimide resins. *ISRN Polymer Science*, 2012:1–8, 2012. doi: 10.5402/2012/309861. URL http://dx.doi.org/10.5402/2012/309861.

[83] Thomas M. Donnellan and David Roylance. Relationships in a bismaleimide resin system. part i: Cure mechanisms. *Polym. Eng. Sci.*, 32(6):409–414, mar 1992. doi: 10.1002/pen.760320604. URL http://dx.doi.org/10.1002/pen.760320604.

[84] R. Torrecillas, A. Baudry, J. Dufay, and B. Mortaigne. Thermal degradation of high performance polymers—influence of structure on polyimide thermostability. *Polymer Degradation and Stability*, 54(2-3):267–274, nov 1996. doi: 10.1016/s0141-3910(96)00052-3. URL http://dx.doi.org/10.1016/S0141-3910(96)00052-3.

[85] R. Torrecillas, N. Regnier, and B. Mortaigne. Thermal degradation of bismaleimide and bisnadimide networks—products of thermal degradation and type of crosslinking points. *Polymer Degradation and Stability*, 51(3):307–318, mar 1996. doi: 10.1016/0141-3910(95)00197-2. URL http://dx.doi.org/10.1016/0141-3910(95)00197-2.

[86] Pellegrino Musto, Giuseppe Ragosta, Peitro Russo, and Leno Mascia. Thermal-oxidative degradation of epoxy and epoxy-bismaleimide networks: Kinetics and mechanism. *Macromolecular Chemistry and Physics*, 202(18):3445–3458, dec 2001. doi: 10.1002/1521-3935(20011201)202:18⟨3445::AID-MACP3445⟩3.0.CO;2-N.

[87] Peter J. W. Debye. *Polar molecules*. The Chemical Catalog Company, Inc., 1929.

[88] Kenneth S. Cole and Robert H. Cole. Dispersion and absorption in dielectrics i. alternating current characteristics. *J. Chem. Phys.*, 9(4):341, 1941. doi: 10.1063/1.1750906. URL http://dx.doi.org/10.1063/1.1750906.

[89] D. W. Davidson and R. H. Cole. Dielectric relaxation in glycerol, propylene glycol, and n-propanol. *J. Chem. Phys.*, 19(12):1484, 1951. doi: 10.1063/1.1748105. URL http://dx.doi.org/10.1063/1.1748105.

[90] S. Havriliak and S. Negami. A complex plane representation of dielectric and mechanical relaxation processes in some polymers. *Polymer*, 8:161–210, jan 1967. doi: 10.1016/0032-3861(67)90021-3. URL http://dx.doi.org/10.1016/0032-3861(67)90021-3.

[91] F. Kremer and A. Schönhals. *Broadband Dielectric Spectroscopy*. Springer, 2003. ISBN 3540434070.

[92] A. Schönhals. Dielectric spectroscopy on the dynamics of amorphous polymeric systems. novocontrol application notes. *Dielectrics*, 1, 2003. URL http://www.novocontrol.de/pdf_s/APND1.PDF.

[93] P. R. Hondred, S. Yoon, N. Bowler, E. Moukhina, and M. R. Kessler. Degradation kinetics of polyimide film. *High Performance Polymers*, may 2011. doi: 10.1177/0954008311409262.

[94] Tariq Chady. Airbus versus boeing - composite materials: The sky's the limit..., September 2013. URL www.lemauricien.com/article/airbus-versus-boeing-composite-materials-sky-s-limit.

[95] Donna Dawson. U.s. crew and cargo candidate takes shape with composites. *High-Performance Composites*, 21(3):78–80, 2013.

[96] Dale Brosius. Boeing 787 update. *High-Performance Composites*, may 2007.

[97] D.O. HUMMEL. STRUCTURE AND DEGRADATION BEHAVIOUR OF SYNTHETIC POLYMERS USING PYROLYSIS IN COMBINATION WITH FIELD ION MASS SPECTROMETRY. In *Analytical Pyrolysis*, pages 117–138. Elsevier BV, 1977. doi: 10.1016/b978-0-444-41558-5.50016-x.

[98] H.A. Kramers. La diffusion de la lumière par les atomes. *Transactions of Volta Centenary Congress*, 2:545–557, 1927.

[99] R. DE L. KRONIG. ON THE THEORY OF DISPERSION OF x-RAYS. *J. Opt. Soc. Am.*, 12(6):547, 1926. doi: 10.1364/josa.12.000547.